UNIVERSITÀ DEGLI STUDI DI SALERNO

Dipartimento di Ingegneria dell'Informazione ed Elettrica e Matematica Applicata

ALMA MATER STUDIORUM - UNIVERSITÀ DI BOLOGNA

Dipartimento di Ingegneria dell'Energia Elettrica, Elettronica e dell'Informazione "Guglielmo Marconi"

PHD IN PHOTOVOLTAICS

Curriculum: Power Electronics and Control

Dottorato di Interesse Nazionale in Photovoltaics

Ripple-Free Stacked Interleaved Buck Converter for Hydrogen Production from Photovoltaic Systems

Supervisor:
Prof. Mattia Ricco

PhD Candidate:
Paolo Pilati
Mat. 8860800006

Co-Supervisor:
Prof. Vincenzo Cirimele

PhD Program Director:
Prof. Giovanni Spagnuolo

XXXVIII Cycle
2022 - 2025

Funded by the European Union

MUR
Ministero dell'Università e della Ricerca

Dottorato di Interesse Nazionale

PhD PV

Dottorato di Interesse Nazionale "PHOTOVOLTAICS"

Curricula:

- Solar cells technologies and lifecycle
- Design and integration
- Monitoring and diagnosis
- Power electronics and control
- Solar intermittency and storage
- Distributed generation and grid connection

"It's done."
Francesco Falcetelli, 2024

Contents

List of Figures

List of Tables

Abstract

The intensive and prolonged use of fossil fuels to power most human activities has resulted in severe environmental and climatic consequences. In response to these challenges, the past decade has witnessed increasing global efforts to identify and implement sustainable alternatives with a lower environmental footprint. This has led to a major shift toward renewable energy sources, with solar photovoltaic and wind power emerging as the most widely adopted technologies.

The continuous development and cost reduction of PV and wind systems have enabled their large-scale deployment in power generation. Nevertheless, one of the key limitations of renewable energy sources lies in their inherent intermittency, making them non-dispatchable sources. To mitigate this problem, efficient and scalable energy storage systems are crucial. Such systems allow the temporary storage of excess energy produced during peak generation periods and its subsequent release during times of low production or high demand.

Among the various energy storage systems, hydrogen-based storage has gained growing interest in recent years due to its versatility and potential for large-scale integration. Hydrogen can function both as a long-term energy carrier and as a clean fuel capable of decarbonising hard-to-abate sectors such as heavy industry and transportation.

Among the various techniques for producing hydrogen, the one that best matches renewable sources is electrolysis. General information on the production process, the various technologies used, the structure of the plants and hydrogen storage systems, as well as the challenges still to be faced, is provided to give as clear a picture as possible of the current state of the art. Because of their characteristics, the focus is then placed solely on Proton Exchange Membrane (PEM) electrolysers and metal hydride storage systems.

An analysis of the literature on the types of electronic power converters used or theorised for this application is also carried out. Of all the converter topologies already considered, the one best suited to powering a PEM-type electrolyser is the stacked interleaved buck, thanks to its ability to cancel the output current ripple under any load condition. A modulation technique is therefore studied to maximise the efficiency of the converter while ensuring the cancellation of current ripple on the electrolyser. Finally, simulations and experimental tests are conducted to validate the proposed solution.

1

Introduction

Fossil fuels are currently the primary energy source behind most human activities. However, their extensive use has led to several negative consequences, including air pollution, stratospheric ozone depletion, and global warming, all of which contribute to climate change [1]. To address these challenges, the past decade has seen growing efforts from the scientific community, industry, and policymakers to develop solutions with a lower environmental footprint, with a strong push toward the adoption of Renewable Energy Sources (RES). As a result, energy production from RES, particularly photovoltaic (PV) and wind power, has increased significantly [2]. However, one of the main characteristics of these sources is their intermittency, as their output is highly dependent on environmental conditions and cannot be dispatched on demand. This makes it essential to implement energy storage systems that can store excess energy when production exceeds demand and release it when needed [3]. Various storage technologies are already available on the market, ranging from pumped hydro storage to batteries and supercapacitors. Among these, hydrogen has gained considerable attention in recent years due to its dual role: it can serve both as an energy carrier for storing renewable energy and as a clean fuel for decarbonizing hard-to-abate industrial sectors [4, 5].

Hydrogen can be produced in various ways, as will be explained in more detail later in this thesis. Starting from electrical energy, the technique that best combines with it is water electrolysis. Since 2020, the European Union has financed numerous projects focused on the development of hydrogen production plants powered by RES, with system capacities ranging from the MW scale up to several GW [6]. In many cases, PV technology is the preferred renewable energy source, particularly for projects located in southern European countries, where the availability of sunlight hours is significantly higher [7]. Reflecting the growing scientific interest in identifying optimal solutions for the development of this technology, Fig. 1.1 illustrates the trend in the number of publications over the past two decades focused specifically on power electronic converters for hydrogen production from PV systems.

The data were collected using both general search engines, such as Google Scholar, and more specialized academic databases, including ScienceDirect and IEEE Xplore. The search was conducted using the keywords: "power converters photovoltaic electrolyser." As the figure shows, the number of publications has increased markedly in recent years, indicating a strong and accelerating research focus in this area.

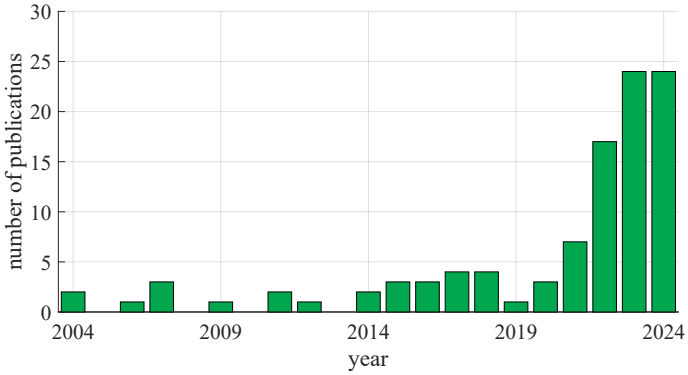

Figure 1.1: Number of publications per year on converters for PV-electrolyser applications.

1.1 Research Problem

Given the considerable development potential of this sector, recent years have seen extensive research into a variety of converter topologies, PV-electrolyser coupling configurations, and control algorithms. About power electronic converters for hydrogen production, numerous studies have been conducted, and several reviews in the literature examine the state of the art, considering either AC sources [8–12] or generic DC sources [8, 11, 13, 14]. In most of these works, however, the focus is placed primarily on the load (namely, the electrolyser) while the energy source is generally assumed to be ideal. This assumption is reasonable in grid-connected applications, where the supply voltage can be considered stable and constant. In contrast, coupling PV systems with electrolysers introduces specific challenges that still require effective solutions.

The primary challenge lies in conversion efficiency, as the current state of the art for hydrogen production from PV typically relies on separate converters for the PV system and the electrolyser. In most cases, to maximize electrolyser output, a grid connection is still employed. As a result, many existing plants use various types of rectifiers to supply the electrolysers, while the PV system is connected to the grid through inverters [15–18]. However, since PV systems and electrolysers are inherently DC sources and loads, respectively, the intermediate AC conversion stage is unnecessary and can reduce the overall system efficiency. A direct connection between PV and electrolyser is also possible [19–23], but this configuration offers

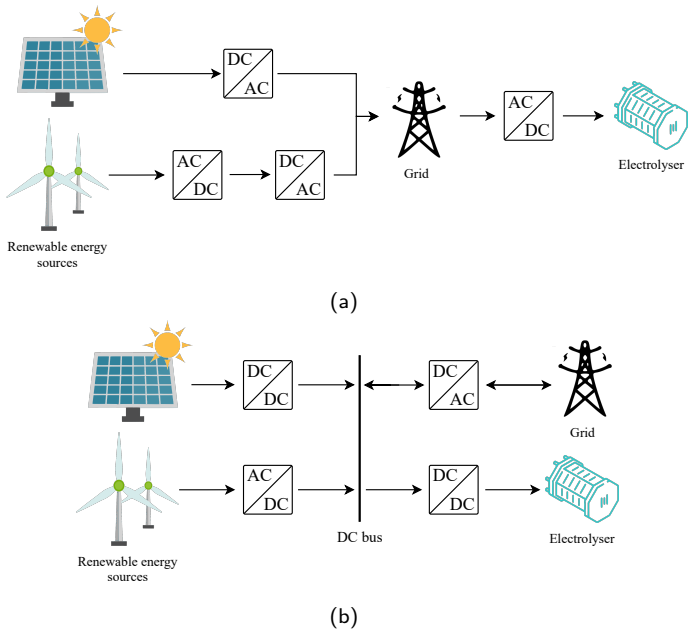

Figure 1.2: Possible system configurations for hydrogen production from renewable sources: (a) current state of the art setup, and (b) potential future architectures.

no control over system operation. Consequently, both components may operate at suboptimal points, particularly under partial shading conditions [24, 25]. For this reason, this approach will not be considered in the present work.

Even when the grid is included to provide balancing services, conversion to AC is not strictly required [26–28]. Fig. 1.2 presents a schematic comparison between the current state of the art layout for hydrogen production from renewable sources and a potential future configuration, in which the coupling could be done through a common DC bus.

The second challenge lies in considering a real PV source as the electrolyser's power supply. With PV sources, the power supply can no longer be considered ideal, but it is necessary to take into account that the input voltage and current can vary suddenly. There are already studies that consider this aspect, but they all exclude and fail to consider one final and fundamental aspect: the other components of the overall system.

A third challenge to consider concerns the current ripple on the electrolyser. As will be discussed in more detail in subsequent chapters, this phenomenon can have a significant impact on the long-term performance and durability of electrolytic cells. Excessive ripple in the current supplied to the stack can lead to a reduction in both efficiency and lifetime of the electrolyser system. For this reason, it becomes essential to identify and implement converter topologies or control strategies that are capable of reducing current ripple to the lowest possible level, ideally achieving

complete ripple cancellation.

The hydrogen management and storage systems are fundamental components that can influence the overall behavior of the entire Power-to-Hydrogen (P2H) system. Since the power generated by PV can vary dramatically in short intervals of time, hydrogen production could also vary rapidly. This characteristic may not be compatible with the characteristics of some storage systems, leading to problems for the overall system.

1.2 Objectives

Based on the foregoing, the objective of this thesis is to identify a modular converter topology that can effectively couple a PV source to an electrolyser.

The primary requirement is the complete elimination of current ripple on the electrolyser. Once the topology has been chosen, the thesis will present a modulation strategy designed to allow the converter to operate with the highest possible efficiency while maintaining the fundamental requirement of ripple-free.

About the modularity of the chosen topology, it is intended not only to reduce costs but also to ensure the scalability of the system, allowing for easier adaptation to different power levels or system configurations. In addition, a modular approach enables more flexible and efficient power flow management, which contributes to improving both the long-term efficiency and the overall reliability of the system.

Finally, when addressing the control of the converter, attention will also be given to the interaction with other system components, such as hydrogen storage units. These subsystems can exhibit non-linear and dynamic behaviours that may significantly affect the overall control strategy of the PV-electrolyser system. Therefore, understanding and accounting for these interactions is essential to ensure stable operation, optimal performance, and effective energy management across the entire system.

1.3 Thesis Structure

After this initial introduction, the thesis is organized into five further Chapters. In the second Chapter, an overview is provided of what hydrogen is, the main production and storage methods and technologies, and the still open challenges that limit its widespread distribution and use.

In the third Chapter, the characteristics of the converter for producing hydrogen from photovoltaics are presented and a review of the literature of non isolated and isolated topologies that have been studied for coupling photovoltaics and electrolysers is reported.

In the fourth Chapter, the thesis proposal is addressed, with an explanation of the chosen topology and its modulation technique. From a theoretical point of view, it will be discussed the topology considered, the possible techniques for improving its efficiency, and those that allow the cancellation of current ripple. It will also make some considerations on component design and possible solutions for managing transients with the proposed modulation technique.

In the fifth Chapter, the results of the simulations carried out and the experiments performed in the laboratory are reported.

Finally, in the sixth and last Chapter, the conclusions are given, with a summary of what has been said previously and an analysis of what may be the future studies and challenges.

2

Power to Hydrogen System

As mentioned in the previous Chapter, hydrogen represents a promising option for storing excess energy generated by RES. This is primarily due to its unique chemical and physical properties, which make it an efficient energy carrier with significant potential for integration into sustainable energy systems.

Hydrogen is the first element of the periodic table, and consequently, it is the smallest and lightest of all elements. At ambient temperature and pressure, it exists as a colorless and odorless gas. One of its key characteristics is its exceptionally high energy density per unit mass, which makes it an attractive fuel for energy storage and conversion applications. However, its energy density per unit volume is relatively low when compared to conventional fuels, posing challenges in terms of storage and transportation. Additionally, hydrogen's high reactivity and wide flammability range make it a potentially hazardous material, requiring stringent safety measures during handling and storage.

Due to these chemical and physical characteristics, hydrogen cannot be considered a primary energy source, as it is not naturally available in its pure form on Earth. Instead, it must be produced from other hydrogen-containing compounds, such as water, hydrocarbons, or biomass. The sustainability of hydrogen production largely depends on the raw materials used and the processes employed for its extraction.

Over time, various hydrogen production pathways have been categorized using a color-based classification, such as grey, blue, and green hydrogen, to indicate the environmental impact and carbon footprint associated with each process. However, it is important to note that this color-based nomenclature is primarily a commercial and communication tool rather than a scientifically rigorous classification. For this reason, it will not be adopted in the context of the present thesis.

2.1 Hydrogen Production

Currently, hydrogen is primarily utilized as a raw material in various industrial processes and is predominantly produced from hydrocarbons [29, 30]. One of the most established and widely adopted techniques for its production is the steam reforming of natural gas, a process that has been industrially optimized over decades. This method is characterized by high productivity and economic profitability, as it enables the extraction of four hydrogen atoms from each methane molecule. Additionally, it does not require the use of rare or expensive materials; the process relies mainly on water and natural gas as feedstocks.

However, hydrogen production from fossil fuels results in significant emissions of greenhouse gases, notably carbon dioxide, which contribute to global warming and climate change. While techniques for carbon capture and storage have been developed as a partial mitigation strategy, they represent only a temporary solution that does not fully eliminate the environmental impact of the process.

For these reasons, hydrogen production from RES has become a rapidly growing field of research and development. Several renewable pathways for hydrogen production have been proposed [31, 32], including biomass pyrolysis, photoelectrochemical water splitting, and biological methods involving genetically modified microorganisms. However, most of these technologies currently suffer from low efficiency and limited production rates, which constrain their practical application on a large scale despite their environmental advantages and relatively low operational costs.

At present, the most mature and widely adopted technique for sustainable hydrogen production is water electrolysis powered by renewable sources, such as PV or wind energy [31, 33]. In this process, electrical energy is used to decompose water molecules into their constituent gases, hydrogen and oxygen, through an electrochemical reaction. The chemical reaction is shown below [34].

$$\mathrm{H_2O(l)} \longrightarrow \mathrm{H_2(g)} + \frac{1}{2}\,\mathrm{O_2(g)} \tag{2.1}$$

This process is not spontaneous, as the calculation of Gibbs free energy under standard conditions ($T = 298$ K, $p = 1$ bar) returns a positive result [35].

When the electrochemical cell operates in reversible conditions, that is, in open-circuit conditions, the voltage E required for the reaction to occur can be calculated as [36]:

$$E = -\frac{\Delta G}{2F}\ , \tag{2.2}$$

where ΔG is the Gibbs free energy change of the reaction, and depends on the temperature and pressure of the reactant, and F is the Faraday constant. The Eq. 2.2

refers to the generator convention, because the same cell operating in reverse, i.e. as a fuel cell, can be a voltage generator. The minus sign in the previous equation must therefore be interpreted as a voltage that needs to be supplied to the cell to drive the electrolysis reaction. However, the expression in Eq. 2.2 is valid only under ideal reversible conditions, meaning that it does not account for the practical non-idealities inherent to real electrolytic cells. In practical operation, several voltage losses must be considered to accurately determine the actual voltage required to sustain the electrolysis process. These non-idealities can be categorized into three main types: activation losses, ohmic losses, and diffusion losses [36].

Each of these losses depends on the current density flowing through the electrolytic cell. Activation losses occur predominantly at low current densities and are associated with the energy barrier that must be overcome for the electrochemical reactions to initiate at the electrode surfaces. Ohmic losses, on the other hand, are due to the resistive effects of the electrolyte and electrodes, and they typically dominate in the normal operating region of the electrolyser. Finally, diffusion losses arise when the current density approaches or exceeds the maximum rated value for the cell. In this region, the mass transport of reactants (e.g., water molecules) to the electrode surface becomes insufficient to sustain the electrochemical reaction rate, leading to a rapid voltage increase and potential degradation of the cell. For this reason, operation in the diffusion losses region is generally avoided, as it can significantly shorten the lifetime of the electrolyser.

Taking these non-idealities into account, the actual voltage V that must be applied to the cell can be expressed as:

$$V = E + V_{\text{act}} + V_{\text{ohm}} + V_{\text{diff}} \ , \tag{2.3}$$

where V_{act}, V_{ohm}, and V_{diff} are respectively voltages representing activation losses, ohmic losses, and diffusion losses. The static voltage-current characteristic that can be derived from Eq. 2.3 of an electrolytic cell is called the polarisation curve. Since this curve also depends on constructive parameters of the cell, such as its active area (which is usually considered an industrial secret), the given data refer to the current density-voltage curve. For example, in Fig. 2.1, the polarisation curve of a commercial electrolyser stack is reported. The diffusion losses region is not reported, as it exceeds the maximum rated power of the stack. In general, the voltage to be applied to a single cell is in the order of volts. To obtain sufficiently high operating voltages, several cells are electrically connected in series and hydraulically in parallel to form a stack.

The molar flow rate of hydrogen produced by a stack $\dot{N}_{\text{H}_2}$ can be easily calculated using Faraday's law [37]:

$$\dot{N}_{\text{H}_2} = N_{\text{cell}} \frac{I_{\text{el}}}{2F} \eta_{\text{F}} \ . \tag{2.4}$$

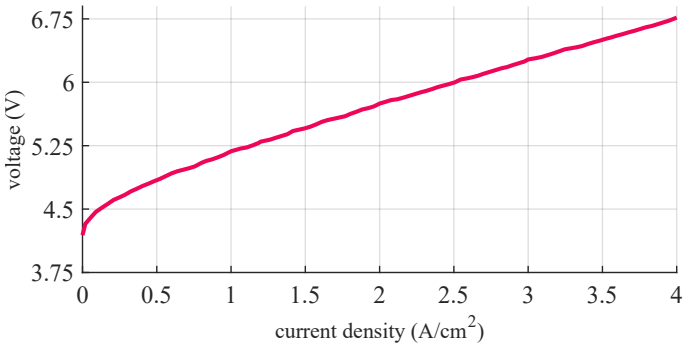

Figure 2.1: Polarisation curve of a representative commercial electrolyser.

In Eq. 2.4 I_{el} represents the current absorbed by the stack, composed of a generic number of electrolytic cells N_{cell}, while η_{F} is Faraday's efficiency. If the reaction is ideal, according to Eq. 2.1, for each mole of water that reacts, there should be one mole of hydrogen, and therefore Faraday's efficiency would be equal to 1. In reality, this does not occur due to various non-idealities in chemical reactions and therefore, to obtain one mole of hydrogen output, it is necessary to supply more than one mole of water ($\eta_{\text{F}} < 1$). Thus, knowing the polarisation curve of a stack, it is possible to calculate, as a first approximation, the hydrogen produced depending on the voltage applied to the stack.

Based on the above discussion, it can be concluded that electrolysers are modular, low-voltage, and high-current loads. They are modular because their total power capacity can be scaled by varying the number of individual cells connected in series, allowing flexible system sizing according to the desired hydrogen production rate. They are low-voltage devices, since the voltage required by each individual cell is relatively small, typically around 1.6 to 2.0 V under nominal operating conditions, so even with hundreds of cells connected in series, the total stack voltage generally reaches only a few hundred volts. Finally, electrolysers are high-current loads, as the total current drawn by the stack increases proportionally with the active surface area of the electrodes and the overall system size.

There are different electrolyser technologies, differing in the ion-conducting electrolyte materials, each with their own advantages and disadvantages. In general, depending on the material used as electrolyte, they can be divided into two categories based on the temperatures at which they can operate: low and high temperature. In the low-temperature ones, there are:

1. **Liquid Alkaline.**

   This is the most established of the various technologies and is therefore cheap, reliable, and already available for large power sizes. However, it employs corrosive liquid reagents, is not suitable for dynamic use, and has

low efficiencies [38];

2. **Proton Exchange Membrane (PEM).**

   This technology has grown a lot in the market in recent years, because it has a better dynamic response than alkalines, does not use toxic elements, thus allowing greater simplicity of the system, it can conduct high current densities, allowing higher power for the same volume or being more compact for the same power, and finally, it has an almost constant efficiency trend over the entire load curve [39]. On the other hand, however, it requires expensive materials (rare metals for the electrodes and special polymers for the electrolytic membrane), which makes it more expensive than alkalines [40];

3. **Anion Exchange Membrane (AEM).**

   This technology is still under development and combines the advantages and disadvantages of the other two technologies already discussed. It allows for dynamic use and is cheaper than PEM as it requires smaller quantities of rare materials, but currently has issues related to the durability and performance of the electrolitic membranes [41].

High-temperature ones, on the other hand, include solid oxide (SO) electrolysers. This is a technology that is still in the development phase, requires greater plant engineering complexity, and therefore has high costs. They also have long ignition times, which makes intermittent use inconvenient [42, 43]. But SOs have demonstrated significant potential for achieving high efficiency, since they can use heath instead of electricity [44].

Fig. 2.2 shows an example of a commercial PEM electrolyser. The lower compartment houses the stack, while the upper section contains part of the auxiliary systems responsible for gas treatment and stack supply management. These auxiliary systems ensure the proper conditioning of the gases produced and maintain the required operating conditions for the electrolyser.

As reported by the International Energy Agency (IEA), the global installed capacity for water electrolysis is expected to reach approximately 5 GW by the end of 2025 [30]. According to IEA data, around 71% of the global operational capacity utilizes alkaline electrolysis, while 20% relies on proton PEM electrolysis. This is because, as already said, alkaline technology is the more mature and economical option of the two [42]. In Europe, the distribution between these technologies is more evenly balanced, with alkaline systems representing 44% and PEM systems at 53%. This is largely due to the commissioning of several large-scale PEM projects in recent years related to the Next Generation EU. The interest in the use of PEM-type electrolyzers can be attributed to their ability to respond more quickly to changes in load demand than alkalines [45, 46]. This makes them more suitable for uses

Figure 2.2: Example of a commercial electrolyser unit.

connected to RES, where production can vary rapidly. However, both alkaline and PEM electrolysis are classified as mature technologies and have reached commercial operation in relevant environments in line with IEA standards [47].

Unlike other storage systems, like batteries and supercapacitors, electrolysers require a more complex system to manage the various reactants. Therefore, an hydrogen production plant from electrolysis can be divided into four main parts:

1. **The power unit.**

   Always present to control stack production, it consists of electronic power converters that interface the power supply and load. There are various topologies, depending on the type of power supply;

2. **The stack.**

   It is the set of all electrolytic cells where the reaction takes place. Within a plant, there may be several stacks connected in parallel to increase production;

3. **The hydrogen storage system.**

   Where hydrogen is stored. Depending on the technologies used for storage, some auxiliary systems may change. Hydrogen storage systems will be discussed in more detail below;

4. **The auxiliaries systems.**

Auxiliary systems include all systems necessary for the proper functioning of the plant: water pumps, valves, gas purification filters, cooling fans, etc.

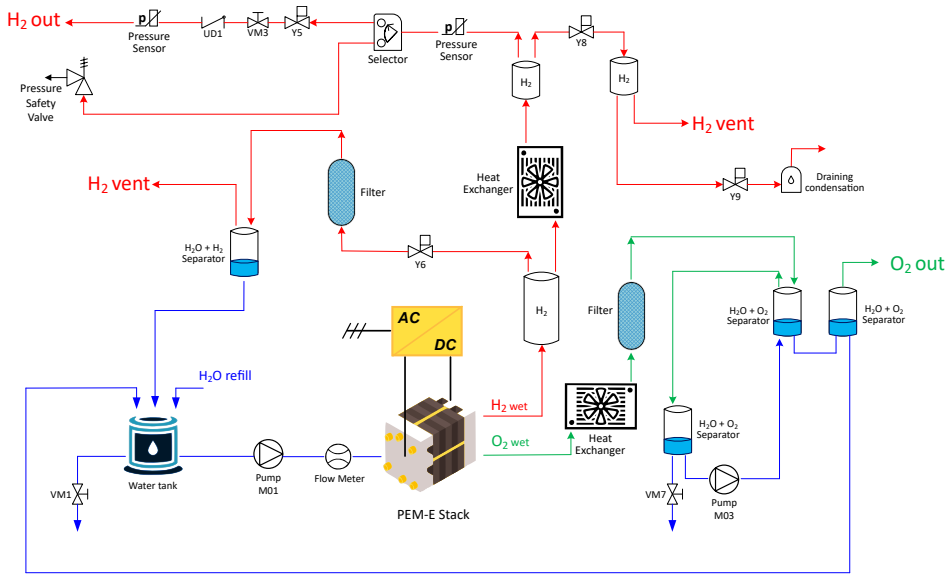

Figure 2.3: Detailed schematic of the electrolyser BoP. The water circuit is shown in blue, oxygen in green, and hydrogen in red.

Power supply, stacks, and auxiliary systems make up the Balance of Plant (BoP) of an electrolyser. In Fig. 2.3, the BoP of the electrolyser used for the experiments conducted during the PhD program is given as an example.

The system control is generally based on monitoring the pressure within the hydrogen circuit: once an upper pressure threshold is defined, hydrogen production is regulated to ensure operation within safe limits. Due to the system's mass balance, pressure will increase if the production rate exceeds the output flow rate, and decrease in the opposite case. When the output flow rate is very low, below the stack's minimum production threshold, the system operates the stack discontinuously, effectively performing pulse width modulation (PWM) on the hydrogen generation process.

A noteworthy auxiliary subsystem present in PEM electrolysers, responsible for a recurring operational phenomenon, is the short-circuit unit (SCU). It is often directly integrated into the stack's power supply circuitry. The SCU periodically short-circuits the stack, driving the cell voltages close to zero in order to purge or consume residual reactants and to accelerate safe activation or rejuvenation of the cells. It prevents damage from hydrogen-air fronts and shortens conditioning time. The operating period of the SCU and related gas purge valves is a parameter set by the manufacturer and is generally constant, regardless of the stack's usage time. In

Fig. 2.4a, it is possible to appreciate the effect of this phenomenon on the hydrogen flow rate directed to the storage system, which results in a fluctuation of the overall trend and in a localized reduction of the flow rate every time the purging is carried out.

2.2 Hydrogen Storage

As previously mentioned in reaction 2.1, hydrogen is typically produced in its gaseous form. Given its low volumetric density, storing it in compact volumes requires an additional processing step. There are three main methods for hydrogen storage currently in use or under investigation: in compressed gaseous form, in liquid form, and in solid form within chemical compounds.

Compressed hydrogen represents the most mature technology among these. The most advanced systems available today use cylinders capable of withstanding pressures of up to 800 bar [48]. However, such high pressures raise concerns regarding safety and the potential risk of explosion. Moreover, hydrogen compression requires specialised compressors, which not only constitute a significant additional investment for the plant but also continuously consume energy during operation.

Alternatively, hydrogen can be stored in liquid form using cryogenic systems operating at temperatures below -253 °C. This approach allows for even higher storage densities per unit volume compared to compressed hydrogen. Nevertheless, boil-off phenomena, caused by the evaporation of hydrogen within storage tanks, must be carefully managed to prevent excessive pressure build-up. If uncontrolled, this can result in unwanted hydrogen venting once the tank's maximum pressure limit is reached [49, 50]. In this case as well, the energy required for maintaining cryogenic conditions is far from negligible.

The most recent approach under investigation for hydrogen storage involves solid-state compounds. This can be achieved in two main ways: either by chemically binding hydrogen to other elements to form more stable and manageable compounds, or by employing special metallic alloys known as metal hydrides (MHs).

In the former case, hydrogen is combined through a chemical reaction to form a new compound (such as ammonia), which is typically denser and more stable. However, this process results in the loss of readily available pure hydrogen. To retrieve the hydrogen, a reverse reaction must be carried out: a process that is generally highly energy-intensive, given the stability of the newly formed compound. Thus, rather than a true storage method, this approach can be more accurately regarded as a technique for producing directly usable compounds.

Regarding storage in MHs, the ability of certain metal alloys to reversibly bind hydrogen is exploited, allowing its release when necessary without requiring significant energy input. Compared to the other storage methods discussed, MHs

offer several important advantages in terms of both safety and performance. They enable high volumetric energy densities, even higher than those of liquid hydrogen [51], while operating at relatively low pressures.

A characteristic feature of these alloys is the occurrence of an exothermic reaction during hydrogen absorption and an endothermic reaction during desorption [52]. Consequently, the temperature of the storage vessel increases during refilling and decreases during emptying. By thermally conditioning the storage system, it is possible to make the reaction more efficient, thus increasing the mass of hydrogen stored within the same volume of the container [53]. However, depending on the MH compound employed, high operating temperatures may be required to achieve efficient hydrogen release, which can be particularly energy-intensive [54, 55]. Naturally, thermal conditioning introduces additional energy consumption, which can reduce the overall system efficiency compared to unconditioned operation [56]. Nevertheless, this additional energy demand remains considerably lower than that of other storage technologies.

Another notable difference from compressed hydrogen storage lies in the absorption dynamics. When the hydrogen supplied is not a limiting factor (so in the case of unlimited power for the electrolyser), MHs inherently restrict the hydrogen uptake rate according to the degree of cylinder filling and the operating temperature [53, 57]. Furthermore, unlike compressed hydrogen storage, MHs continue to absorb hydrogen even after reaching their maximum pressure limit. Fig. 2.4 shows, as an example, the evolution of relevant physical quantities recorded during an MH filling test conducted in air. In this case, the maximum pressure corresponds to the highest value that the electrolyser can deliver. Since the electrolyser is connected to the grid, there are no inherent limitations on hydrogen production. Nevertheless, as shown, once the maximum pressure is reached, the cylinders progressively reduce the absorbed flow rate. Finally, as illustrated in Fig. 2.4b, the filling state of MH cylinders is not linearly correlated with pressure, unlike in the case of compressed hydrogen storage. The fill rate with this technology is expressed as a percentage of the gross weight of the storage system.

Given these advantages and the direct experience gained during this doctoral work, MH-based storage is the technology considered in this thesis.

2.3 Related Challenges

There are still several challenges hindering the large-scale development of hydrogen as an energy carrier. The most significant among these is undoubtedly the cost: current technologies rely either on rare and expensive materials for production or on complex and energy-intensive storage systems.

Regarding production, PEM technology is considered as a reference, since, as

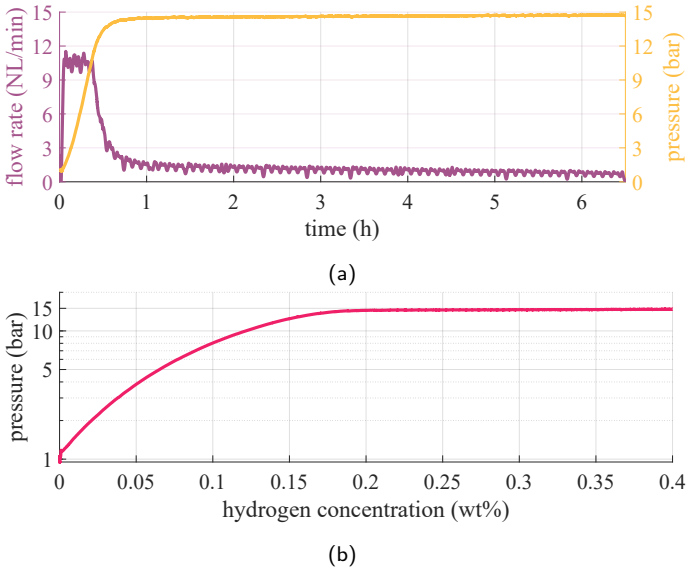

Figure 2.4: Trends of selected physical quantities during an MH cylinder filling test in ambient air: (a) flow rate and pressure vs time, and (b) cylinder fill fraction as a function of pressure.

previously discussed, it currently offers the most suitable characteristics for coupling with PV sources. However, this technology remains economically unfavorable due to the use of special materials required for the construction of electrolytic cells [58]. To better amortize the initial investment, a possible strategy is to extend the operational lifetime of the stack [59, 60]. Indeed, stack lifetime extension represents one of the most critical and actively investigated research topics in this field [61].

2.3.1 Effects of current ripple on PEM cells lifetime

In the last decade, it has been verified that one of the main factors reducing the lifetime of a PEM electrolytic cell is the presence of current ripple. This occurs because fluctuations in the current cause corresponding variations in the reactant flow rates, which can induce mechanical stress on the membrane. This phenomenon has been observed both when the cell operates as an electrolyser and as a fuel cell [62–64]. These studies have demonstrated accelerated aging in fuel cells and electrolysers subjected to current ripple, through characterization techniques such as polarization curves and electrochemical impedance spectroscopy. Two parameters play a key role in this degradation: the ripple frequency and its amplitude. Low-frequency ripple is generally more harmful than high-frequency ripple, while increased amplitude always has a negative impact [65].

Several works have investigated this phenomenon in greater detail. In [66], the effects of current ripple were analyzed across a frequency range from 100 Hz to

10 kHz. The experimental results obtained from impedance spectroscopy, reported in Fig. 2.5, showed that low-frequency ripple (100 Hz) causes premature cell degradation compared to higher-frequency operation. Similarly, [67] performed aging tests on PEM fuel cells under high-frequency ripple (20 kHz), concluding that such conditions do not significantly affect cell lifetime. Finally, in [65], the ripple impact was analyzed in terms of both membrane durability and efficiency. Tests with low-frequency ripple (50–400 Hz) showed a clear reduction in both membrane lifetime and performance.

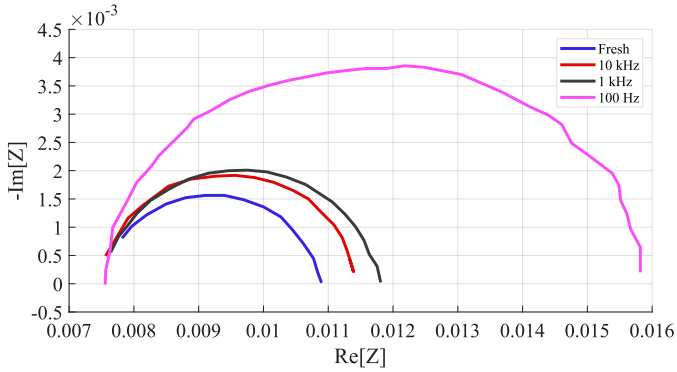

Figure 2.5: Impedance curves on single PEM cells obtained after cycling for 100 h at variable frequencies from [66].

2.3.2 Effects of current ripple on PEM cells efficiency

However, in addition to accelerating ageing, current ripple has also been shown to reduce cell efficiency [68, 69]. In [70], the effects of current ripple on electrolyser efficiency were experimentally investigated. The study found that ripple at frequencies on the order of a few hundred Hz causes a noticeable efficiency reduction, regardless of the waveform shape. Conversely, an increase in ripple amplitude consistently leads to a deterioration in performance.

Similarly, [71] examined the effects of ripple over a frequency range from 10 kHz to 50 kHz, varying the ripple amplitude at each frequency. Their results, reported in Fig. 2.6, showed a decrease in cell performance, evidenced by a reduction in output voltage, for all frequencies as the ripple amplitude increased. This effect was most pronounced at the lowest frequency tested (10 kHz).

A few studies have also attempted to model the ageing mechanisms induced by ripple [72]; however, the current literature in this area primarily focuses on fuel cells rather than electrolysers. Furthermore, it would be advisable to extend these studies in order to determine whether the aforementioned phenomena are interrelated or instead independent of one another [65].

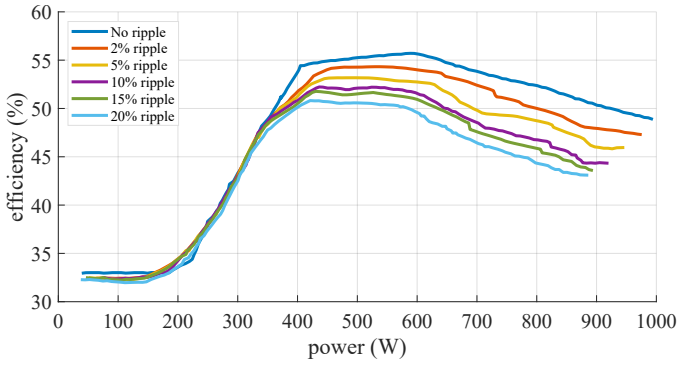

(a)

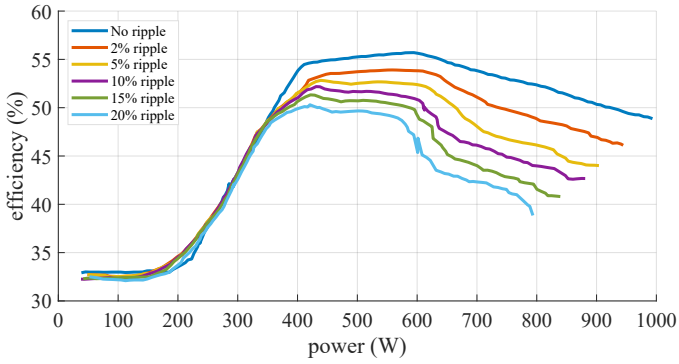

(b)

Figure 2.6: Fuel cell stack efficiency for: (a) 50 kHz ripple and (b) 10 kHz ripple from [71].

2.3.3 Hydrogen storage costs and safety

Despite significant advancements in electrolysis technologies, one of the major barriers to the widespread adoption of hydrogen as an alternative fuel remains its storage. As discussed previously, the current state of the art primarily relies on compressed hydrogen storage, which raises major safety concerns. High-pressure cylinders, often containing several hundred bar of highly reactive gas, require careful handling and continuous monitoring, leading to increased operational complexity and cost.

In the case of MH storage, the main limitations are currently related to the cost and weight of the systems. The high cost stems from the fact that this technology is relatively new and has not yet benefited from economies of scale. The second limitation is associated with the intrinsic density of the metal alloys used, whose weight is not negligible. Research is ongoing to develop lighter alloys capable of competing with batteries in terms of gravimetric energy density, which would enable the adoption of MH storage in the automotive sector. However, at present, its application remains confined mainly to stationary systems, such as the one considered in this thesis.

3

Electrolyser Power Electronic Converters

A direct coupling between a RES and an electrolyser, while cost-effective, often results in both operating under suboptimal conditions [73–75]. Power electronic converters, depending on their topology and control strategy, enable direct control of the system, thereby optimising overall performance and hydrogen production [12, 13].

As discussed in the Introduction, the current state of the art for powering electrolysers typically relies on both controlled and uncontrolled rectifiers. Several review papers have already analysed the AC/DC converters used for such applications [8–12]. However, this standard reliance on rectifiers is not optimal. Although they are mature and relatively inexpensive technologies, they suffer from issues related to harmonic distortion and reduced efficiency. Experimental tests conducted on commercial electrolysers have demonstrated that the overall system efficiency can be significantly limited by the converter, particularly when it is inadequately sized or based on outdated designs [57].

Regarding the scientific literature, several comprehensive review papers have been published in recent years on DC/DC converters for electrolyser applications [8, 11, 13, 14]. For stationary applications, the most desirable features are a high voltage conversion ratio, high efficiency, reliability (particularly in the event of power switch failures), and a low output current ripple to ensure optimal electrolyser performance.

Nonetheless, considerably fewer studies have addressed the coupling between PV systems and electrolysers. In most cases, the electrolyser's power source is modelled as ideal.

Fig. 3.1 shows the main types of connections considered to date in the literature concerning hydrogen production from PV. Each of these configurations has its own advantages and disadvantages. The diagram proposed in Fig. 3.1a, for example, does not allow separate control of the PV and the electrolyser. Therefore, either MPPT is performed, disregarding the behaviour of the electrolyser, or only

the electrolyser is controlled, considering the PV as an ideal source. The diagrams in Fig. 3.1b and Fig. 3.1c, on the other hand, allow for greater control freedom, but also greater system complexity, with the presence of multiple converters. In the following thesis, only the converter that interfaces with the electrolyser will be considered.

The following sections summarise the main works in the literature that have investigated converter solutions for coupling PV sources and electrolysers, considering both non-isolated and isolated topologies.

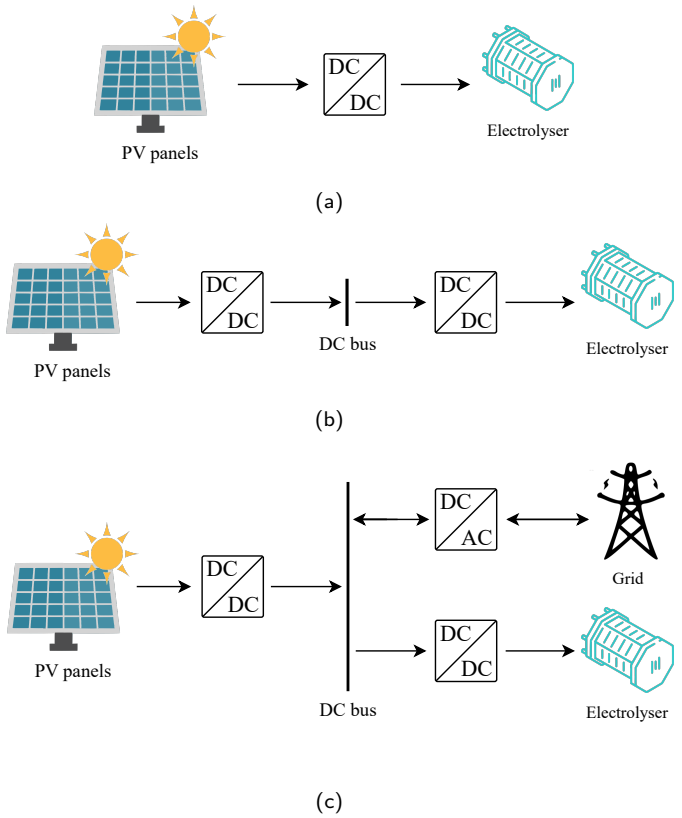

Figure 3.1: Possible configurations for hydrogen production from photovoltaic source: (a) PV panels connected to the electrolyser via a single converter, (b) PV panels connected to the electrolyser via a DC bus, and (c) PV panels connected to the electrolyser via a DC bus with the grid in parallel.

3.1 Non Isolated Converters

Non-isolated topologies refer to all converter configurations that lack galvanic isolation between the power source and the load.

The simplest possible configuration for coupling a PV system with an electrolyser (excluding direct coupling) employs a single DC/DC converter, as in

Fig. 3.1a. Depending on the voltage levels of the source and load, this converter can be either a buck or a boost. In most studies, however, a buck converter is selected since, as previously discussed, the electrolyser stack operates at relatively low voltages. Some works do not specify the topology in detail [76, 77], yet in the majority of single-converter studies, the chosen configuration is an asynchronous buck.

3.1.1 Asynchronous and synchronous buck

In [78], a mathematical model of a 500 kW system is developed, using the classical Perturb and Observe (P&O) algorithm to perform MPPT. Similarly, [79] adopts the same control approach for a 7 kW case study. Other studies that employ P&O for MPPT include [80] and [81], although these works focus on much smaller power ratings. In [82], a small-scale prototype (2 W) is implemented, aimed at providing a constant voltage to the load. In [83], a 5 kW electrolyser is analysed, with the control again targeting a constant output voltage. The study in [84] focuses less on mathematical modelling and more on converter control, employing a sliding mode control (SMC) algorithm. In [85] and [86], the Incremental Conductance (IC) method is used for MPPT in systems rated at 250 W and 1.5 kW, respectively. In [87], a 7.8 kW electrolyser is integrated into a hybrid energy storage system. The PV array is directly connected to the DC bus, and the system control combines a modified invasive weed optimisation algorithm with P&O. Finally, [88] also investigates a hybrid storage configuration, featuring a PV array directly connected to the DC bus and an electrolyser rated at 50 kW.

In Fig. 3.2, the circuit diagram of a synchronous buck converter is shown. The asynchronous version can be obtained by removing the lower switch and retaining only the diode. This fundamental topology theoretically allows the average output voltage V_{out} to be regulated between 0 and the supply voltage V_{in}, as expressed by:

$$V_{\text{out}} = DV_{\text{in}} \ , \tag{3.1}$$

where D is the duty cycle. However, the input current is inherently discontinuous, while the output current is smoothed by the presence of the inductor. The peak-to-peak output current ripple Δi_{Lpp} can be determined as:

$$\Delta i_{\text{out,pp}} = \frac{V_{\text{in}}}{L f_{\text{sw}}}(1 - D)D \ . \tag{3.2}$$

Eq. 3.2 highlights that the amplitude and frequency of the output current oscillations depend on the switching frequency f_{sw} and the selected inductance L. Except for the extreme cases where no switching occurs (i.e., $D = 0$ or $D = 1$), the output current always exhibits some level of ripple. Therefore, proper sizing of the reactive

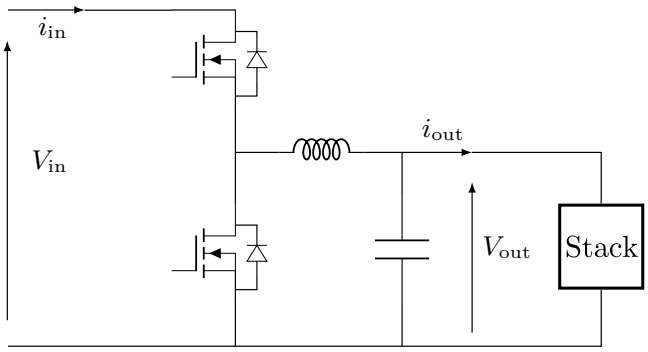

Figure 3.2: Circuit scheme of a synchronous buck converter.

components is essential to prevent harmful current fluctuations that could damage the electrolyser.

Furthermore, when a synchronous converter is employed, at low load conditions, the inductor current may become negative within a switching period due to the presence of ripple. Although this does not necessarily pose a problem for the electrolyser, since its electrical dynamics are significantly faster than its mechanical ones, it can justify the preference for using asynchronous converters. An additional advantage of asynchronous converters is their natural capability to operate in boundary conduction mode (BCM), thereby reducing switching losses.

To partially overcome the limitations associated with the single buck configuration, some studies have considered the use of two cascaded asynchronous buck converters [89].

3.1.2 Asynchronous and synchronous boost

Conversely, cases where a boost converter is employed are rarer. In these few instances, both asynchronous [90–94] and synchronous [95] boost topologies have been analysed. In such configurations, the situation is essentially the mirror image of the buck converter. Theoretically, the converter's output voltage can range from V_{in} to infinity, as expressed in:

$$V_{\text{out}} = \frac{V_{\text{in}}}{1 - D} \ . \tag{3.3}$$

In practice, however, conduction and switching losses limit this range, and the duty cycle must be constrained to prevent excessive losses and ensure proper converter operation. Furthermore, the current on the electrolyser side is discontinuous, while on the PV side it is smoothed by the inductor. Although this behaviour is not ideal for the electrolyser, since discontinuous current can accelerate degradation, it is beneficial for the PV source, as it enables more accurate implementation of MPPT control.

3.1.3 Interleaved buck

A well-known approach to reducing current ripple on the electrolyser side is the use of interleaved converter topologies. In [75], a 500 W synchronous interleaved buck converter with six legs is analyzed, while in [96], an asynchronous three-leg configuration is coupled to a 5.6 kW electrolyser. The circuit diagram of a generic synchronous interleaved buck converter with N legs is shown in Fig. 3.3. In general, these topologies exhibit the same input-output characteristics as the single-leg buck converter described in Eq. 3.1, but they enable a reduction of the output current ripple by a factor proportional to the number of legs employed. Under specific operating conditions, it is even possible to achieve complete ripple cancellation by appropriately phase-shifting the carriers of the gate signals.

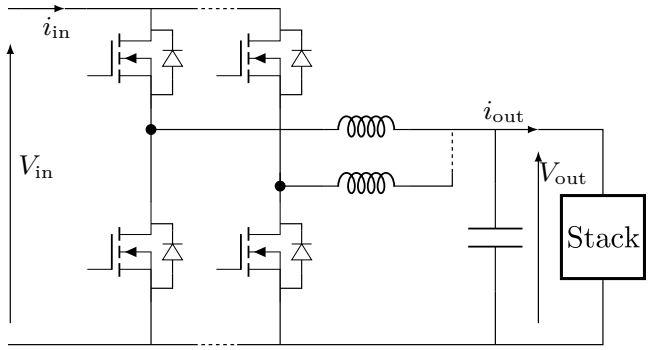

Figure 3.3: Circuit scheme of a synchronous interleaved buck converter.

In the synchronous interleaved buck converter, the output current is shared among all active legs. The phase of each leg current is uniformly shifted by an electrical angle of $360°/N$, while the upper and lower switches of each leg operate in a complementary manner. As a result, the amplitude of the output current ripple can be reduced by at least a factor of $1/N$.

3.1.4 Quadratic buck

Another converter topology considered, similar to the standard buck already discussed, is the quadratic buck [84]. This topology differs by incorporating an additional circuit section at the input stage. The circuit diagram of this topology is shown in Fig. 3.4. Such a configuration allows for a further reduction in output voltage for the same duty cycle. In this case, the input-output voltage relationship of the converter is:

$$V_{\text{out}} = D^2 V_{\text{in}} \ , \tag{3.4}$$

This advantage, however, is achieved at the cost of employing additional reactive

components, thereby increasing both cost and losses compared with the standard buck. The equation describing the output current ripple of the converter in this case is given by [97]:

$$\Delta i_{\text{out,pp}} = \frac{V_{\text{in}}}{L_2 f_{\text{sw}}}(1-D)D^2 \ , \tag{3.5}$$

where L_2 represents the inductance at the converter output port. The converter considered in this study is asynchronous and therefore benefits from operating in BCM.

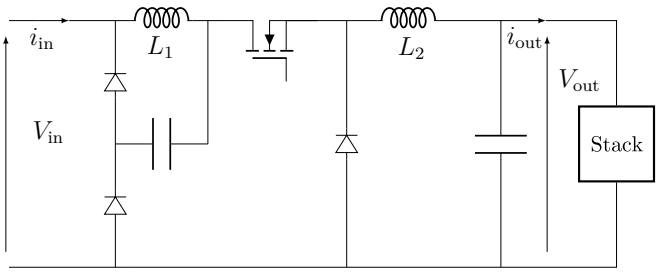

Figure 3.4: Circuit scheme of a quadratic buck converter.

3.1.5 Cùk

Other well-known topologies considered for coupling PV systems with electrolysers are the Cùk and the Single-Ended Primary-Inductor Converter (SEPIC) [98].

The Cùk converter offers improved current quality owing to the presence of inductors on both the input and output sides. This configuration enables the implementation of an accurate MPPT and ensures that the stack is supplied with continuous current. Furthermore, thanks to the presence of the diode, it can operate in BCM. The circuit diagram is presented in Fig. 3.5.

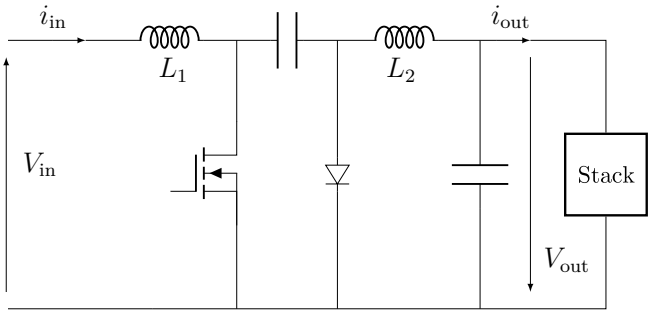

Figure 3.5: Circuit scheme of the Cùk converter.

The voltage input-output relationship for this converter is:

$$V_{\text{out}} = \frac{D}{1-D} V_{\text{in}} \ . \tag{3.6}$$

From Eq. 3.6, it can be observed that this topology can operate either as a buck or as a boost converter, depending on whether D is less than or greater than 0.5. In an application such as the one considered, however, once the PV system has been implemented and the stack selected (and therefore the voltage ranges defined), this results in constraining the duty cycle within a specific range.

Regarding the current ripple, the ripple on the output current can be expressed as:

$$\Delta i_{\text{out,pp}} = \frac{V_{\text{in}}}{L_2 f_{\text{sw}}} D \ , \tag{3.7}$$

where L_2 is the inductance on the output side of the converter. By exploiting the magnetic coupling between inductors, or by using other Cùk converter variants, it is theoretically possible to achieve ripple-free operation on both the input and output currents [99]. However, this comes at the expense of higher cost and greater design complexity. Another drawback of this topology is the inversion of the output voltage polarity.

3.1.6 SEPIC

The SEPIC converter exhibits characteristics similar to those of the Cùk topology but avoids the drawback of output voltage inversion. Its input-output voltage relationship is identical to that of the Cùk converter; therefore, the SEPIC can also operate as both a buck and a boost converter. However, this comes at the expense of output current quality, which becomes discontinuous since it is no longer smoothed by an output inductor. The circuit diagram of the SEPIC converter is shown in Fig. 3.6.

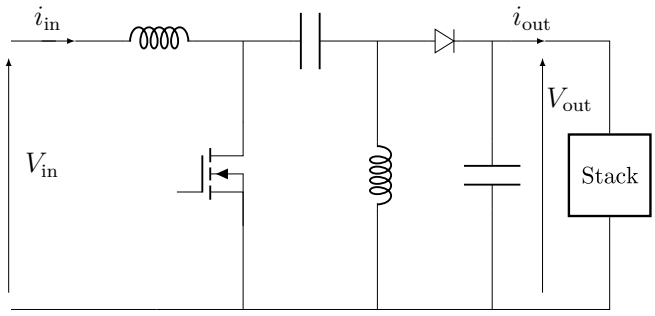

Figure 3.6: Circuit scheme of the SEPIC converter.

Both the Cùk and SEPIC converters require a higher number of components compared to the standard buck topology, as well as larger switch and diode ratings.

This is because, when the switch and the diode are not conducting, they are subjected to a voltage equal to $V_{\text{in}} + V_{\text{out}}$, while during conduction they must carry a current equal to $i_{\text{in}} + i_{\text{out}}$.

In [98], several control algorithms for both converters are compared. The P&O method is evaluated against a control strategy based on artificial neural networks (ANNs), showing that the latter achieves higher accuracy, albeit with greater computational complexity.

3.1.7 Stacked interleaved buck

Another topology considered for this type of application is the stacked interleaved converter. In [100], a stacked interleaved synchronous buck converter is proposed to supply a 400 W electrolyser. Its circuit diagram is shown in Fig. 3.7.

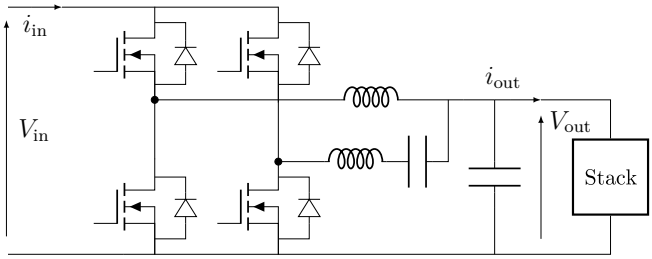

Figure 3.7: Circuit scheme of a stacked interleaved buck converter.

This converter resembles a synchronous interleaved buck with two legs but differs in the presence of a capacitor in series with the inductor of one leg, referred to as the cancellation leg. This configuration blocks the DC component of the current, allowing only the ripple component to pass through. By operating the converter so that the ripple current in the cancellation leg is in phase opposition to that of the main leg, total cancellation of the output current ripple can be achieved for any operating point. This aspect will be explored in greater depth later in the thesis. This characteristic is highly beneficial for the stack, although the input current remains discontinuous, as in the standard buck converter.

In [100], a dual closed-loop control strategy is implemented to regulate the output voltage to a specified reference value.

3.2 Non Isolated Grid-Connected Configurations

In most studies, the system is assumed to operate in off-grid mode, where all the energy produced by the PV source is directly supplied to the electrolyser, as in Fig. 3.1a. Accordingly, the control strategy is primarily designed to maximise energy transfer from the PV source to the electrolyser, thereby optimising hydrogen

production. The few studies that consider a grid-connected configuration as the one reported in Fig. 3.1c, typically involving a single converter for either the PV or the electrolyser, address more complex system architectures in which additional components such as fuel cells or batteries are integrated [86–88, 92, 93]. In most of these cases, the PV array is directly connected to the DC bus, and the converter is dedicated solely to powering the electrolyser, while MPPT is achieved by regulating the DC bus voltage.

The second configuration most frequently discussed in the literature consists of using one converter for the PV system and another for the electrolyser, as illustrated in Fig. 3.1b and in Fig. 3.1c. In this case, a greater variety of topological combinations is possible, as different converter types can be selected for each subsystem. Typically, this configuration employs a converter with a boost characteristic on the PV side and one with a buck characteristic on the electrolyser side [101–104].

In several studies, the specific topology adopted for one of the two converters is not explicitly stated [105–110], as the research focus may be placed on the load, the generation unit, or more generally on the energy management strategy of the entire system. Nevertheless, the most commonly employed configurations remain the asynchronous boost converter for the PV and the asynchronous buck converter for the electrolyser [111–116].

In some particular cases, identical converter types are adopted for both the PV and the electrolyser sides, such as generic boost converters [117], asynchronous buck converters [118], or three-leg synchronous interleaved buck converters [119]. A noteworthy example is presented in [120], where an asynchronous boost converter is employed for the PV and a stacked interleaved buck converter is used for the electrolyser.

The advantages and disadvantages of the various converter topologies have already been discussed. The use of dedicated converters is mainly motivated by the need to integrate them into more complex energy systems comprising not only the PV and the electrolyser, but also additional elements such as loads and storage units (e.g., batteries). In most cases, these microgrids are considered to operate in off-grid conditions; however, grid-connected configurations are also investigated in some studies.

The presence of dedicated converters enables independent management of each subsystem. This allows, for instance, the electrolyser to operate at its maximum efficiency point while the PV array follows its own MPPT. Such decoupled operation would not be possible without auxiliary storage systems or grid integration to compensate for instantaneous power mismatches between generation and consumption.

Therefore, despite the introduction of multiple conversion stages, these architectures offer greater flexibility and enable a more rational distribution of energy

flows among the different subsystems. Control strategies adopted for the converters can vary depending on the application or the study objectives, and no standardized approach currently exists. Generally, the converter interfacing the PV array performs MPPT, while the one supplying the electrolyser regulates the operation either to maintain a fixed hydrogen production rate or to absorb excess energy from the system.

3.2.1 Non isolated multi-port converter

A special case to be mentioned, which combines what has been said so far, is the use of multi-port converters. These topologies allow several components to be integrated via the same converter, such as PV, batteries, and electrolyser. At present, only one paper proposes a specific non-isolated topology explicitly designed for this type of application [121]. In this work, the authors introduce a non-isolated three-port converter that integrates a PV system, a PEM electrolyser, and a generic DC bus. The circuit diagram of the proposed topology is shown in Fig. 3.8. The converter operates as a boost stage toward the DC bus and as a buck stage toward the electrolyser stack. Its control strategy is based on satisfying the power demand of the DC bus, to which a load or an additional storage system may be connected, while directing only the surplus power, i.e., the portion not required by the DC bus, to the electrolyser. In this way, the converter simultaneously performs MPPT and activates the electrolyser power supply only when excess generation is available.

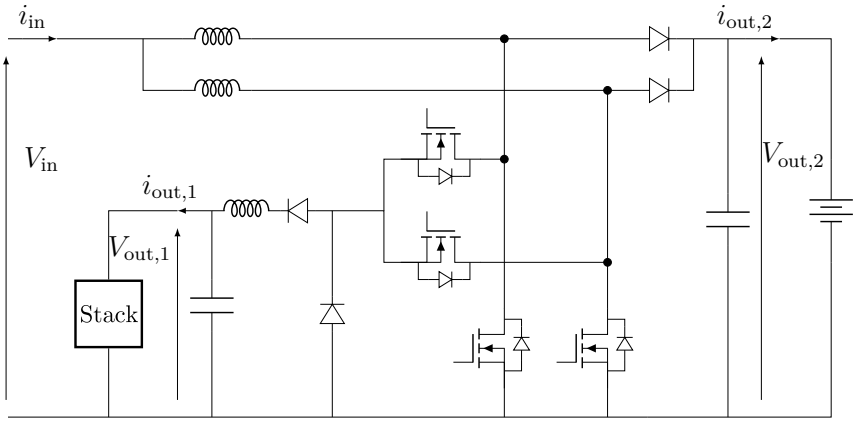

Figure 3.8: Circuit scheme of the multi-port converter presented in [121].

3.3 Isolated Converters

Isolated topologies include all converter configurations that incorporate some form of galvanic isolation. This isolation is typically achieved through high-frequency transformers, which allow a significant reduction in size and weight compared to traditional low-frequency transformers. Such an advantage becomes particularly relevant in high-power applications, such as large-scale electrolysers. In this category of converters, the input-output voltage relationship depends on the transformer's turns ratio n. Consequently, these topologies offer greater flexibility in selecting the conversion ratio, which is no longer strictly constrained by the duty cycle as in non-isolated converters. As with non-isolated systems, some studies consider only PV-electrolyser configurations, whereas others focus on microgrid applications. In certain works, the exact topology is not explicitly detailed, but only referred to in general as isolated converters [122, 123].

3.3.1 Dual active bridge

When considering systems composed solely of a PV source and an electrolyser stack, one of the most commonly adopted isolated converter topologies is the Dual Active Bridge (DAB) [124, 125]. The power ratings of the case studies presented in the literature for DAB-based applications range from 80 kW in [125] to 2.9 MW in [124].

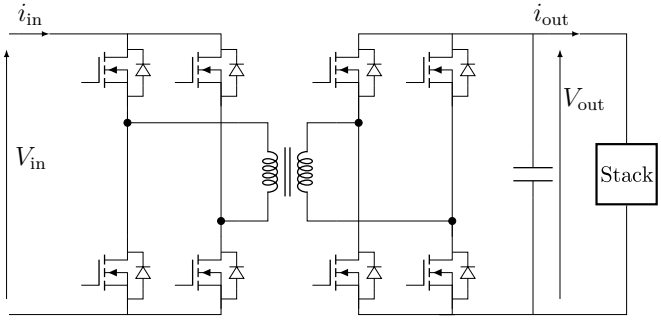

Figure 3.9: Circuit scheme of the DAB converter.

The DAB consists of two H-bridge converters separated by a high-frequency transformer, as shown in Fig. 3.9. Power transfer between the bridges is controlled by the relative phase shift between their switching signals. Depending on the direction of this phase shift, power can flow in either direction, making the converter inherently bidirectional, although this feature is not required for the application considered in this study. The relationship between the input and output voltages of the DAB depends on the duty cycles of both H-bridges and their relative phase shift [125]:

$$V_{\text{out}} = \frac{V_{\text{in}}}{n} X \ , \tag{3.8}$$

where X is a parameter that depends on the switching frequency and on the duty cycles of the two H-bridges. In [125], the influence of the three-phase shift modulation scheme used to control the DAB on current ripple is also analysed. The study shows that performing MPPT, which requires dynamic adjustments of the three phase-shift ratios, causes oscillations in the equivalent impedance on the primary side of the converter. As a result, the system exhibits reduced adaptability to photovoltaic fluctuations when coupled with a PEM electrolyser, leading to an increase in output current ripple.

3.3.2 Push-pull

Another isolated converter topology that has been investigated is the full-bridge converter followed by a push-pull stage, as analysed in [126], where a 19 kW system is considered as a case study. The corresponding circuit diagram is shown in Fig. 3.10.

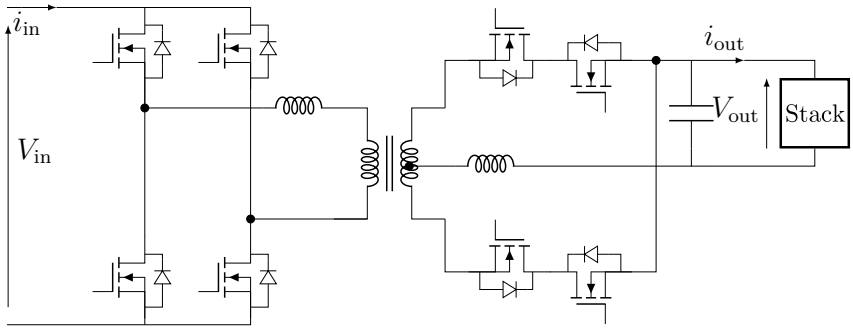

Figure 3.10: Circuit scheme of a full bridge at primary and a push-pull at secondary.

This converter allows bidirectional power flow, although this feature is not required in the present application. Moreover, it enables soft-switching operation of all semiconductor devices across a wide range of input voltages and power levels. In [126], unlike other cases previously discussed, the converter is not designed to perform MPPT but rather to operate the electrolyser at a fixed operating point. Consequently, this choice penalises the PV system, leading to suboptimal operating conditions and reduced overall efficiency.

3.4 Resonant Converters

Another major category of isolated converters is that of resonant converters. In addition to the high-frequency transformer, these topologies incorporate a network of reactive components arranged to form a resonant circuit operating at a specific frequency. The voltage transfer ratio of such converters can generally be expressed

as the product of three factors: the inverter bridge gain, the transformer turns ratio n, and the resonant tank gain K [127]. The coefficient K depends on the converter's design parameters, including the values of the resonant components and the ratio between the switching frequency and the resonant frequency.

Several studies have investigated isolated resonant topologies for coupling photovoltaic systems with PEM electrolysers. In these cases, a common trend is the use of multiple converters connected in series, even when the system consists solely of a PV source and an electrolyser stack. This represents a significant distinction from non-isolated topologies, in which multiple converters are typically employed only in more complex systems, such as microgrids. These architectures are hereafter referred to as multi-stage converters.

In [128], two different two-stage converter configurations are compared for a 5.5 kW case study, differing in the topology adopted for the first stage. In one configuration, the first stage implements a partial power processing topology, whereas in the other, it consists of a two-leg asynchronous interleaved buck converter.

In both configurations, the second stage consists of an LLC resonant converter implemented as a half-bridge on the primary side and a centre-tapped rectifier on the secondary side. For both cases, a P&O MPPT algorithm is employed to control the overall converter operation. The circuit diagrams of the two configurations are shown in Fig. 3.11 and Fig. 3.12a, respectively.

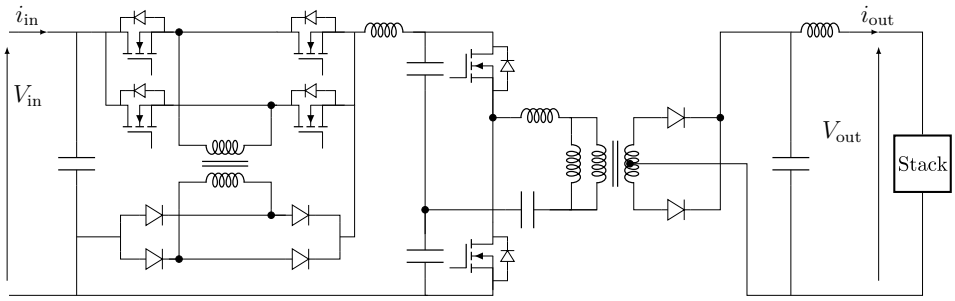

Figure 3.11: Multi-stage LLC resonant converter with partial power processing converter followed by a half-bridge at primary and a center tapped at secondary.

However, the focus of the article is on the overall efficiency of the converter; therefore, a comparison of the current quality on the stack side is not provided. It was demonstrated that, under low-load conditions, the system including the partial power processing stage achieves higher efficiency. This advantage, however, comes at the cost of increased circuit complexity, as it requires a greater number of components, including a second high-frequency transformer.

In [127], four different isolated two-stage topologies are compared for a 5 kW case study. In all configurations, the first stage is an asynchronous interleaved buck converter, while the second stage varies according to the specific topology considered.

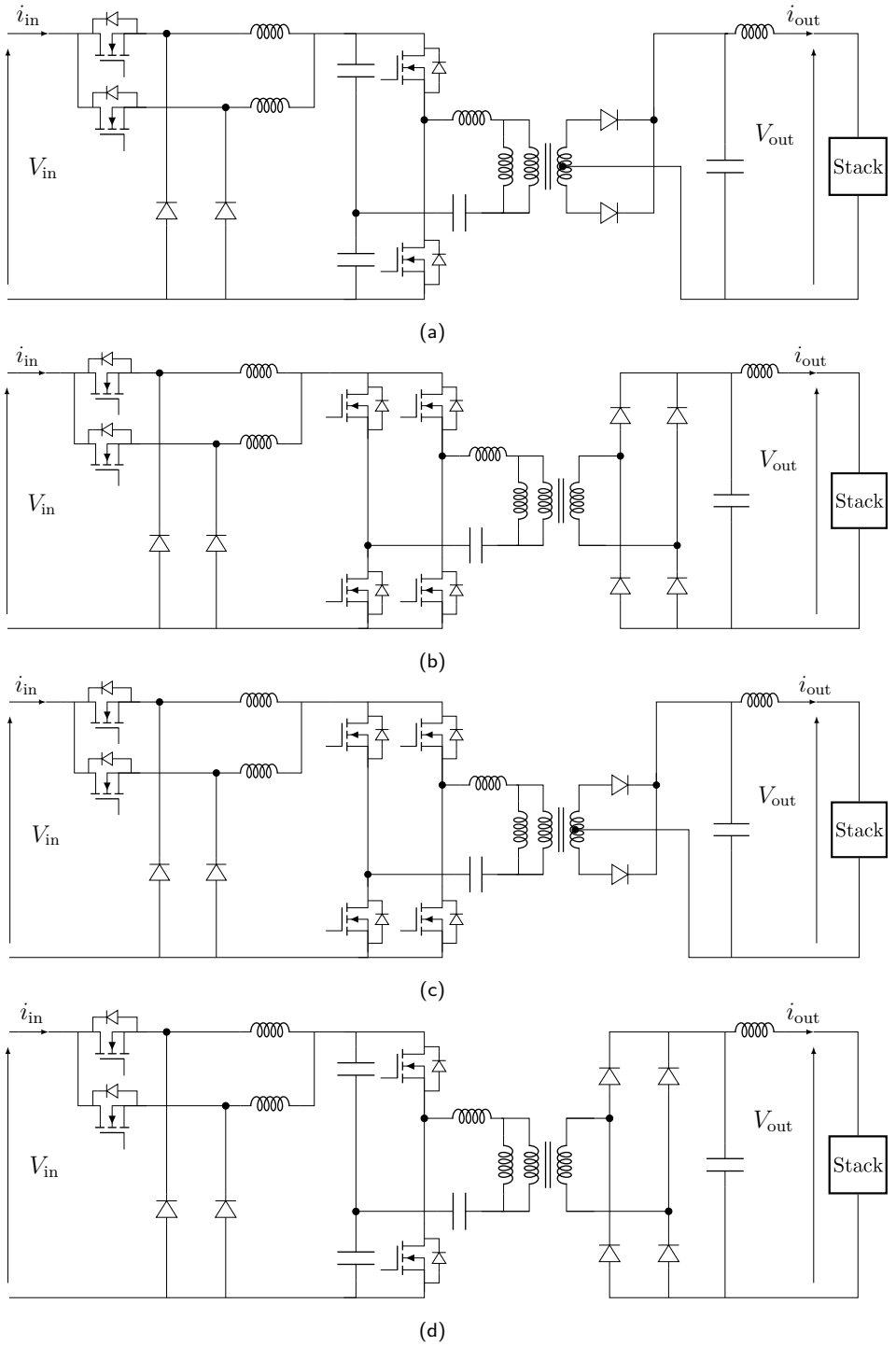

Figure 3.12: Different types of multi-stage LLC resonant converter with interleaved buck converter as the first stage: (a) half-bridge at primary and center tapped at secondary, (b) H-bridge at primary and diode rectifier at secondary, (c) H-bridge at primary and center tapped at secondary, and (d) half-bridge at primary and diode rectifier at secondary.

In the first configuration, an LLC resonant full bridge on the primary side and a diode rectifier on the secondary are employed, as shown in Fig. 3.12b. In the second configuration, the same full bridge is maintained on the primary side, but a centre-tapped rectifier is used on the secondary, whose circuit diagram is shown in Fig. 3.12c. The third configuration employs an LLC resonant half-bridge on the primary side and a diode rectifier on the secondary (Fig. 3.12d). Finally, the fourth configuration corresponds to the one previously discussed in [128] and is illustrated in Fig. 3.12a.

In this study, the purpose of employing multi-stage converters is to use them as single power modules within a multi-interleaved, multi-string PV system connected to a single high-power electrolyser. The first stage acts as a pre-regulator and is responsible for performing the MPPT, whereas the second stage ensures voltage matching (in this application, voltage reduction) and provides galvanic isolation. As in previous works, the focus of this paper is mainly on efficiency. It is shown that configurations adopting a centre-tapped topology in the second conversion stage exhibit superior performance from this point of view.

The input-output voltage relationship of the second stage in the various resonant converters already discussed can be classified into two groups. When the second stage employs an H-bridge, the inverter bridge gain is equal to 1, and the voltage conversion ratio is given by

$$V_{\text{out}} = V_{\text{in}} n K \ , \tag{3.9}$$

while in the case where the second stage consists of a half bridge, the inverter bridge gain is equal to 1/2, leading to the conversion ratio

$$V_{\text{out}} = \frac{1}{2} V_{\text{in}} n K \ . \tag{3.10}$$

In [129], a topology similar to that shown in Fig. 3.12b is proposed for a 10 kW electrolyser, with the difference that the converter stages are reversed: the resonant H-bridge stage followed by the rectifier is connected to the PV source, whereas the two-leg interleaved buck stage is connected to the electrolyser. In this case, the interleaved converter adopts a synchronous configuration.

Conversely, in [130], a converter corresponding to the scheme in Fig. 3.12b is investigated, but without the first stage, i.e., considering only the isolated resonant converter. The focus of that work is the comparison of different resonant tank configurations, demonstrating that among the various options, the LLC resonant tank is the most suitable for a 250 W electrolyser application. This is attributed to its ability to ensure lower switching losses and higher efficiency compared to the other configurations.

In [131], the multi-stage topology considered consists of an asynchronous buck converter, which performs the MPPT using a P&O algorithm, followed by a phase-shifted full-bridge converter with a centre-tapped secondary, used to interface with a 10 kW stack. The circuit diagram of this topology is shown in Fig. 3.13.

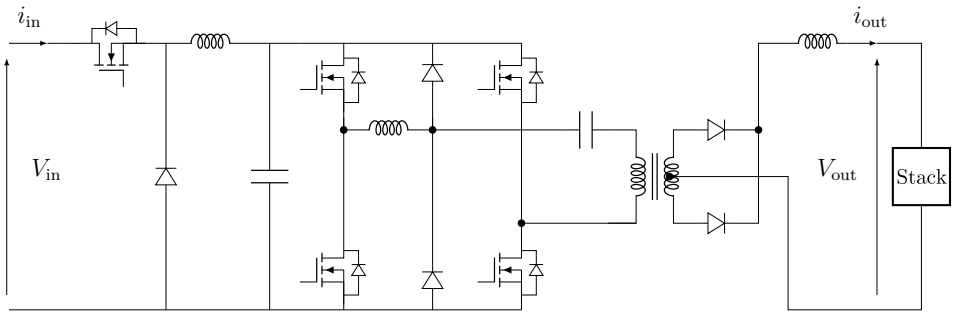

Figure 3.13: Multi-stage converter composed of a buck converter and a phase shift full bridge.

Even for isolated converters, when considering more complex systems, there may be cases where separate converters are employed for each component or multi-port converter architectures are adopted. As with non-isolated topologies, in microgrids where both the PV system and the electrolyser have dedicated converters, the exact topology of one or both converters is not always specified. For example, in [132], the converter topology responsible for performing the MPPT is not indicated, while for the electrolyser a full-bridge converter is used on the primary side and a double-current rectifier on the secondary.

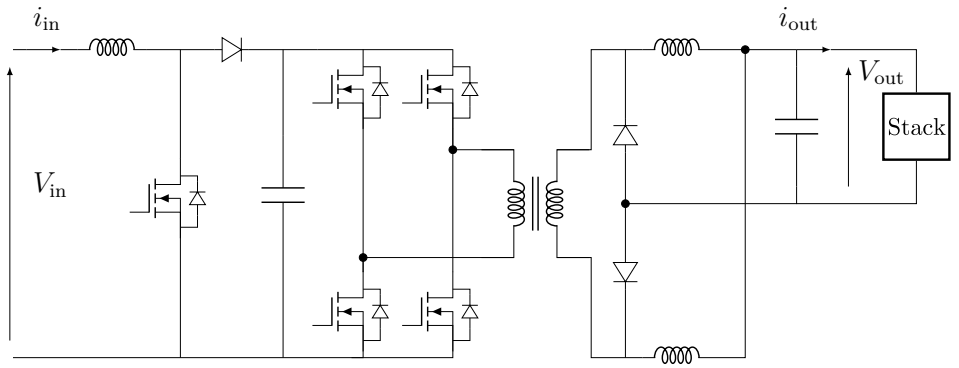

Figure 3.14: Multi-stage converter composed of a boost converter and an isolated full bridge.

In [133], an asynchronous boost converter is used for the PV, while for the electrolyser the topology shown in Fig. 3.14 is considered. The case study involves a 1.5 MW plant. The boost converter performs the MPPT using the IC algorithm, while the isolated converter regulates the voltage applied to the stack. In this work, no additional storage system is connected in parallel with the electrolyser, allowing

the DC bus voltage to vary according to PV power fluctuations. This approach protects the stack from abrupt power transients but requires an oversizing of the capacitors on the DC bus to maintain stability.

3.4.1 Isolated multi-port converters

In [134], a 500 W multi-port topology specifically designed for the integration of PV, battery, and electrolyser subsystems is proposed. The circuit diagram of this topology is shown in Fig. 3.15a. On the primary side, an H-bridge operates both as a synchronous interleaved buck converter for the battery and as an LCC resonant converter for the stack. On the secondary side, an uncontrolled rectifier is employed. The desired voltage on the port connected to the battery is obtained through the duty cycle computed from the MPPT, while the voltage on the port connected to the stack is regulated by controlling the switching frequency. The relationship between the input voltage from the PV and the output voltage on the stack can be expressed as:

$$V_{\text{out}} = \frac{V_{\text{in}}}{n} \frac{64 f_{\text{sw}} \sin(D\pi)}{K} \ , \tag{3.11}$$

where K is a coefficient that depends on the converter design parameters, such as the ratio of the resonant capacitances, but also on the ratio of switching frequency to resonance frequency. This configuration allows the operation of the PV and the stack to be controlled independently, enabling MPPT for the PV while the electrolyser operates at a desired power level. The current ripple on the stack for this topology is given by:

$$\Delta i_{\text{out,pp}} = \frac{V_{\text{out}}}{L_{\text{out}} f_{\text{sw}}} \left\{ \frac{1}{2} \left[\cos\left(\arcsin \frac{2}{\pi} \right) - 1 \right] + \frac{1}{\pi} \left(\arcsin \frac{2}{\pi} \right) \right\} \ . \tag{3.12}$$

Since the output voltage is primarily controlled by the switching frequency, the ripple of the current flowing through the stack depends less on the duty cycle.

In [135], the multi-port configuration is instead achieved through a specially designed three-winding transformer. The converter is implemented using three three-phase inverters, as shown in Fig. 3.15b. The battery on the third port is included for illustration purposes, but this port could also be connected to the grid. The three-phase inverter is a well-known, simple, and modular topology that can be integrated into both off-grid and grid-connected systems, depending on the control strategy. However, the use of a three-winding transformer generally increases design complexity and cost compared to two-winding alternatives.

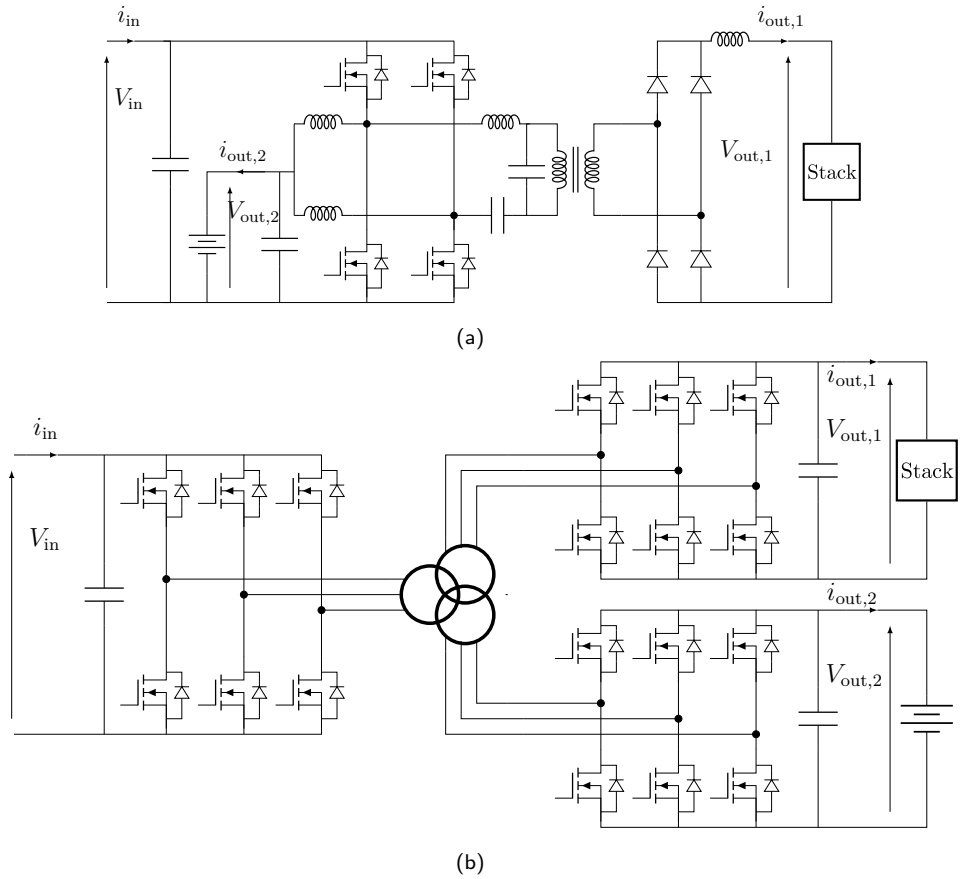

Figure 3.15: Different types of isolated multi-port converter: (a) circuit scheme presented in [134], and (b) circuit scheme with the three-winding transformer presented in [135].

3.5 Discussion on PV-Electrolyser Converters

Regarding the converter topology adopted for hydrogen production from PV, the choice between an isolated and a non-isolated converter is not always directly related to whether the system is grid-connected or standalone. Since electrolysers generally operate at low voltages, the inclusion of transformers in isolated converters allows achieving higher conversion ratios between input and output voltages compared to non-isolated ones. This offers greater design flexibility and enables better voltage matching between the PV generator and the electrolyser stack. However, this benefit comes at the cost of increased converter complexity, larger volume, and higher manufacturing cost, mainly due to the need for a high-frequency transformer, which is a critical and often expensive component.

When focusing on systems composed solely of a PV array and an electrolyser stack, in most cases, a single converter is preferred to minimize conversion losses and system cost. Although certain studies, especially those dealing with isolated

topologies, consider multi-stage converters, these configurations remain limited because each additional stage introduces further conversion losses and reduces the overall efficiency of the system. Nevertheless, multi-stage architectures can still be advantageous when considered as modular power units within multiple interleaved or multistring PV configurations connected to a single high-power electrolyser. In such scenarios, each module can perform local MPPT, ensuring optimal energy extraction from each PV string, while collectively providing stable operation for the stack.

In most single-converter configurations, the converter performs MPPT control to maximize energy transfer from the PV system to the electrolyser, thereby maximizing hydrogen production. This approach, however, leads to an intermittent operating profile for the electrolyser, as it becomes directly dependent on PV power fluctuations. Conversely, a few studies propose control strategies that prioritize the protection and longevity of the electrolyser by ensuring constant power operation. In these cases, the converter works to maintain a stable load on the stack, which benefits its lifespan and efficiency, but at the expense of the PV operating below its maximum power point. This results in reduced conversion efficiency and potential overheating of the PV panels, which over time can accelerate degradation and reduce their effective output capacity.

More complex configurations, such as hybrid or microgrid systems, have also been widely studied. In most of these, dedicated converters are used for both the PV array and the electrolyser, allowing for independent control of each component. Typically, non-isolated topologies are preferred for such systems due to their simplicity, lower cost, and high efficiency. However, in certain cases, only one converter, either on the PV or electrolyser side, is used, with both connected to a common DC bus whose voltage is regulated by the overall energy management system. This configuration enables a higher degree of flexibility and a more intelligent distribution of power flows. It allows the PV to always operate at its optimal point via MPPT, while the electrolyser can function in a smoother, more continuous regime, protected from abrupt power variations. The trade-off is an increase in system cost and complexity, as these architectures often require additional components such as energy storage systems (e.g., batteries or supercapacitors) to balance instantaneous power mismatches.

For a broader evaluation of the cost and reliability of the different converter topologies, a useful simplification is to consider the number of components used. Although the reliability of a power converter depends on many factors, such as component quality, thermal design, and control complexity, it is not always true that a larger number of components reduces overall system reliability [136–138]. Similarly, cost does not scale linearly with the number of components, since certain topologies, such as interleaved converters, allow current and thermal stresses to be distributed among multiple phases, enabling the use of smaller and more

cost-effective components. Nevertheless, the total component count remains a useful indicator of the relative complexity and potential cost of a given topology.

Table Tab. 3.1 summarizes the number of components required for each converter topology discussed in this section. For interleaved topologies, the general case with N legs is considered. When counting diodes, freewheeling diodes have not been included, as they may either be integrated within the switching device or omitted in certain designs. Additionally, the table provides an overview of the control strategies adopted for each converter and the corresponding power range of the application considered.

Table 3.1: Main Characteristics of the Various Converters Considered

Topology	**Reference**	**Transformer**	**S/D/L/C**	**Control**	**Power Range**
Asynchronous buck	[78–88]	No	1/1/1/1	P&O, IC, SMC, Fixed V_{out}	2 W – 500 kW
Asynchronous boost	[90–94]	No	1/1/1/1	P&O	1 – 200 kW
Asynchronous interleaved buck	[96]	No	N/N/N/1	SMC	5.6 kW
Synchronous interleaved buck	[75]	No	2N/0/N/1		500 W
Quadratic buck	[84]	No	1/3/2/2	SMC	330 W
Cùk	[98]	No	1/1/2/2	P&O, ANN	
SEPIC	[98]	No	1/1/2/2	P&O, ANN	
Synchronous stacked interleaved buck	[100]	No	4/0/2/2	Fixed V_{out}	400 W
Non-isolated multi-port	[121]	No	4/4/3/2		
DAB	[124, 125]	Yes	8/0/0/1		80 kW – 2.9 MW
Full bridge/push-pull	[126]	Yes	8/0/2/1	Fixed V_{out}	19 kW
Multi-stage with partial power processing	[128]	Yes	6/6/4/4	P&O	5.5 kW
Multi-stage half-bridge/center tapped	[127, 128]	Yes	4/4/5/4	P&O	5 – 5.5 kW
Multi-stage H-bridge/center tapped	[127]	Yes	6/4/5/2		5 kW
Multi-stage H-bridge/diode rectifier	[127]	Yes	6/6/5/2		5 kW
Multi-stage half-bridge/diode rectifier	[127]	Yes	4/6/5/4		5 kW
Multi-stage with synchronous interleaved buck	[129]	Yes	8/4/3/4		10 kW
H-bridge/diode rectifier	[130]	Yes	4/4/2/2		250 W
Multi-stage phase shift full bridge	[131]	Yes	5/5/3/2	P&O	10 kW
Multi-stage asynchronous boost/isolated full bridge	[133]	Yes	5/3/3/2	IC	1.5 MW
Isolated multi-port	[134]	Yes	4/4/4/4	Fixed V_{out}	500 W
Isolated multi-port with 3 winding transformer	[135]	Yes	18/0/0/3		

S = Switches; D = Diodes; L = Inductances; C = Capacitors

As can be seen from Tab. 3.1, in many converter topologies, the number of diodes and switches used depends primarily on whether the configuration is asynchronous or synchronous. In asynchronous designs, each leg requires an additional diode to provide the freewheeling path during the switch-off period, while in synchronous converters, this function is performed directly by the controlled switch. In general, for all topologies that employ interleaved configurations, the number of total components (both active and passive) scales with the number of legs used. This is an expected outcome, as increasing the number of legs enables current ripple reduction and improved thermal distribution, but at the cost of higher circuit complexity and control requirements.

The converter families that require the greatest number of reactive components are the isolated resonant topologies. This is due to the inclusion of multiple inductors and capacitors that form the resonant tank, which allows the converter to achieve soft switching and higher efficiency at high frequencies. However, these same components contribute to greater system bulk and cost. Even among non-isolated topologies, some variants, such as the Cùk or SEPIC converters, employ a larger number of reactive elements compared to simpler configurations like the buck or boost converters. Nonetheless, the quantity of these additional components remains considerably lower than in isolated resonant topologies. It can therefore be reasonably concluded that isolated resonant converters, particularly those involving complex transformer-coupled stages, are among the most expensive and volumetrically demanding solutions for PV-powered hydrogen generation systems. This higher cost and size are not only attributable to the transformer but also to the additional resonant elements and the need for precise component matching.

Another observation that emerges from Tab. 3.1 concerns the control techniques adopted. When explicitly specified, most converters rely on traditional and well-established MPPT algorithms such as P&O or IC. These algorithms are preferred because of their simplicity, robustness, and proven effectiveness in a wide range of PV applications. However, a few studies have experimented with more advanced or intelligent control strategies, such as those based on ANNs or fuzzy logic, which have demonstrated improved tracking accuracy and dynamic performance.

Following this analysis, a comparative study of the output current ripple as a function of the duty cycle is presented for all converter topologies for which analytical expressions are available. For fairness in comparison, identical parameters, such as switching frequency, input voltage, and inductance values, are used for all cases. Topologies in which the load current is inherently discontinuous or not leveled (e.g., SEPIC) are excluded from this comparison, as they are considered less suitable for directly supplying electrolysers due to the resulting performance degradation and increased stress on the stack.

As previously discussed, and as illustrated in Fig. 3.16, several topologies

exhibit operating points (specific duty cycle values) at which the output current ripple theoretically cancels out. Among all analyzed configurations, the stacked interleaved buck offers the best performance, achieving complete ripple cancellation under appropriate phase-shift conditions between the power legs and cancellation leg. The quadratic buck converter also shows superior performance compared to the standard buck across the entire duty cycle range, and for lower duty cycles, it even outperforms a six-leg interleaved buck. Regarding the Cùk converter, it should be recalled that its duty cycle range is inherently limited by the design parameters and chosen operating mode (either $0 - 0.5$ when functioning as a buck or $0.5 - 1$ when acting as a boost) thus constraining its operating flexibility despite its favorable ripple characteristics.

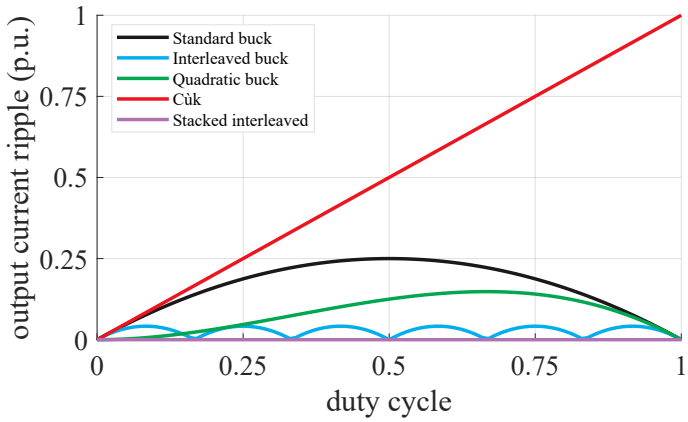

Figure 3.16: Comparison of normalized output current ripple amplitude as a function of the duty cycle.

Therefore, based on the considerations discussed so far, it can be concluded that the stacked interleaved buck converter represents the most suitable topology for supplying a PEM-type electrolyser, as it enables the achievement of zero output current ripple over the entire load range. This characteristic is a fundamental requirement for the reliable operation and long-term durability of a PEM-type electrolyser, and the additional cost with respect to a conventional interleaved buck converter can be justified by the resulting performance benefits. Conventional buck and boost converters are unable to satisfy this requirement, while standard interleaved configurations can only achieve ripple-free operation at specific operating points. As will be shown later, their effectiveness is therefore strongly dependent on the number of active legs and on the voltage constraints of the system. Similarly, quadratic buck, Ćuk, and SEPIC converters do not inherently provide operating conditions with zero output current ripple. In the case of the Ćuk topology, ripple cancellation may be achieved only through the implementation of specially designed magnetic circuits, whose increased complexity can lead to a significant rise in cost

and design effort. Finally, isolated and resonant converter topologies generally entail higher costs compared to non-isolated solutions, making them less attractive from an economic perspective. Nevertheless, in specific applications or at particular voltage levels, they may represent the only viable option and therefore cannot be entirely disregarded.

4

Stacked Interleaved DC/DC Buck Converter

As discussed in Chapter 3, current ripple significantly accelerates the degradation of PEM cells. Consequently, numerous studies in the literature have proposed converter topologies and control strategies aimed at mitigating this issue, with a comprehensive review provided in [139]. However, in most cases, these approaches achieve ripple reduction or complete ripple cancellation only at specific operating points [140]. With the topology considered in [141], for example, ripple cancellation is achieved only for specific duty cycles, while in [142] cancellation is achieved only on $D = 0.5$. Some converter topologies are capable of eliminating ripple across the entire operating range [143], provided that certain design constraints are satisfied; nonetheless, they often suffer from limited modularity and reduced efficiency. For example, in [144], current ripple is cancelled only if the inductors comply with certain design parameters. Also, the topology proposed in [145] aims to use coupled inductors to cancel current ripple, but this condition only occurs if these inductors comply with a specific design. Another example is the topology proposed in [146], which allows current ripple to be cancelled under any operating conditions, but has an average experimental efficiency of less than 92%.

In contrast, interleaved topologies inherently offer advantages in terms of modularity and efficiency [147]. Although the interleaved buck architecture naturally reduces output current ripple due to its phase-shifted operation, achieving complete ripple elimination across all operating conditions remains a major challenge in the design of converters for PEM electrolysers. For electrolyser applications, the suppression of output current ripple is crucial, as it directly influences the system's long-term reliability and efficiency, preventing premature degradation and extending the operational lifetime of the hydrogen production system.

Therefore, based on what has already been seen in the previous Chapters, it has been chosen to focus on the study of the synchronous stacked interleaved

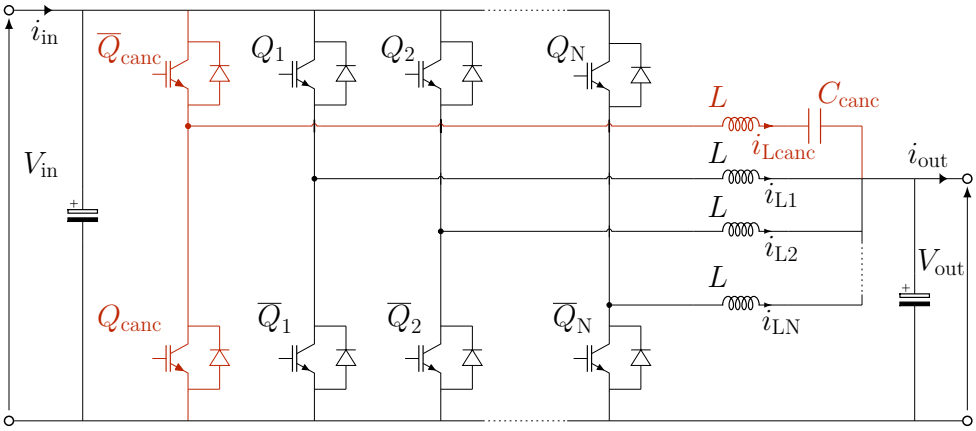

Figure 4.1: General circuit schematic of a synchronous stacked interleaved buck converter with N legs, with the cancellation leg highlighted in red.

buck converter (SSIB), a modular topology capable of achieving complete current ripple cancellation across all operating points. Its modular nature also enables the application of efficiency-improving strategies, such as phase shedding. A schematic of this topology is presented in Fig. 4.1.

As previously mentioned and now generalized, the SSIB can be regarded as a synchronous interleaved buck (SIB) converter with an additional leg (highlighted in red). This additional leg, referred to as the cancellation leg, differs from the others by including a capacitor in series with the inductor. Its detailed operating principle will be discussed in the following section.

An example of such a converter used as a buck was described in [148]. The simplest configuration was considered in that case, with only one power leg. A generalisation of this type of converter to the case where there are N power legs was well described in [149]. Other articles have also considered and discussed this converter topology, perhaps considering the cancellation leg as an external circuit [150] or making modifications to it [151]. All these works consider as a source an ideal power source. As already mentioned in the previous Chapter, in [100] it was analyzed in conjunction with a PV system but only using a single power leg. Finally, in [152] this topology was analyzed as a boost converter.

In this work, a modulation strategy for the SSIB is proposed to achieve a ripple-free current on the electrolyser while minimizing the number of active components. This is accomplished through phase shedding to maximize converter efficiency and by selectively enabling or disabling parts of the SSIB architecture.

4.1 Interleaved Buck Converters

For an N-leg SIB converter, the current in each leg is phase-shifted by an electrical angle of $360°/N$, ensuring that the total current is evenly distributed among all active legs. As discussed in the previous Chapter, this configuration leads to a reduction in the output current ripple by at least a factor of $1/N$.

The peak-to-peak ripple of the output current, $\Delta i_{\text{out,pp}}$, for a buck converter under any operating condition is given by [153]:

$$\Delta i_{\text{out,pp}} = \frac{V_{\text{in}}}{L f_{\text{sw}}} \left[1 - N\left(D - \frac{p-1}{N}\right)\right]\left(D - \frac{p-1}{N}\right) \ , \tag{4.1}$$

where V_{in} is the input voltage, f_{sw} is the switching frequency, L is the inductance per leg of the converter, D is the duty cycle, and p is a natural index ranging from 0 to N, defined as:

$$p = \text{ceil}(ND) \ . \tag{4.2}$$

Consequently, there are $N + 1$ operating points at which $\Delta i_{\text{out,pp}}$ becomes zero. In other words, an SIB converter exhibits $N + 1$ ripple-free operating points. Specifically, as can be seen in Fig. 4.2a, the naturally ripple-free points are those where $D = i/N$, where $i = 1, ..., N$.

Even in cases where the overall output current appears ripple-free, the individual converter legs still experience a non-zero current ripple. This is an intrinsic characteristic of interleaved topologies, where the cancellation occurs due to the phase-shifted contributions of each leg rather than the elimination of ripple at the leg level. The peak-to-peak ripple for each leg is the same already seen in the previous Chapter for the single buck. From Eq. 3.2 and as can be seen in Fig. 4.2b, it is evident that a leg current ripple exists for any duty cycle strictly between 0 and 1, i.e., whenever switching occurs. The number of legs is totally irrelevant in this case; in fact, the various cases shown in the graph Fig. 4.2b overlap perfectly. Only in the extreme cases of $D = 0$ or $D = 1$, corresponding to a leg being fully off or fully on, does the ripple vanish entirely. This highlights the importance of interleaving multiple legs to achieve ripple cancellation at the output while accepting that the ripple within each individual leg remains an unavoidable phenomenon.

4.2 Ripple Cancellation Via Software

To achieve ripple cancellation, the SIB converter can be operated exclusively at the duty cycles corresponding to the ripple-free points. This approach allows the use of only the essential components, as the cancellation leg becomes unnecessary. Such a technique has already been explored in [153] and in [154].

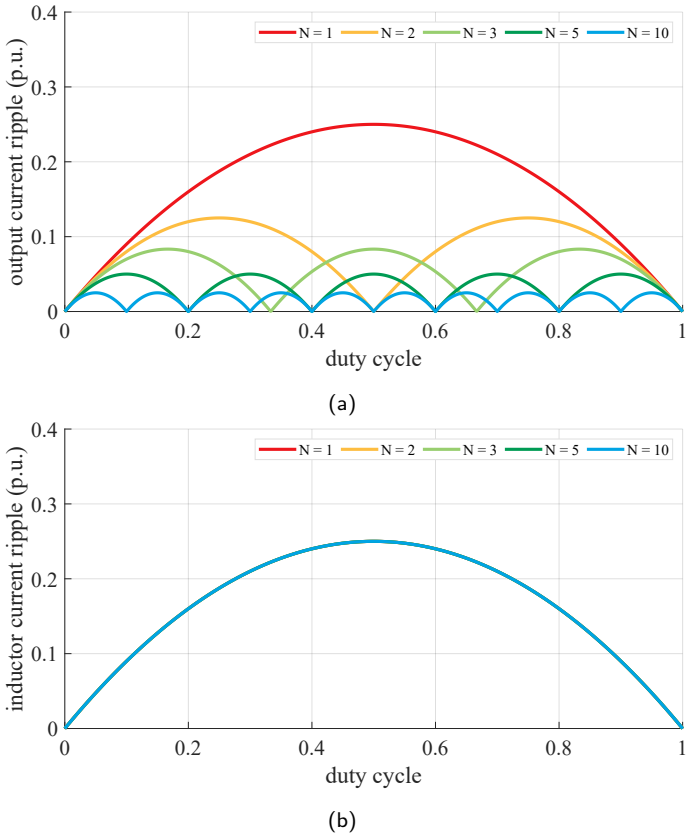

Figure 4.2: Current ripple amplitude in an interleaved buck converter as a function of duty cycle for different numbers of legs: (a) output current, and (b) single leg current.

It is reasonable to assume that the input voltage of a PV generator can vary within certain limits, as some PV panels may be shaded. These limits obviously depend on the series-parallel arrangement of the panels and are a degree of freedom when designing the system. The voltage applied to the electrolyser, as defined by its polarisation curve, can also be adjusted to regulate the rate of hydrogen production. Once the electrolyser type, size, and polarisation curve are known, the PV generator can be appropriately sized. In this context, the PV system is considered to possess a higher degree of design flexibility compared to the electrolyser stack, since PV panels can be configured in multiple series-parallel arrangements. In contrast, the construction parameters of the electrolyser stack are typically fixed by design and manufacturing constraints. After determining the voltage levels of both the PV system and the electrolyser, it becomes possible to calculate the minimum number of legs, N_{min}, that the converter must include to ensure ripple-free operation:

$$N_{\text{min}} = \text{ceil}\left(\frac{V_{\text{in,min}}}{V_{\text{out,min}}}\right) . \tag{4.3}$$

The tighter the voltage variation limits, both at the input and at the output, the

higher the number of legs required [154, 155]. Fig. 4.3 shows the input-output relationship of a 12-leg SIB converter, considering different input voltage ranges, highlighted by the red dotted vertical lines. The output voltage range is considered constant as the same stack is used. As can be seen from the areas highlighted in red, more stringent input voltage limits lead to the formation of zones where the load cannot operate ripple-free, as there are no duty cycles that naturally cancel out the ripple. Therefore, if the input voltage must remain within strict limits for various reasons, there may be operating points where the output current will not be ripple-free.

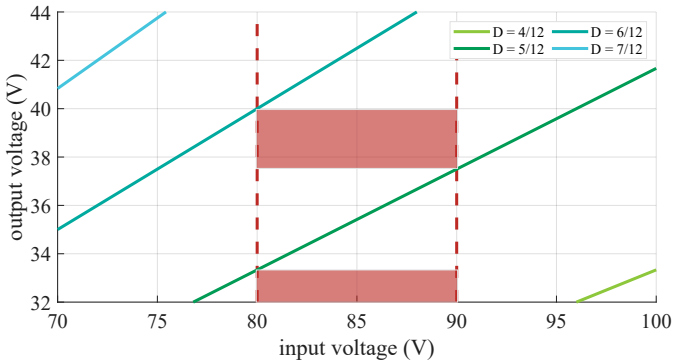

Figure 4.3: Comparison between different input voltage limits (the dashed lines refer to tighter limits) with the same number of legs $N = 12$.

Another aspect to consider is that the number of possible ripple-free operating points is directly proportional to the number of legs N. Thus, as already mentioned, achieving greater flexibility and a higher number of ripple-free operating points would require increasing the number of legs [154]. Fig. 4.4 shows a comparison between two possible configurations: one with $N = 6$ and one with $N = 12$. The comparison is made with the same voltage range, both at the input and output. As can be observed from Fig. 4.4, when identical voltage limits are imposed on both the input and the output sides, changing the number of converter legs leads to a different set of ripple-free duty cycles. When the number of legs is reduced, situations may arise in which, for a given input voltage value, no duty cycle exists that guarantees ripple-free operation at the output. For instance, as shown in Fig. 4.4b, for every value of the input voltage there exists at least one ripple-free duty cycle that allows an output voltage within the prescribed limits to be obtained. Conversely, this condition is no longer satisfied for all input voltage values in the case illustrated in Fig. 4.4a. A similar consideration can be made when analysing the system from the load perspective. For a given desired output voltage, there may exist multiple duty cycles, and therefore multiple admissible input voltages, that result in the same output condition, as clearly illustrated in Fig. 4.4b. In contrast, in the case depicted

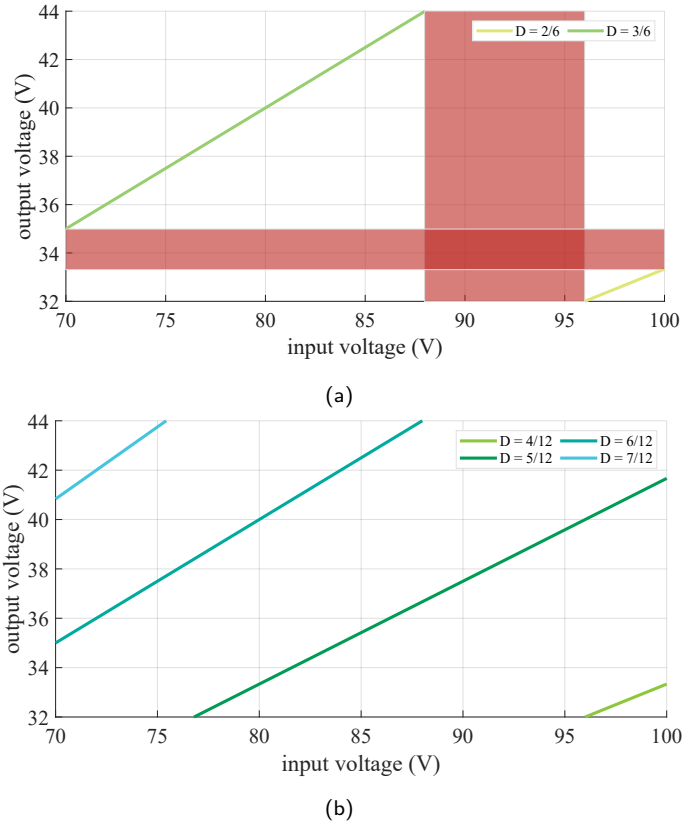

Figure 4.4: Voltage input-output relations with different number of legs: (a) 6 legs, and (b) 12 legs.

in Fig. 4.4a, there exists a region of output voltage values for which no ripple-free duty cycle is available at all. These observations highlight how the achievable ripple-free operating range is strongly dependent on the number of converter legs, as well as on the imposed voltage limits, and underline the importance of an appropriate selection of the converter modularity during the design stage.

With this technique, the converter therefore operates at a constant duty cycle. Of course, the preferred duty cycle is the one that minimizes the inductor current ripple as well as voltage stress on the system components. If it required a specific output voltage V_{out}, the optimal duty cycle can be determined as:

$$D = \frac{\text{floor}\left(\frac{NV_{\text{out}}}{V_{\text{in,min}}}\right)}{N} \,. \tag{4.4}$$

Obviously, with this technique, any variation in the input voltage will cause a corresponding change in the output voltage.

4.3 Ripple Cancellation Via Hardware

If the converter's output voltage must remain constant despite variations in the input voltage, operating at a fixed duty cycle is no longer feasible. Furthermore, if the number of legs used were to be varied in order to improve efficiency, one could end up operating in areas where there are no duty cycles that allow ripple-free operation. This is because, as already mentioned, reducing the number of legs used also reduces the number of possible ripple-free points. An exceptional case to consider would be that of a converter with a single leg, in which ripple-free operation would be impossible to achieve. This is because with only one leg, interleaving is completely lost, while for a number of legs less than $N_{\min}$, load conditions are created in which there are no duty cycles (from Eq. 4.4) that allow the output voltage to fall within the desired limits. In these cases, therefore, it is necessary to use another method to cancel the current ripple: the cancellation leg.

With the cancellation leg active, the converter operates such that Q_{canc} conducts simultaneously with one of the switches Q_{i} ($i = 1, ..., N$), and likewise, $\overline{Q}_{\text{canc}}$ conducts in sync with $\overline{Q}_{\text{i}}$. This arrangement allows the cancellation leg to exhibit a behavior opposite to the Thevenin equivalent of a single power leg. The capacitor connected in series with the inductor blocks the DC component of the current, permitting only the AC component to flow.

4.3.1 Output current ripple cancellation

Referring to the SSIB Thevenin equivalent circuit shown in Fig. 4.5, the input voltage of the equivalent power leg is denoted as v_{p}, while that of the cancellation leg is represented by v_{c}. The equivalent power leg switches at a frequency $f_{\text{N}} = 1/T_{\text{N}} = Nf_{\text{sw}}$ and has an equivalent duty cycle defined as:

$$D_{\text{N}} = N\left(D - \frac{p-1}{N}\right) . \tag{4.5}$$

Applying Kirchhoff's Voltage Law to the Thevenin equivalent circuit, the following relationship can be established:

$$V_{\text{out}} + V_{\text{canc},0} + L\frac{di_{\text{Lcanc}}}{dt} - v_{\text{c}} = 0 , \tag{4.6}$$

$$V_{\text{out}} + L\frac{di_{\text{p}}}{dt} - v_{\text{p}} = 0 , \tag{4.7}$$

where $V_{\text{canc},0}$ denotes the initial voltage across the capacitor C_{canc}, and i_{p} represents the current flowing through the equivalent power leg. Over a time interval of $D_{\text{N}}/f_{\text{N}}$, the main voltages are defined as follows: $v_{\text{c}} = 0$, $v_{\text{p}} = V_{\text{in}}$, and $V_{\text{out}} + V_{\text{canc},0} = V_{\text{in}}(1 - D_{\text{N}})$. Since the inductor voltages remain constant during this interval, both i_{Lcanc} and i_{p} vary linearly.

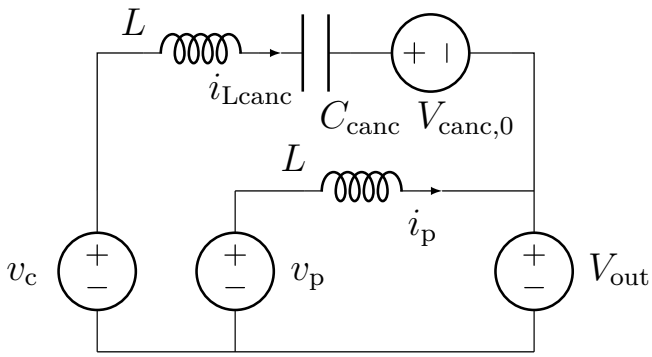

Figure 4.5: Thevenin equivalent circuit of an SSIB.

Consequently, the derivative di/dt can be expressed as $\Delta i/\Delta T$, where ΔT in this case equals $D_{\mathrm{N}}/f_{\mathrm{N}}$. From this, the residual ripple Δi_{p} and the ripple in the cancellation leg $\Delta i_{\mathrm{Lcanc}}$ can be expressed as:

$$\Delta i_{\mathrm{p}} = \frac{V_{\mathrm{in}}}{L f_{\mathrm{N}}} D_{\mathrm{N}}(1 - D_{\mathrm{N}}) \ , \tag{4.8}$$

$$\Delta i_{\mathrm{Lcanc}} = -\frac{V_{\mathrm{in}}}{L f_{\mathrm{N}}} D_{\mathrm{N}}(1 - D_{\mathrm{N}}) \ . \tag{4.9}$$

Thus, the sum of the current in the cancellation leg and the current in the other legs leads to a complete ripple cancellation of the output current; in fact, $\Delta i_{\mathrm{p}} + \Delta i_{\mathrm{Lcanc}} = 0$. Specifically, it can be seen that replacing Eq. 4.5 in Eq. 4.8 returns to Eq. 4.1. Fig. 4.6 shows the waveforms of the currents in the cancellation leg and the overall waveform of the SSIB power legs. With this topology, the current ripple is zero for any load condition.

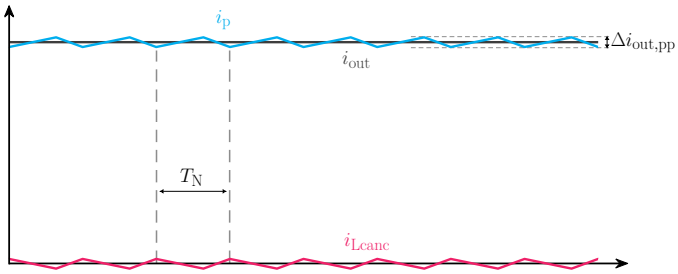

Figure 4.6: Current waveform of the SSIB.

4.3.2 Input voltage ripple considerations

Regarding the voltage ripple at the input of the converter, caused by the discontinuity of the input current, it can be evaluated starting from the current flowing through the input filter capacitor. The input current $i_{\mathrm{in}}(t)$ can be considered

as the sum of two components: a DC component i_{in} and an AC component $i_{\mathrm{in,AC}}$. For simplicity, it can be assumed that the entire AC component flows through the capacitor, thus:

$$i_{\mathrm{C}} = i_{\mathrm{in,AC}} = i_{\mathrm{in}}(t) - i_{\mathrm{in}} \ . \tag{4.10}$$

Taking into account a time interval equal to one equivalent switching period T_{N}, the input current $i_{\mathrm{in}}(t)$ corresponds to the current flowing through the inductor of the power leg, i_{p}, during the interval $D_{\mathrm{N}}T_{\mathrm{N}}$, and to the current through the inductor of the cancellation leg, i_{Lcanc}, for the remaining time $(1 - D_{\mathrm{N}})T_{\mathrm{N}}$. As previously assumed, the currents in the various legs vary linearly over time.

Therefore, the charge balance for the input filter capacitor is given by:

$$\Delta Q = \int_0^{T_{\mathrm{N}}} i_{\mathrm{C}} dt \ . \tag{4.11}$$

This can be separated into the two considered time intervals, yielding:

$$\Delta Q = \int_0^{D_{\mathrm{N}}T_{\mathrm{N}}} i_{\mathrm{C}} dt + \int_{\mathrm{D_N T_N}}^{T_{\mathrm{N}}} i_{\mathrm{C}} dt \ , \tag{4.12}$$

$$\Delta Q = \int_0^{D_{\mathrm{N}}T_{\mathrm{N}}} (i_{\mathrm{in}}(t) - i_{\mathrm{in}}) dt + \int_{\mathrm{D_N T_N}}^{T_{\mathrm{N}}} (i_{\mathrm{in}}(t) - i_{\mathrm{in}}) dt \ . \tag{4.13}$$

From the fundamental relation of the ideal buck converter, one can derive the relationship between the average input and output currents:

$$i_{\mathrm{in}} = D_{\mathrm{N}} i_{\mathrm{out}} \ . \tag{4.14}$$

Combining Eq. 4.14 with Eq. 4.13 and taking into account the considerations made earlier, the following expression is obtained:

$$\Delta Q = \int_0^{D_{\mathrm{N}}T_{\mathrm{N}}} (i_{\mathrm{p}} - D_{\mathrm{N}} i_{\mathrm{out}}) dt + \int_{\mathrm{D_N T_N}}^{T_{\mathrm{N}}} (i_{\mathrm{Lcanc}} - D_{\mathrm{N}} i_{\mathrm{out}}) dt \ . \tag{4.15}$$

From Fig. 4.6 it is possible to note that $i_{\mathrm{p}} = i_{\mathrm{out}} \pm \Delta i_{\mathrm{out,pp}}$ and $i_{\mathrm{Lcanc}} = \pm \Delta i_{\mathrm{out,pp}}$. By substituting the corresponding equations as a function of time into Eq. 4.15 and solving the integrals, the following expression is obtained:

$$\Delta Q = i_{\mathrm{out}}(1 - D_{\mathrm{N}}) D_{\mathrm{N}} T_{\mathrm{N}} \ . \tag{4.16}$$

From Eq. 4.16, the voltage ripple can be derived as follows:

$$\Delta V_{\mathrm{in,pp}} = \frac{\Delta Q}{C} \ , \tag{4.17}$$

$$\Delta V_{\mathrm{in,pp}} = \frac{i_{\mathrm{out}}}{N C f_{\mathrm{sw}}} (1 - D_{\mathrm{N}}) D_{\mathrm{N}} \ , \tag{4.18}$$

$$\Delta V_{\text{in,pp}} = \frac{i_{\text{out}}}{C f_{\text{sw}}} \left[1 - N\left(D - \frac{p-1}{N}\right)\right]\left(D - \frac{p-1}{N}\right) \ . \tag{4.19}$$

This corresponds exactly to that of the voltage ripple of the interleaved buck [156]. As with the output current, there are specific duty cycles for the input voltage that cancel out the input voltage ripple. Specifically, there are also $N+1$ points where the input voltage ripple is zero. When comparing Eq. 4.1 and Eq. 4.19, it is worth noting that the term that depends on the duty cycle is the same, so the ripple-free points are the same for both the input voltage and the output current. Based on these considerations, it can be observed that the SIB and SSIB topologies are not suitable for implementing ripple correlation control (RCC) as proposed in [157–159] to perform MPPT from a PV source. This limitation arises because, depending on operating conditions, these converters may operate at points where the input voltage ripple naturally vanishes. As a result, the control algorithm would be unable to detect or exploit the correlation between ripple variations and PV power changes, which is the fundamental principle behind RCC-based MPPT methods. Therefore, for these converter topologies, it would be more appropriate to adopt alternative MPPT techniques, such as the P&O method, which does not rely on the presence of input ripple to identify the maximum power point.

4.3.3 Hardware design consideration

In this configuration, the converter comprises N power legs for energy transfer and one additional auxiliary leg dedicated exclusively to ripple cancellation, resulting in a total of $N+1$ legs. However, the inclusion of this extra leg inevitably increases the component count, leading to higher system complexity and potentially reduced reliability. Therefore, some considerations regarding the converter design can be made in order to improve its position in comparison with other already established topologies.

From the previous discussion, it follows that the cancellation leg differs fundamentally from the power legs in both its operating frequency and current conduction profile. Specifically, the cancellation leg must operate at a switching frequency that is N times higher than that of the power legs and is designed to handle only the ripple current rather than the main load current. This significantly reduces the average current stress on its components, thereby allowing for the use of different semiconductor technologies or smaller device ratings compared to those employed in the power legs.

This flexibility opens the door to various hybrid configurations aimed at optimizing performance and cost. For example, the power legs could be implemented using IGBTs, which are generally more cost-effective for handling high current levels at moderate switching frequencies. Conversely, the cancellation leg, which requires

high-frequency operation but carries only low ripple currents, could employ Si or SiC MOSFETs. Alternatively, an even more advanced approach might utilize SiC MOSFETs in the power stage and GaN HEMTs in the cancellation leg, combining the high efficiency and fast switching of GaN devices with the robustness and maturity of SiC technology. Such hybrid implementations can lead to optimized cost-performance trade-offs, reducing overall converter losses while minimizing the cost increase associated with high-performance devices.

A crucial design consideration in this topology is the capacitor used in the cancellation leg. Since the voltage across this leg is alternating, the capacitor must be non-polarized to prevent dielectric breakdown or component failure. The use of a polarized capacitor in this position would inevitably result in rapid degradation or destruction of the component due to voltage reversal.

Finally, it is essential to account for the power leg current ripple in the thermal and electrical design of both the semiconductors and inductors. Although the output current ripple may ideally be reduced to zero through interleaving or the use of a cancellation leg, the ripple within each individual leg is never completely eliminated, except in the special cases where the duty cycle is either $D = 0$ or $D = 1$.

For this reason, the inductances of the individual legs play a crucial role in the overall design. Their values cannot be considered negligible, as they directly influence both the peak current amplitude and the magnetic flux variation within the core. If the inductance is too low, excessive ripple current may cause magnetic saturation in the inductor cores, leading to severe distortion in the current waveform, increased losses, and potential thermal runaway. Conversely, selecting inductors with excessively high inductance values would unnecessarily increase the volume, cost, and weight of the converter while also reducing its dynamic response.

Therefore, an appropriate trade-off must be achieved between electrical and magnetic design constraints. The inductors should be dimensioned to prevent core saturation under maximum load conditions while keeping thermal and conduction losses within acceptable limits. This ensures not only stable and efficient converter operation but also long-term reliability of the magnetic components under real operating conditions.

4.4 Efficiency-Enhancing Technique For Modular DC/DC Converters

4.4.1 Phase shedding

Until now, the number of legs has been considered fixed and equal to that chosen for the design. However, as already mentioned, at partial loads, in order

to improve the efficiency of the converter, only a limited number of these could be operated, thus performing the aforementioned phase shedding.

To understand why the efficiency of an interleaved converter tends to improve at partial loads when only a small number of legs are used, it is first necessary to understand how the efficiency of a generic converter can be calculated. During my PhD activities, I have mainly worked with two methods: one analytical and one based on the interpolation of experimental data.

In the analytical method, the efficiency of a power converter can be determined as the ratio between the output power P_{out} and the input power P_{in}. This approach provides a clear, component-level understanding of how losses within the converter affect its overall performance. Assuming that all power-processing legs of the converter are identical, the total losses can be divided into two main categories: those occurring in the inductors P_{L} and those associated with the switching devices P_{sw}. Hence, considering N identical legs, the total output power can be expressed as:

$$P_{\text{out}} = P_{\text{in}} - NP_{\text{L}} - P_{\text{sw}} \ . \tag{4.20}$$

The losses in the inductors are generally composed of copper losses and core losses, as expressed by:

$$P_{\text{L}} = P_{\text{Fe}} + P_{\text{Cu}} \ . \tag{4.21}$$

The losses in the magnetic core, P_{Fe}, are primarily due to hysteresis and eddy current effects. For simplicity, they can be estimated using the empirical Steinmetz equation [160]:

$$P_{\text{Fe}} = m_{\text{Fe}} k f_{\text{sw}}^{m} \hat{B}^{n} \ , \tag{4.22}$$

where $\hat{B}$ is the peak magnetic flux density in the inductor core, m_{Fe} is the mass of the magnetic core, and k, m, and n are Steinmetz coefficients that depend on the material properties of the core. Since $\hat{B}$ is proportional to the peak current flowing through the inductor, once the inductor geometry and switching frequency are fixed, P_{Fe} can be scaled directly as a function of the current amplitude. This approximation simplifies the analysis without significantly compromising accuracy for most practical designs.

The copper losses, on the other hand, result from the Joule effect in the winding conductors and are expressed as:

$$P_{\text{Cu}} = i_{\text{L,rms}}^{2} R_{\text{L}} \ , \tag{4.23}$$

where $i_{\mathrm{L,rms}}$ is the RMS current through the inductor and R_{L} is the equivalent series resistance of its winding. These losses increase quadratically with current, making them particularly relevant at high load conditions.

The losses in the switching devices, P_{sw}, can be further decomposed into three components: conduction losses P_{Ω}, commutation (or switching) losses P_{com}, and auxiliary losses P_{aux}, as defined by:

$$P_{\mathrm{sw}} = P_{\Omega} + P_{\mathrm{com}} + P_{\mathrm{aux}} \ . \tag{4.24}$$

The auxiliary power P_{aux} corresponds to the energy required by the gate driver circuits of the switches. It can be reasonably approximated as constant and independent of the current flowing through the device. Therefore, for N converter legs (each with two switches), the total auxiliary power consumption becomes:

$$P_{\mathrm{aux}} = 2P_{\mathrm{aux}}N \ , \tag{4.25}$$

where P_{aux} is the driver power consumption per individual switch.

Within each leg, the lower switch conducts for a fraction of the switching period equal to the duty cycle D, while for the remaining portion of the cycle $(1-D)$, the corresponding upper diode conducts. The total conduction losses can therefore be written as:

$$P_{\Omega} = i_{\mathrm{L,rms}}^2 R_{\mathrm{sw,on}} D + (i_{\mathrm{L,rms}} V_{\mathrm{d}} + i_{\mathrm{L,rms}}^2 R_{\mathrm{d}})(1 - D) \ , \tag{4.26}$$

where $R_{\mathrm{sw,on}}$ is the on-state resistance of the switch, V_{d} is the diode forward voltage drop, and R_{d} is the diode on-state resistance. This formulation highlights how both the duty cycle and current levels influence the conduction losses of the converter.

Finally, commutation losses P_{com} are mainly associated with the switching transitions (turn-on and turn-off events) of the semiconductor devices. These can be estimated from the manufacturer's datasheet by considering the energy dissipated during each switching event and the switching frequency. Although they typically represent a smaller fraction of total losses at low switching frequencies, they become increasingly significant as the frequency rises.

Indeed, the energy values E_{on} and E_{off} provided in semiconductor datasheets are typically measured under specific test conditions, corresponding to a reference current i_{rate} and voltage. These values generally scale linearly with the actual current flowing through the switch, while the voltage dependency is often less significant and can be neglected in a first-order approximation. Thus, by assuming a linear dependence on the current and keeping the voltage constant, the commutation losses can be estimated by rescaling the reference energy values according to the real operating current. Consequently, the total switching losses can be expressed as:

$$P_{\text{com}} = f_{\text{sw}}(E_{\text{on}} + E_{\text{off}})\frac{i_{\text{L,rms}}}{i_{\text{rate}}} \ , \tag{4.27}$$

where E_{on} and E_{off} represent the energy dissipated during turn-on and turn-off transitions, respectively. This simplified formulation allows for a reasonably accurate estimation of commutation losses, provided that the converter operates near the test conditions specified in the datasheet.

The analytical method described so far offers a valuable tool for predicting the converter's efficiency already at the design stage, as it directly links the electrical and magnetic parameters of the components to overall losses. However, this approach requires detailed knowledge of every relevant construction parameter, including parasitic elements and thermal characteristics. Moreover, the greater the number of simplifications or assumptions made (such as linear dependencies or neglecting temperature effects), the greater the deviation between the estimated and actual efficiency values. Hence, while highly informative during preliminary design and optimization, this method should ideally be complemented by experimental validation.

An alternative and often more practical approach to estimating converter efficiency relies on experimental measurements. In this case, the efficiency curve is derived from measured input and output power data under different load conditions, and the results are interpolated to obtain a continuous efficiency profile. This empirical technique was first formalized in [147] and is particularly advantageous for evaluating modular or interleaved converters, where direct analytical modeling becomes cumbersome.

The underlying concept is that converter losses can be decomposed into three principal components: a constant term (associated with fixed power consumption, such as driver circuits and control electronics), a term of linear proportionality (representing switching losses), and a term of quadratic proportionality (representing conduction or ohmic losses). Based on this reasoning, the efficiency of a single-leg converter can be expressed as:

$$\eta_{\text{conv}} = \frac{1}{1 + \frac{k_0}{P_{\text{out}}} + k_1 + k_2 P_{\text{out}}} \ , \tag{4.28}$$

where k_0 is the coefficient that quantifies the fixed losses, k_1 represents the linear component, and k_2 accounts for conduction losses, which scale quadratically with the current or power.

When losses are very small compared to the overall power of the converter, i.e., when the converter efficiency is very high, it is possible to simplify Eq. 4.28 to:

$$\eta_{\text{conv}} \approx 1 - \left(\frac{k_0}{P_{\text{out}}} + k_1 + k_2 P_{\text{out}}\right) \ . \tag{4.29}$$

When multiple converter legs are connected in parallel, as in interleaved architectures, the loss distribution changes. Specifically, since each leg processes only a fraction of the total current, the equivalent conduction resistance, and thus the losses associated with the quadratic term, decrease. However, the number of driver circuits increases, leading to higher fixed losses. Accordingly, the efficiency expression for an N-leg interleaved converter becomes:

$$\eta_{\text{conv}} \approx 1 - \left(\frac{N k_0}{P_{\text{out}}} + k_1 + \frac{k_2 P_{\text{out}}}{N} \right) . \tag{4.30}$$

This model provides a highly practical and versatile tool for estimating efficiency, even in the absence of detailed component-level data. By performing a limited set of experimental measurements on a converter with a given number of legs, one can extract the coefficients k_0, k_1, and k_2 through curve fitting. Once these coefficients are determined, it becomes possible to extrapolate the efficiency performance for converters with different configurations or power ratings by means of a second-order polynomial interpolation. This method thus offers an effective bridge between empirical validation and theoretical modeling, enabling both accurate efficiency prediction and scalable converter design.

It is therefore clear that reducing the number of active legs can lead to an improvement in converter efficiency, particularly under partial-load conditions. This is because, as previously discussed, fewer active legs reduce the number of gate driver circuits and associated fixed losses, which become proportionally more significant at low output powers.

4.4.2 Operation in boundary condition mode

However, there exists another effective strategy to enhance converter efficiency: operating in BCM. In this mode, the converter is controlled so that the switches commutate when the current flowing through them reaches zero, effectively eliminating switching losses in ideal conditions.

Unlike what has been considered up to now, where the switching frequency is constant and independent of load conditions, in BCM the switching frequency dynamically adapts to the load current. This variable-frequency operation allows each switching transition to occur at zero current, minimizing the energy dissipated during turn-on and turn-off events. The switching frequency in BCM can be expressed as a function of the load current, input voltage, and duty cycle, as follows:

$$f_{\text{sw}} = \frac{N V_{\text{in}}}{2 i_{\text{out}} L} (1 - D) D . \tag{4.31}$$

From (4.31), it can be observed that the switching frequency is inversely proportional to the load current: as the output current increases, the switching frequency

decreases, and vice versa. This relationship ensures that the inductor current reaches zero at the end of each switching period, satisfying the boundary condition that defines BCM operation.

While BCM operation theoretically eliminates switching losses, it introduces several practical design considerations. At high load currents, the corresponding reduction in switching frequency increases the current ripple and the RMS current in the inductor and switches. This, in turn, leads to higher conduction losses and can increase thermal stress on the components. Conversely, at low load currents, the switching frequency tends to rise significantly, potentially exceeding the safe operating limits of the semiconductor devices or the control circuitry. Therefore, in practical implementations, the switching frequency must be constrained within defined upper and lower limits to ensure reliable operation.

In summary, operating a converter in BCM provides a valuable trade-off between minimizing switching losses and maintaining acceptable conduction losses. However, its effectiveness depends on careful design of both the magnetic components and the control strategy, ensuring that the converter operates efficiently across the entire load range without exceeding component limitations.

4.5 Proposed Cancellation Methodology

The modulation technique proposed in this thesis aims to combine the advantages of both the cancellation leg and ripple-free modulation techniques. The considered topology is the SSIB, with the number and type of legs varying according to the power handled by the converter. It is assumed that the input voltage V_{in} may fluctuate within a predefined range established as a design parameter, since on the input, the presence of PV is assumed. Under normal operating conditions, the converter functions as an interleaved buck, with the cancellation leg deactivated.

The system architecture considered assumes the presence of a DC bus between the PV source and the electrolyser. If this DC bus is not present and the PV array is directly connected to the stack through the SSIB converter, one of the two components would inevitably operate inefficiently. In particular, the electrolyser stack would be exposed to excessively fast power fluctuations, or, conversely, the PV system would be unable to perform MPPT when the hydrogen storage cannot accommodate additional hydrogen production. An auxiliary energy storage system, such as a battery bank or a grid connection, could be integrated into the DC bus to ensure continuous hydrogen generation; however, these additional components are not considered in the present discussion.

It is therefore assumed that a higher-level energy management control operates above the converter's modulation layer, managing the overall energy flow within the entire P2H system. A generic schematic of a possible control architecture for the

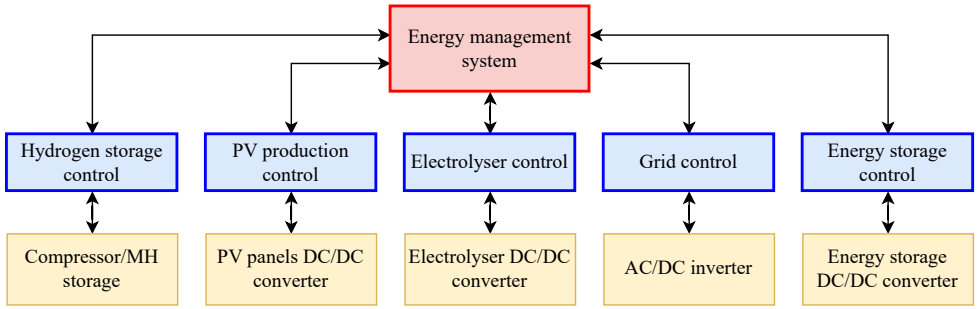

Figure 4.7: Possible control diagram for the plant and all its possible subsystems.

entire hydrogen production plant, together with the control of the various specific subsystems, is shown in Fig. 4.7. The focus of this thesis, however, is limited exclusively to the control subsystem associated with the electrolyser. The energy management system is responsible, in particular, for regulating the storage system, which in turn dictates the hydrogen production rate. In this thesis, the worst-case scenario is considered (namely, the use of MH storage), whose hydrogen adsorption characteristic is nonlinear with respect to pressure.

When the hydrogen storage system allows for maximum input flow, the electrolyser can be controlled to operate at any desired point along its characteristic curve, offering complete flexibility in prioritizing either stack efficiency, hydrogen production rate, or adaptation to PV generation. Conversely, when the storage flow rate is constrained, the operating point of the electrolyser becomes correspondingly limited. In systems equipped with a DC bus, however, the PV panels can continue performing MPPT independently, as any surplus energy can be directed to auxiliary storage systems or other loads.

Once the electrolyser's production threshold has been defined, the corresponding required output power P_{out} can be determined. Based on this value, the appropriate number of converter legs N is selected, and phase shedding is applied to maximise efficiency. Using the power characteristics and the stack polarisation curve, the voltage that must be applied to the electrolyser to achieve the desired power absorption can then be calculated.

Knowing the number of active legs N and the output voltage V_{out}, the duty cycle required to achieve ripple-free operation can be computed using Eq. 4.4. If a duty cycle $D \neq 0$ exists, it is verified through the conventional input-output relationship of the buck converter that the resulting output voltage corresponds to the desired value for the given input voltage.

If this condition is not satisfied, two alternative actions are possible: adjust the DC bus voltage, thereby modifying V_{in} to obtain the desired V_{out} while maintaining the previously calculated duty cycle; or activate the cancellation leg, recalculating the duty cycle so that, for the given input voltage, the desired output voltage is

achieved.

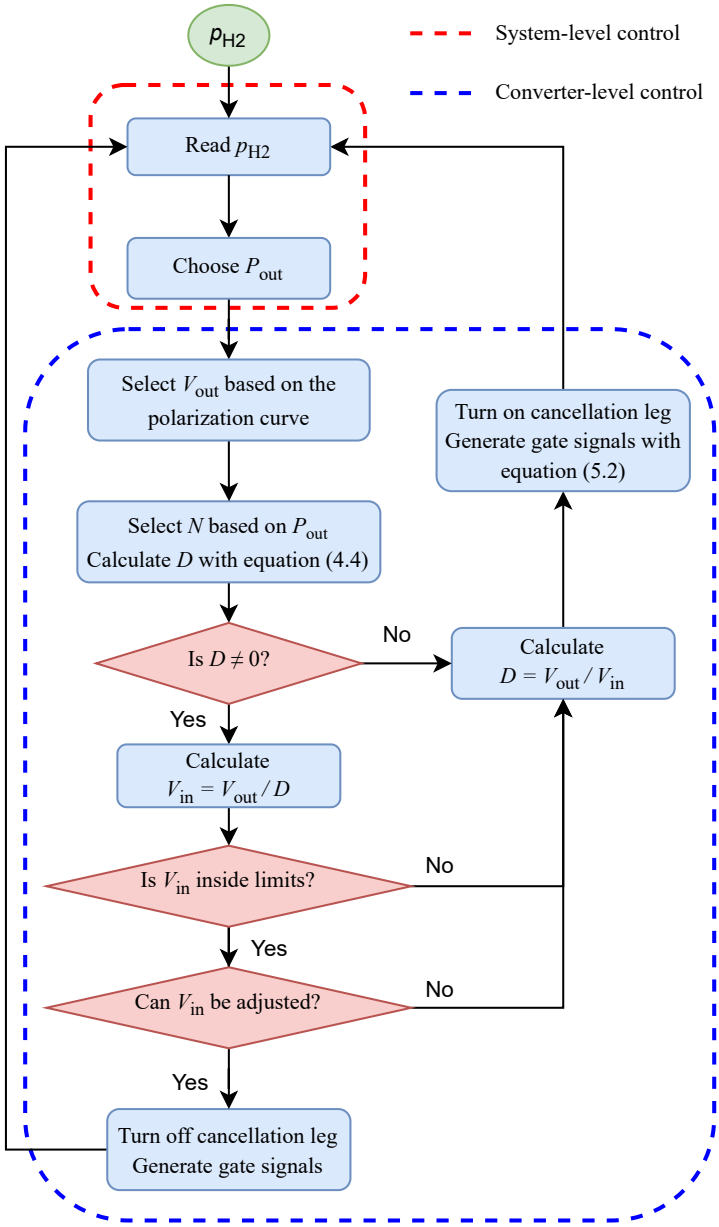

Figure 4.8: Generic block diagram of the proposed logic.

The first solution depends on the external energy management system, which must act on other converters to vary the DC bus voltage. In contrast, in the second case, the duty cycle is recalculated so that, for the given input voltage, the output voltage corresponds to the desired one. This approach minimises the number of components conducting in each cycle while ensuring the primary requirement of maintaining a ripple-free output current. A schematic representation of the described

control logic is shown in Fig. 4.8, in which the different control levels have also been highlighted, together with the specific tasks and responsibilities that each of them should address. This allocation of responsibilities is designed to clearly separate the plant-level energy management system from the individual electrolyser converter, thereby decoupling the electrolyser converter from the specific context in which it is integrated. As a result, the only input parameter required by the control system of the electrolyser converter is the power it is required to absorb. In this way, regardless of the particular application or system configuration in which the converter is deployed, the electrolyser stack can always be supplied under ripple-free operating conditions.

4.5.1 Leg number regulation and transient handling

Sudden variation in the number of active legs, the carrier phase-shift angle, or the C_{canc} voltage step leads to electric transients. When one of these events occurs, both the power branches and the cancellation leg temporarily experience an incorrect duty cycle value, which may induce a second-order underdamped oscillation and result in potentially dangerous current peaks.

To address this issue, whenever the number of active legs changes (either through activation or deactivation), all switches are turned off, allowing the inductor currents to decay to zero. Immediately afterwards, the correct number of legs is sequentially reactivated to establish the new current distribution and carrier phase shift according to the updated configuration, virtually eliminating second-order transient effects.

During the brief interval in which the converter is shut down, it is possible to combine the action of another fundamental component of PEM cells' system: the already mentioned SCU. The SCU periodically short-circuits the electrolyser for approximately 100 milliseconds, aiding in the humidification of the proton exchange membranes [161–163]. The time required for leg reconfiguration is significantly shorter than the SCU operating period. In fact, leg reconfiguration can be synchronised to occur simultaneously with the SCU action.

The system can therefore encounter three types of events:

1. **Cancellation capacitor voltage regulation:** To effectively cancel residual ripple, it is necessary that the capacitor C_{canc} experiences a voltage of $V_{\text{in}}(1 - D_{\text{N}}) - V_{\text{out}}$. It should be noted that D_{N} depends on N, as defined in Eq. 4.5. During steady-state operation, when no abrupt voltage change occurs, this voltage is naturally regulated by the cancellation leg. However, whenever the number of active legs is modified, the voltage changes abruptly, triggering transients. To mitigate this, the voltage should be gradually adjusted by acting on the cancellation leg duty cycle while the power legs remain active. This

ensures that the cancellation capacitor reaches the correct voltage value before the switch shutdown (i.e., event number 2). During this adjustment period, the ripple-free characteristic is temporarily lost, but harmful transients are prevented.

2. **Switch shutdown:** To initiate leg reconfiguration, all gate signals are set to zero, turning off the switches. Immediately afterwards, the inductor currents begin to decrease (flowing through the antiparallel diodes of the switches) until they reach zero. So the voltage on the x-th leg inductor, from Kirchhoff's Voltage Law, will be $V_{\mathrm{Lx}} = -V_{\mathrm{out}}$. From the fundamental equation of the inductor, we can therefore deduce that:

$$\frac{di_{\mathrm{Lx}}}{dt} = -\frac{V_{\mathrm{out}}}{L} \ . \tag{4.32}$$

As previously mentioned, it is considered the variation of the linear current over time. In the worst-case scenario (namely when the inductor current is at its upper peak), the system requires a resetting time approximately equal to:

$$t_{\mathrm{res}} = \frac{L}{V_{\mathrm{out}}} \left(i_{\mathrm{Lx}} + \frac{V_{\mathrm{in}}}{2Lf_{\mathrm{sw}}}(1-D)D \right) \ , \tag{4.33}$$

where i_{Lx} is the average current of the x-th leg.

It should also be noted that when both cancellation leg switches are turned off, the voltage across C_{canc} remains constant at the value set during event 1.

3. **Sequential switch turn-on:** To re-establish normal current flow with the new leg configuration, each leg's upper switch is sequentially turned on with a time delay of T_{sw}/N (corresponding to the interleaving phase shift). The switches remain in this configuration for a duration of $(I_{\mathrm{Lx}}L)/V_{\mathrm{in}}(1-D)$, sufficient to reach the steady-state average current. Once this time has elapsed, regular PWM operation resumes. The cancellation leg is activated once the last active leg reaches its steady-state value. In the worst-case scenario, ripple-free operation is restored in approximately $(I_{\mathrm{Lx}}L)/V_{\mathrm{in}}(1-D) + (N-1)/(f_{\mathrm{sw}}N)$.

In summary, the transition from $N = N'$ to $N = N''$ can be achieved through the following procedure: first, regulate the voltage of the cancellation capacitor to $V_{\mathrm{canc},0}(N'')$ (event 1); second, shut down the N' active legs and the cancellation leg (event 2); finally, sequentially turn on the N'' new legs (event 3).

5

Results and Discussion

The previous Chapters covered all the theory relating to PV hydrogen production systems, and in particular the type of converter considered. This Chapter, on the other hand, presents a case study to support the proposals made in this thesis and the experimental results of the tests conducted in the laboratory in recent years.

5.1 Simulation Results

In this section, a numerical example is presented to validate the operation of the proposed converter architecture and its corresponding control strategy. The case study focuses on the PEM electrolyser available in our laboratory, which serves as a representative system for small-scale hydrogen production powered by photovoltaic sources. The electrolyser has a nominal power output of 2.5 kW and can reach a maximum power output of 3 kW under full-load conditions.

The polarization curve and the corresponding power characteristic used for the analysis are reported in Fig. 5.1. These curves are obtained from experimental measurements carried out during steady-state operation of the electrolyser. As a result, the regions associated with activation losses (typically observed at very low current densities) and diffusion losses (which occur when the current density exceeds the rated operating limit) are not included in the plots, as both represent undesirable and potentially damaging operating conditions for the stack.

This thesis does not address the optimal sizing of the overall system; therefore, parameters such as the number of PV panels, their specific type, or their arrangement into strings will not be considered in detail. A reasonable and realistic assumption, consistent with current commercial PV system architectures, is that all panels are connected to a common DC bus through individual power optimizers. Each panel is thus equipped with its own DC/DC converter, responsible for performing MPPT locally. The voltage of the common DC bus will consequently vary depending on external conditions, such as partial shading or mismatch among panels.

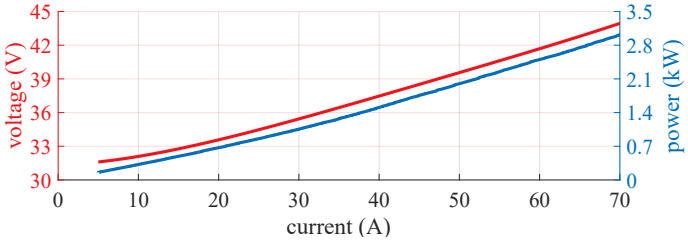

Figure 5.1: Polarization curve (in red) and power curve (in blue) of the considered electrolyser.

In grid-connected systems, the DC bus voltage is typically regulated by an inverter, which maintains it within specific limits, usually in the range of a few hundred volts. In this case study, however, the presence of the inverter connected to the DC bus in parallel to the stack is not considered in the following simulations. Nevertheless, since the DC bus voltage represents a degree of freedom in the system, it can be selected so that it remains within the standard voltage range commonly used for PV inverters.

Considering the size of the electrolyser under study (3 kW), it is assumed that the system is connected to a low-voltage single-phase grid. Accordingly, the DC bus voltage range is set between 280 and 420 V, corresponding to a nominal voltage of approximately 350 V $\pm$ 20%. This choice ensures that, if the system were to be integrated with the grid, the DC bus voltage would be compatible with typical PV inverter operation. Moreover, the upper limit of 420 V allows the use of 800 V rated semiconductor switches at a utilization factor of about 40–50%, providing a significant safety margin for both voltage stress and thermal considerations.

It should be noted that these limits are conservative, as many commercial PV inverters can tolerate wider voltage ranges. For example, the Huawei SUN2000-3KTL-M1 inverter supports an operating voltage range of 140 to 980 V, offering greater flexibility in system design and operation.

Once the voltage limits have been defined, it is possible to determine the minimum number of legs required for ripple-free operation using Eq. 4.3. In this specific case, the minimum number of legs is found to be 9, leading to the selection of a converter configuration consisting of 9 power legs and one cancellation leg.

Employing nine power legs offers several advantages. Firstly, it enables the implementation of phase shedding, which can be exploited to improve the converter's efficiency under partial load conditions. Secondly, this configuration enhances the system's fault tolerance, allowing continued operation even in the event of power derating caused by the failure of one or more legs. Moreover, choosing a number of legs that is a multiple of three provides an additional benefit in terms of modularity, as the same hardware modules could also be employed in three-phase inverter applications, thereby increasing design flexibility and reducing overall system costs.

The use of 9 legs in this configuration implies that each leg is required to carry a maximum mean current of approximately 8 A, which allows for the use of smaller and more cost-effective components. The peak current flowing through the individual switch will be higher and will depend on the design of the inductor.

In this regard, for the inductor design, it is assumed that the peak-to-peak current ripple in each inductor, $\Delta i_{\mathrm{L,pp}}$, is limited to 20% of the maximum average current under the worst-case operating condition, i.e., when $D = 0.5$, as discussed in the previous Chapter and illustrated in Fig. 4.2b. This represents a conservative design choice, ensuring that, under partial-load conditions, the current ripple remains lower for the same inductance value. The only case in which higher peak currents could occur is if the converter is operated in BCM mode, thereby reducing the frequency.

About the switching frequency, a maximum value of $f_{\mathrm{sw}} = 10$ kHz is considered, and the design of the inductors is carried out based on this value. For the efficiency evaluation in BCM operation, it is assumed that the switching frequency could vary dynamically between a minimum of 1 kHz and the aforementioned maximum of 10 kHz. In this case, soft-switching is achieved without the use of external snubber circuits, relying solely on the adopted modulation technique. More specifically, the switching frequency f_{sw} is dynamically adjusted so that the minimum value of the leg current coincides with zero. Moreover, setting the upper frequency limit to 10 kHz guarantees that, even in the worst case, the switching frequency of the cancellation leg remains below 150 kHz, which complies with standard limits imposed by electromagnetic compatibility regulations [164].

Despite the considerations made in the previous Chapter regarding the selection of different semiconductor technologies for each leg, for the sake of simplicity, in this analysis a single switch model is assumed for all converter legs. Specifically, the Fairchild FCPF400N80Z MOSFET is selected as the reference device.

The efficiency is evaluated using the analytical approaches previously discussed. Three operating cases are considered: the SIB topology with phase shedding, the SSIB topology with phase shedding, and the SSIB topology combining phase shedding with BCM operation. For the efficiency calculation, only the losses in inductors, switches, diodes, and auxiliary circuits are included, while capacitor losses are neglected.

The parameters of the selected MOSFET are taken from the manufacturer's datasheet, considering the worst-case operating condition corresponding to a junction temperature of 100 °C, to obtain conservative estimates. The losses in the inductor core, P_{Fe}, are computed by assuming a generic ferrite material, with parameters derived from [160]. For the winding resistance and the ferrite core mass, the reference model considered is the TDK B82746S6702A040. All relevant parameters used for

the efficiency calculations are summarized in Tab. 5.1.

Table 5.1: Efficiency Calculation Parameters

Parameter	**Value**	**Unit**
Leg inductance, L	6.5	mH
Inductor resistance, R_{L}	18	mΩ
Ferrite mass, m_{Fe}	175	g
Steinmetz mass coefficient, k	$1.983 \cdot 10^{-3}$	
Steinmetz frequency coefficient, m	1.36	
Steinmetz magnetic coefficient, n	2.86	
Switch resistance, R_{sw}	34	mΩ
Diode resistance, R_{d}	109	mΩ
Diode forward voltage, V_{d}	1.2	V
Turn on losses, E_{on}	$23.6 \cdot 10^{-6}$	J
Turn off losses, E_{off}	$39.5 \cdot 10^{-6}$	J
Auxiliaries losses, P_{aux}	1	W

The results of the analytical efficiency calculation are presented in Fig. 5.2, while Fig. 5.3 provides a direct comparison among the three analysed cases. As can be observed, the SIB topology exhibits slightly higher efficiency than the SSIB, primarily due to its lower component count. It should also be noted that, in this analysis, capacitor losses have been neglected, and the SSIB includes an additional capacitor, which would further increase its total losses in a more detailed evaluation.

In contrast, the BCM configuration consistently achieves higher efficiency across the operating range. This indicates that the limitation lies not in the intrinsic performance of the BCM itself, but rather in the choice of switching frequency used for the other two configurations. Specifically, the adopted frequency saturation mechanism imposes a lower frequency limit at high load conditions, when the current increases. Since, in the selected switch model, switching losses represent a significant portion of the total losses, this constraint directly impacts overall efficiency.

Nevertheless, as the purpose of this example is purely qualitative, the switching frequency values reported in Tab. 5.1 are retained. A further reduction of the switching frequency would require redesigning the inductors and selecting alternative components, which would in turn alter the efficiency estimation. Such an optimisation process lies beyond the scope of this thesis.

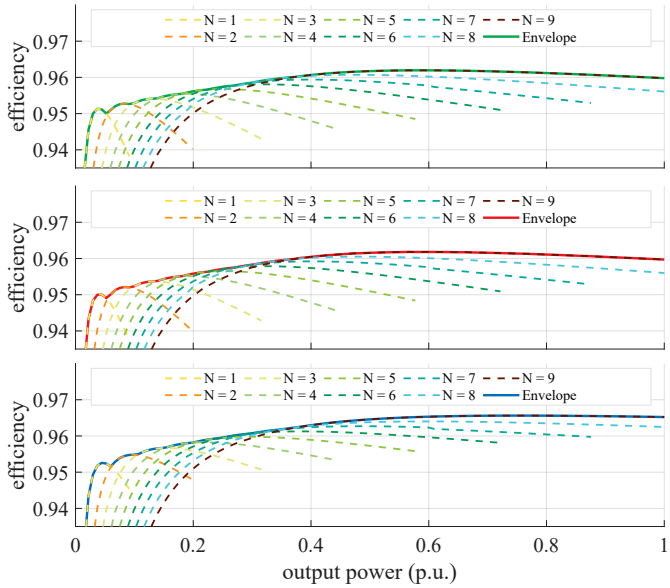

Figure 5.2: Efficiency curves varying the number of legs from $N = 1$ to $N = 12$ and their upper envelope, considering on top the SIB, in the middle the SSIB, and at the bottom the SSIB with BCM.

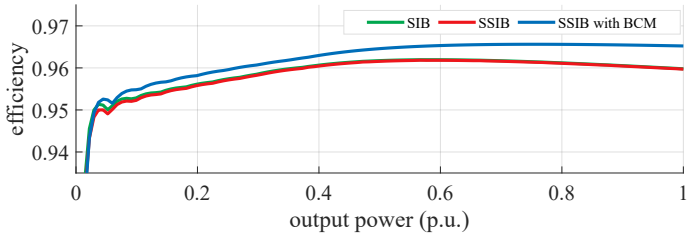

Figure 5.3: Comparison between phase shedding and phase shedding with BCM.

To enable a fair comparison among the three configurations, the four-point efficiency $\eta_{4\text{point}}$ is introduced, defined as:

$$\eta_{4\text{point}} = \frac{1}{4}(\eta_{25\%} + \eta_{50\%} + \eta_{75\%} + \eta_{100\%}) \ , \tag{5.1}$$

where $\eta_{25\%}$, $\eta_{50\%}$, $\eta_{75\%}$, and $\eta_{100\%}$ correspond to the converter efficiency at 25%, 50%, 75%, and 100% of the nominal load, respectively.

The calculated four-point efficiencies for the SIB, SSIB, and SSIB operating in BCM mode are 96%, 95.9%, and 96.3%, respectively. These results indicate that deactivating the cancellation leg is beneficial when current ripple elimination is already achieved through duty cycle modulation, as it allows for a slight improvement in overall efficiency and a reduction in component stress.

Furthermore, the BCM case is not considered in the subsequent analysis, as its improved performance is primarily the result of the lower switching frequency

imposed. Another reason for this exclusion concerns converter control: dynamically varying both the switching frequency and the number or type of active legs introduces instability when the system operates in open loop, as in the present case. For these reasons, operation in BCM will not be examined further in the simulations, although it may represent an interesting subject for future research.

Before conducting the experimental tests, the phase-shedding control logic of the SSIB is simulated in PLECS, focusing exclusively on the electrolyser and its associated converter. In this simulation, the source is modeled as a controlled voltage source, while a ramp-shaped power demand is applied to the electrolyser to emulate a request from the plant's energy management system. The electrolyser is modelled using a lookup table containing the polarisation curve data from Fig. 5.1. The power ramp duration is 5 s, starting from 0 and reaching maximum power. The ramp duration is chosen arbitrarily and is not a standard operating condition for an electrolyser. Load variation requests of this type could only occur at start-up, when the system needs to be pressurised.

To implement the algorithm proposed in Fig. 4.8 and select the number of active power legs, it can be performed either through a block of C code or by implementing state machines in which the analytically derived efficiency curves are embedded. If experimental data are available, they can be integrated in the same way to refine the decision logic. The first approach, based on C code, offers greater flexibility and adaptability to various operating conditions but requires more complex implementation. Conversely, the state machine approach is simpler to realize and easier to maintain, though it is inherently less flexible and may require reconfiguration if system parameters change.

Since the number of active legs and their corresponding phase shifts must vary dynamically according to the power demand, it is essential that the carrier signals adapt in real time. For this reason, the carriers for the power legs are generated by mathematically synthesizing the triangular waveforms rather than using predefined PLECS blocks. This approach is chosen because PLECS does not natively provide a block capable of dynamically adjusting the phase shift between multiple carriers, a crucial requirement to maintain the correct interleaving and ensure ripple-free operation under varying load conditions.

A key requirement for the correct operation of the SSIB is maintaining carrier synchronism, since the switching frequency of the cancellation leg depends on the number of active power legs N. If separate carriers are used for the cancellation leg and the power legs, synchronism may be lost during the activation or deactivation of additional legs. As the number of active power legs varies, the carrier frequency of the cancellation leg changes accordingly, potentially introducing an undesired phase shift relative to the other carriers. This loss of phase alignment compromises the converter's ability to effectively cancel current ripple.

To prevent this issue, the gate signal of the cancellation leg $s_{\text{canc}}(t)$ is generated according to the following relation:

$$s_{\text{canc}}(t) = \sum_{\text{i}=1}^{N} s_{\text{i}}(t) - \text{floor}(ND) - N_{\text{off}} \ , \tag{5.2}$$

where $s_{\text{i}}(t)$ represents the gate signal of the i-th power leg, and N_{off} denotes the number of inactive converter legs.

Fig. 5.4 shows the waveforms of the currents in the converter when $N = 4$. At this operating point, there are no duty cycles that allow ripple-free operation, so the use of the cancellation leg is essential. As demonstrated in the previous Chapter and as can be seen in Fig. 5.4b, the current on the load is ideal and ripple-free.

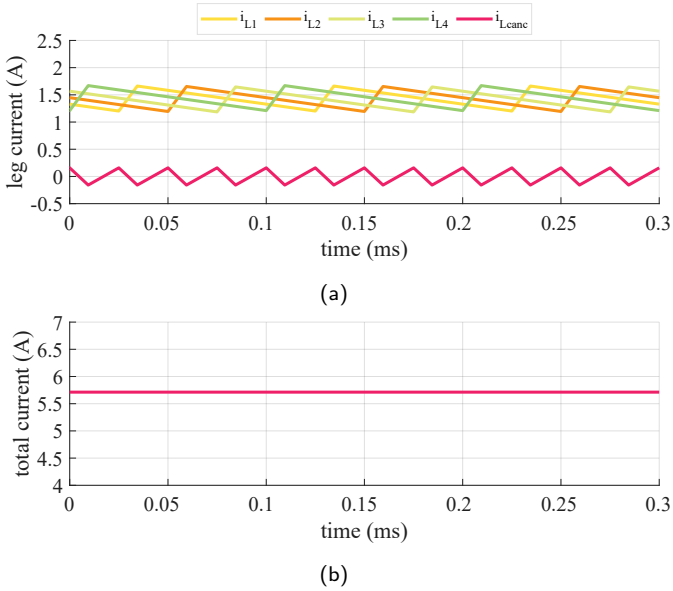

Figure 5.4: Current waveforms in case $N = 4$ and the cancellation leg working: (a) currents on the inductors, (b) current on the load.

Fig. 5.5 shows the current trends in the power legs during the power ramp. As can be seen, as the load varies, phase shedding of the unnecessary legs occurs. It should be noted that in Fig. 5.5, no transient control technique has been implemented, so that each time the number of legs changes, with the insertion of a new one, a transient occurs which, as mentioned in the previous Chapter, leads to unwanted current peaks.

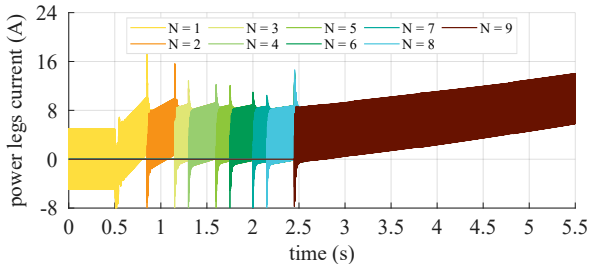

Figure 5.5: Power legs current trends.

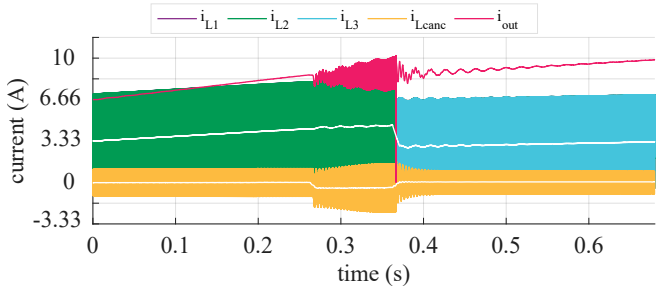

(a)

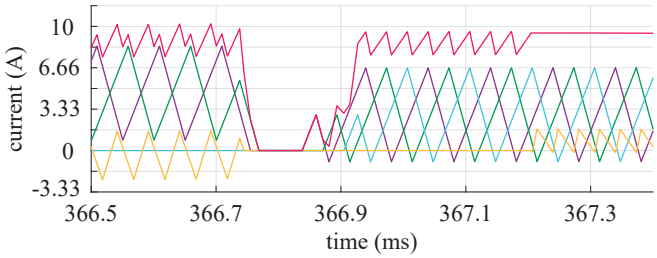

(b)

Figure 5.6: Power legs, cancellation, and input currents under active leg number rearrangement from $N' = 2$ to $N'' = 3$: (a) white lines are the moving average of power legs and cancellation currents, (b) a detailed view of the currents during the leg transition.

To validate the results related to ripple-free operation, phase shedding, and transient handling, Fig. 5.6 reports the time-domain waveforms of the power-leg currents, the cancellation-leg current, and the total input current, considering a transition in the number of active legs from $N' = 2$ to $N'' = 3$. As shown in the Fig. 5.6a, the electrolyser current i_{out} is initially ripple-free thanks to the action of the cancellation leg, whose compensating behaviour is visible in the waveform of i_{Lcanc}.

At $t = 268$ ms, the voltage of the cancellation capacitor C_{canc} begins its controlled adjustment in anticipation of the leg-number increase (event 1 in Subsection 4.5.1). During this interval, as expected, i_{out} temporarily loses its

ripple-free condition. Moreover, the cancellation current i_{Lcanc} exhibits a non-zero moving average, indicating an exchange of energy with the cancellation capacitor.

When the capacitor voltage regulation is completed (at $t = 366.7$ ms), the system undergoes events 2 and 3 in rapid succession. As highlighted in Fig. 5.6b, all currents are forced to zero in approximately 50 μs. After roughly 70 μs, the power legs are reactivated sequentially, and the steady-state current is restored in less than 100 μs without any noticeable transient. At $t = 367.2$ ms, the cancellation leg is enabled again, reinstating ripple-free operation of i_{out}.

It is worth noting that the system remains in a shutdown state for less than 1 ms, a duration significantly shorter than the typical times associated with SCU operation [163]. The same sequence of events can be replicated for any pair of operating points N' and N''.

5.2 Experimental Results

To evaluate the impact of the cancellation leg on current ripple, as well as its effectiveness when the converter already operates under ripple-free duty conditions, a series of experimental tests were carried out. In these tests, the converter is implemented with seven power legs and a single dedicated cancellation leg.

The laboratory setup is divided into two main sections: the power section, which includes the converter under test, and the control and acquisition section. A photograph of the complete setup is shown in Fig. 5.7.

The power section consists of a TDK-Lambda GEN 750W/1500W series power supply, two capacitors connected in parallel to form the input filter, and four PCBs connected in parallel that constitute the converter under test. Each PCB integrates an IGBT-based H-bridge along with its corresponding gate driver circuitry. The setup also includes the inductors associated with the power legs and two capacitors connected in series to realise the capacitance of the cancellation leg.

Since the experiments were conducted in multiple sessions with different objectives, the load configuration varied accordingly. To verify the basic operation of the converter and analyse current waveforms, two resistors connected in series were used. For efficiency analysis and accurate converter characterisation, an electronic load ITECH IT6600C was employed, allowing control of the absorbed power at a fixed applied voltage.

The component parameters and operating quantities are summarised in Tab. 5.2.

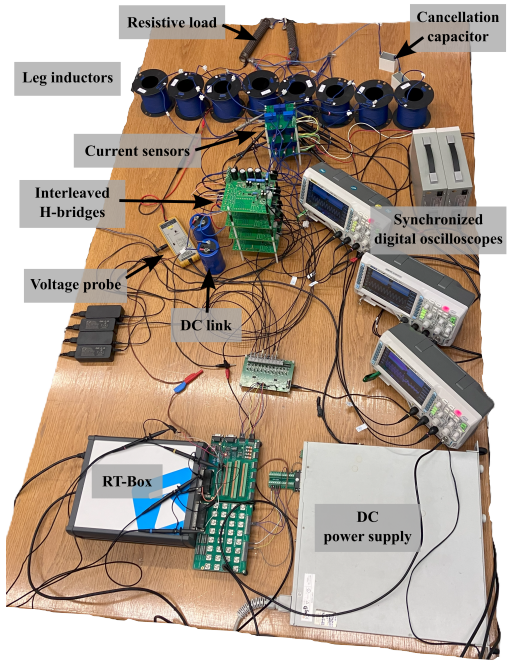

Figure 5.7: View of the whole experimental setup.

Table 5.2: Experimental System Parameters

Parameter	**Components Count**	**Value**	**Unit**
DC link capacitance, C_{DC}	2	1	mF
Leg inductance,L_{i}	8	1.73	mH
Leg resistance,R_{i}	8	0.73	Ω
Cancellation capacitance, C_{canc}	2	100	μF
Load resistor, R_{load}	2	10	Ω
Input voltage, V_{in}	ND	70	V
Switching frequency, f_{sw}	ND	1	kHz

The control and acquisition section includes three RIGOL DS1054Z oscilloscopes for voltage and current waveform monitoring, eight LEM LA 55-P current sensors, a Pico Technology TA041 voltage probe, the RT Box-1 real-time control platform for converter operation, a ZES Zimmer LMG671 precision wattmeter, and a personal computer for supervision and data processing.

To implement phase shedding, it is essential to directly control the gate signals of the individual switches; otherwise, a leg would remain permanently active or inactive, preventing proper deactivation. With this experimental setup, dynamic phase shedding could not be implemented because the single leg is controlled by a

single signal, which is divided between the gates of the individual switches by means of auxiliary circuits on the single board, making it impossible to switch off both switches. The tests are therefore conducted for three fixed configurations with 7, 5, and 3 power legs. For each configuration, three common duty cycles are tested: $D = 1/N$, $D = 1/2$, and $D = (N - 0.5)/N$. The first condition corresponds to the ripple-free operating point for all configurations, the second represents an intermediate condition common to all three configurations, and the third corresponds to the operating point with the maximum ripple amplitude for every respective configuration.

The generation of the carrier and modulation signals is performed within the PLECS environment, while the gate signals are generated by the RT-Box, which transmits the corresponding digital signals to the converter boards. To emphasise the effect of the cancellation leg, the maximum switching frequency of the power legs is set to 1 kHz. This choice intentionally increases the current ripple for a given inductance, thereby highlighting the ripple-cancellation capability of the additional leg.

For each test, the converter operation is evaluated both with and without the activation of the cancellation leg. Data acquisition is synchronised with the activation of the cancellation leg. The experimental results are shown in Fig. 5.8, where the individual leg currents and the total output current are reported, while in Fig. 5.9 is reported the detail with $N = 3$ and $D = (N - 0.5)/N$. The instant when the cancellation leg is switched on serves as the time reference, while the grey-shaded region indicates the interval during which it is disabled.

From the results, it can be observed that for all tests conducted at $D = 1/N$, the activation of the cancellation leg has minimal or negligible effect, as the converter already operates under naturally ripple-free conditions. In these cases, the use of the cancellation leg is therefore unnecessary. Conversely, for the other duty cycles, the activation of the cancellation leg consistently improves the output current waveform, effectively cancelling the ripple. This improvement is particularly evident in the configuration with $N = 3$, where the reduced number of legs results in inherently higher ripple amplitude.

The case highlighted in Fig. 5.9 is chosen because it is emblematic of the worst-case scenario tested: the number of power legs is lower, with the duty cycle resulting in maximum ripple at a high power level. It can be seen that the experimental result is in line with that obtained from the simulations. It can also be seen that the non-idealities of the circuit cause an imbalance in the currents, which in turn causes a recirculation current in the cancellation leg even when it is not active.

A further phenomenon visible in the experimental waveforms is the transient that occurs when the cancellation leg is enabled. During this brief interval, the current through the cancellation leg may exceed that of the power legs, but the

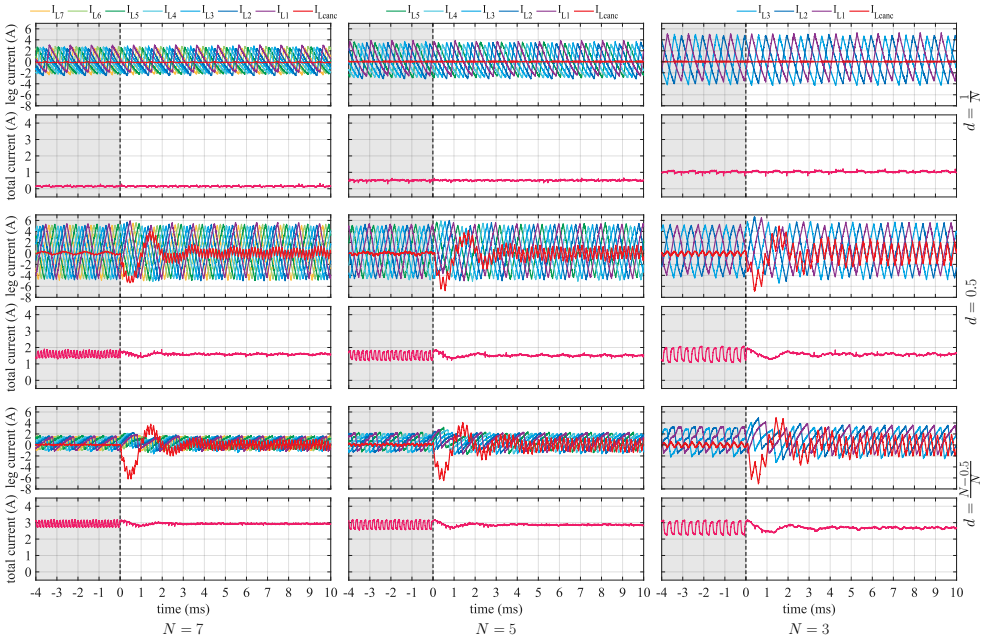

Figure 5.8: Experimental results of the leg and load currents: the left column corresponds to cases with $N = 7$, the centre to $N = 5$, and the right to $N = 3$. From top to bottom, the rows show the results for duty cycles of $d = 1/N$, $d = 1/2$, and $d = (N - 0.5)/N$, respectively. The grey-shaded area represents the time interval before the activation of the cancellation leg.

transient decays very rapidly, typically within a few milliseconds.

It should also be noted that the proposed technique for managing transients could not be implemented for the same reason that dynamic phase shedding could not be implemented.

This transient introduces an important design consideration when the converter operates in open loop, specifically concerning the sizing of the switches in the cancellation leg. In principle, smaller switches could be used for this leg, since under steady-state conditions, when it remains continuously active and the number of power legs is constant, the current flowing through it primarily carries the ripple component. However, in dynamic scenarios where the insertion and deactivation of the cancellation leg occur more frequently, it is advisable to size the switches to withstand possible current overloads during these transient events. The magnitude and repetition rate of such transients may accelerate component ageing; hence, this aspect must be carefully evaluated during the design phase.

These considerations are particularly relevant under open-loop operation. In more realistic closed-loop configurations, or when employing modulation techniques specifically designed for transient management, such as the one discussed in Chapter 4, the amplitude of the current transients can be effectively limited. This allows

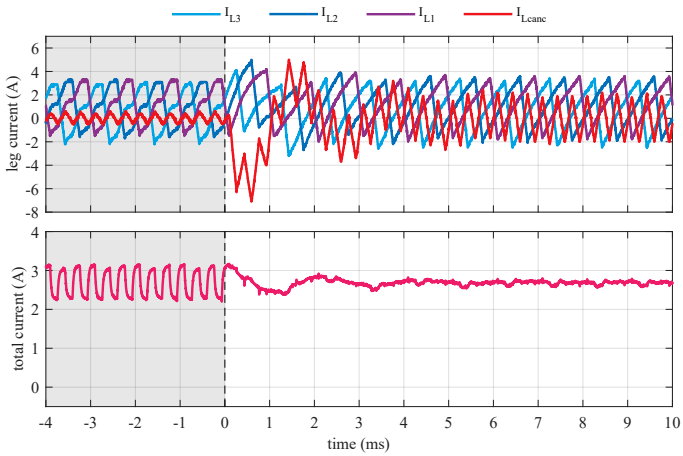

Figure 5.9: Detail of the current in the inductors and on the output when $N = 3$ and $D = (N - 0.5)/N$.

the use of smaller and potentially more cost-effective switches for the cancellation leg, without compromising reliability. It should also be noted that the switching frequency of the cancellation leg varies according to the number of power legs in operation.

Finally, an experimental efficiency assessment is conducted to validate the results of the analytical efficiency analysis. For this purpose, the number of power legs considered is limited to 5, and the switching frequency is fixed at 3 kHz. For the BCM case, the switching frequency is instead varied between 1 and 10 kHz. In the latter configuration, the number of legs is limited to 4, due to the maximum switching frequency constraints imposed by the devices used in the cancellation leg.

Efficiency measurements are carried out for each of the previously analysed converter topologies, SIB, SSIB, and SSIB operating in BCM mode, and the results are subsequently interpolated according to the method proposed in [147] and already discussed in Chapter 4.

The results obtained for each configuration are presented in Fig. 5.10, while their comparison is shown in Fig. 5.11. The experimental trends are in close agreement with the analytical predictions, confirming that the activation of the cancellation leg is beneficial only when strictly necessary. The main deviation between the experimental and analytical analyses is observed in the BCM configuration, which exhibits a slightly higher efficiency than the SIB at output power levels below 100 W. This behaviour is primarily attributed to the specific characteristics and non-idealities of the low-power prototype used during testing. This is probably because the resistance of the inductors used is greater than that considered in the analytical calculation, and thus at low frequencies (and therefore at higher rms values) conduction losses increase more significantly. Furthermore, the

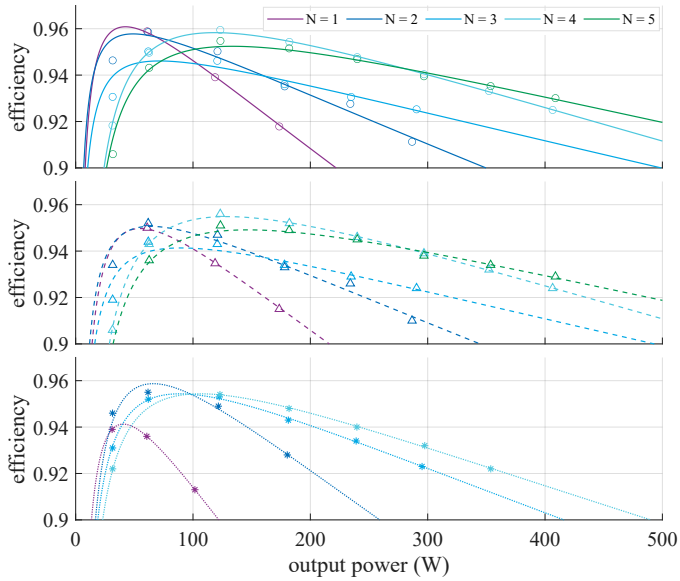

Figure 5.10: Experimentally efficiency curves, the individual points represent the measurement made while the lines represent their interpolation according to [147]: on top the SIB, in the middle the SSIB, and at the bottom the SSIB with BCM.

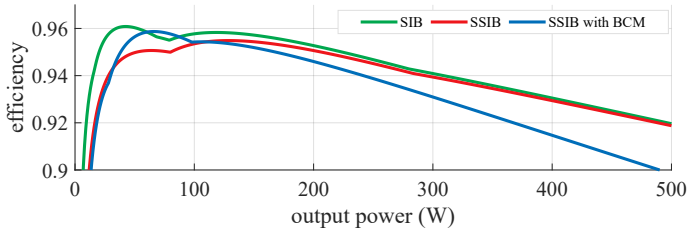

Figure 5.11: Comparison between the upper envelope of the experimental efficiency curves.

switches considered in the analytical case are different from those mounted on the boards used.

The advantages of phase shedding are also clearly demonstrated: at high output power levels, converters operating with a larger number of active legs achieve superior performance, whereas at partial loads, higher efficiency is obtained by deactivating part of the converter legs.

The experimentally measured four-point efficiencies are 93.9%, 93.7%, and 92.7% for the SIB, SSIB, and SSIB operating in BCM mode, respectively. This result does not match exactly with what was found in the analytical analysis, for the reasons already mentioned regarding the operation in BCM. However, as regards the comparison between SIB and SSIB, the experimental results are consistent with what was already found in the analytical analysis.

5.3 Discussion

This thesis provides an overview of the current state of the art in hydrogen production, with a particular emphasis on PV systems as the primary energy source. Among the various converter topologies investigated for this type of application, the SSIB converter is selected. Compared to the SIB topology, this configuration differs through the addition of an extra leg with a series-connected capacitor. The control strategy does not introduce additional complexity, since the control of the cancellation leg can be derived directly from the gate signals of the other legs. Moreover, if desired, the converter can also be operated as a conventional SIB simply by disabling the cancellation leg. As with SIB converters, the modular nature of the topology enables potential cost reductions in both manufacturing and maintenance, while also allowing the implementation of advanced control techniques such as phase shedding to enhance conversion efficiency.

Considering that, in a hydrogen production plant based on water electrolysis, the highest costs are associated with the electrolyser stack and the hydrogen storage system, the additional cost of an extra leg and a capacitor inside the converter can be justified by another key feature of this topology: its ability to completely eliminate the output current ripple under any operating condition. This characteristic is particularly crucial for systems employing PEM electrolysers, as it can prevent premature membrane degradation and avoid the associated reduction in conversion efficiency, thereby contributing to improved system lifetime and overall performance.

The experimental results confirm the findings discussed in the theoretical section: ripple cancellation naturally occurs for all duty cycles corresponding to i/N ($i = 1, ..., N$). At these operating points, the activation of the cancellation leg is unnecessary, as it would reduce converter efficiency without providing any additional benefit. This behaviour has also been verified experimentally.

For all other duty cycle values, a trade-off must be made between higher converter efficiency, at the expense of the electrolyser's lifetime, and complete current ripple cancellation, at the expense of conversion efficiency. The experiments also highlighted the presence of current transients during the insertion of the cancellation leg when no transient control is implemented. Simulations demonstrated that employing the proposed modulation technique for transient management can significantly mitigate current peaks, although this comes at the cost of temporarily losing ripple-free operation during the transient period.

6

Conclusion

This thesis represents the outcome of three years of research in the field of power converters for both Power-to-Gas and Gas-to-Power systems, that is, for hydrogen production and utilisation. This topic has gained significant attention in recent years, largely due to increased funding and strategic interest in the hydrogen sector.

This thesis focuses specifically on a converter topology known as the synchronous stacked interleaved buck. Although this converter is particularly well-suited for supplying PEM electrolysers, it has not yet been adopted in commercial systems. I hope that the results and insights presented in this work will contribute to changing that in the near future.

One of the key features of this converter is its ability to eliminate current ripple under any load conditions. This makes it ideal for powering PEM stacks, which could suffer from reduced conversion efficiency and useful life when subjected to current ripple. It is also a modular converter, which could implement techniques to improve efficiency at partial loads. A modulation technique has therefore been proposed that can combine current ripple cancellation with efficiency maximisation.

Experimental tests have shown that the use of the cancellation leg leads to the cancellation of ripple in all cases where it is not already naturally cancelled by the duty cycle. The use of this extra leg is therefore not necessary if the converter operates at naturally ripple-free points. Furthermore, experimental tests have shown that converter phase shedding improves performance at partial loads. The four-point efficiencies obtained show that, with the prototype used, in the case of interleaved buck alone, almost 94% can be achieved. In contrast, the other cases with the cancellation leg enabled lead to lower efficiencies, 93.7% and 92.7% respectively for stacked phase shedding alone and for stacked phase shedding with BCM.

Despite notable progress, there remains considerable scope for improvement, particularly concerning the materials employed in both electrolyser stacks and storage systems. From the perspective of power electronics, many of the challenges

encountered in this field can be addressed by leveraging solutions and design principles already established in other industrial sectors. Electrically, the greatest potential for advancement lies in optimising overall system architecture, intending to improve the efficiency of energy conversion and management throughout the process.

Regarding the use of a single power converter, a first possible direction for future improvement lies in the development of more advanced partial power processing topologies for PV-electrolyser applications. Such topologies enable more efficient management of the generated power by reducing unnecessary dissipation in semiconductor devices. As already seen in the previous Chapters, current studies mainly focus on two-stage converter configurations, partly due to the fact that partial power processing introduces non-negligible harmonic distortion on the load. If this issue can be mitigated in future designs, a significant increase in system efficiency could be achieved without compromising the lifetime of the electrolyser stack.

A second promising area for improvement concerns the implementation of multi-stack architectures or modular converters. Multi-stack system configurations have already been investigated in renewable applications involving wind sources, and the same concept could be extended to PV-based systems. These architectures enable power distribution among several stacks, thereby reducing operational stress on individual units and enhancing system reliability over the long term.

In addition to multi-stack arrangements, modular converter architectures (either connected in series or parallel) represent another avenue for advancement. Some recent studies have already explored these solutions: in [165], a modular multilevel converter of type π single-phase (π-MMC 1ph) was presented, while in [166], a modular multilevel converter was employed to perform MPPT, with each converter module associated with a single PV panel, although the connection to the electrolyser was not specified. Such modular configurations can enhance PV utilisation by mitigating issues related to partial shading, which are typical of conventional architectures employing a single converter.

Finally, another potential field for future development concerns the adoption of new semiconductor materials, such as SiC, GaN, and diamond-based devices. Currently, the high cost of these technologies limits their attractiveness for applications that already involve significant investment, such as PEM electrolysers. Nevertheless, they may become highly relevant in the future. These materials exhibit superior electrical conductivity, lower conduction losses, improved thermal performance, and allow for higher switching frequencies compared to conventional silicon devices. The latter feature, in particular, can reduce the size of passive filters and transformers, contributing to lower system volume and potentially reduced costs. However, increased switching frequencies also introduce challenges related to electromagnetic interference and electromagnetic compatibility, which must be carefully addressed in system design.

Each Chapter of the thesis is based on work already published or submitted to conferences or journals. Chapter 2 is the result of collaboration with the mechanical engineering group at the University of Bologna, which led to a conference publication [52] and two journal publications [53, 56]. Some considerations in Chapter 3 were developed based on experimental tests carried out with the mechanics group [57]. The literature review was conducted during my period abroad at the University of Le Havre, France, and has now been submitted for publication and is currently under review. Chapters 4 and 5, on the other hand, are based on work already presented at conferences [155] or published in journals [152].

Acknowledgements

I would like to express my heartfelt gratitude to all those who have contributed, in one way or another, to the achievement of this milestone.

First and foremost, my thanks go to all the people with whom I have had the pleasure of working over the past few years. I am deeply grateful to Professor Gabriele Grandi for encouraging me to pursue my PhD, and to my supervisors, Professor Mattia Ricco and Professor Vincenzo Cirimele, for their invaluable guidance and support throughout this journey. My sincere thanks also go to Professor Riccardo Mandrioli for his continuous advice and encouragement.

I would also like to thank all my colleagues, with whom I have shared not only long hours of work but also many enjoyable moments outside the office. A special mention goes to the Mechanical Engineering group, with whom I had the pleasure of collaborating during these three years.

I would also like to extend my gratitude to the Le Havre research group, who welcomed me during the six months I spent there, an experience that proved to be both professionally enriching and personally rewarding. My sincere thanks go to Professor Damien Guilbert for accepting me into his research group, to Omar Amri for his warm hospitality and companionship throughout my stay, and to all the colleagues with whom I had the pleasure of sharing my time and work.

This thesis is dedicated to my grandfather, who always reminded me that studying is less tiring than working. My deepest gratitude goes to my family, who have always supported me and made it possible for me to pursue my studies, and to Gessica, who has stood by my side throughout these years, even when my work often took precedence over our time together.

Finally, I would like to thank all my friends, who have filled my time beyond work with laughter, experiences, and balance. Without them, I would not have had the activities and companionship that helped me relax and regain perspective along the way.

Bibliography

[1] J. Houghton, "Global warming," *Reports on progress in physics*, vol. 68, no. 6, p. 1343, 2005.

[2] O. O. Yolcan, "World energy outlook and state of renewable energy: 10-year evaluation," *Innovation and Green Development*, vol. 2, no. 4, p. 100070, 2023.

[3] G. G. Farivar, W. Manalastas, H. D. Tafti, S. Ceballos, A. Sanchez-Ruiz, E. C. Lovell, G. Konstantinou, C. D. Townsend, M. Srinivasan, and J. Pou, "Grid-connected energy storage systems: State-of-the-art and emerging technologies," *Proceedings of the IEEE*, vol. 111, no. 4, pp. 397–420, 2022.

[4] C. B. B. Farias, R. C. S. Barreiros, M. F. da Silva, A. A. Casazza, A. Converti, and L. A. Sarubbo, "Use of hydrogen as fuel: a trend of the 21st century," *Energies*, vol. 15, no. 1, p. 311, 2022.

[5] L. Van Hoecke, L. Laffineur, R. Campe, P. Perreault, S. W. Verbruggen, and S. Lenaerts, "Challenges in the use of hydrogen for maritime applications," *Energy & Environmental Science*, vol. 14, no. 2, pp. 815–843, 2021.

[6] European Clean Hydrogen Alliance, "Project pipeline of the european clean hydrogen alliance," 2022.

[7] G. Kakoulaki, I. Kougias, N. Taylor, F. Dolci, J. Moya, and A. Jäger-Waldau, "Green hydrogen in europe–a regional assessment: Substituting existing production with electrolysis powered by renewables," *Energy conversion and management*, vol. 228, p. 113649, 2021.

[8] A. Hassan, O. Abdel-Rahim, M. Bajaj, and I. Zaitsev, "Power electronics for green hydrogen generation with focus on methods, topologies, and comparative analysis," *Scientific Reports*, vol. 14, no. 1, p. 24767, 2024.

[9] L. Sánchez, D. Reigosa, A. Bilbao, I. Peña-Gonzalez, and F. Briz, "Comparative analysis of power converter topologies for hydrogen electrolyzers," *IEEE Journal of Emerging and Selected Topics in Power Electronics*, 2024.

[10] B. Yodwong, D. Guilbert, M. Phattanasak, W. Kaewmanee, M. Hinaje, and G. Vitale, "Ac-dc converters for electrolyzer applications: State of the art and future challenges," *Electronics*, vol. 9, no. 6, p. 912, 2020.

[11] M. B. El Kattel, P. P. Praça, R. Mayer, C. d. C. Lucio Berrehil el Kattel, R. P. T. Bascopé, F. L. M. Antunes, and B. de Jesus Cardoso Filho, "Overview of main electrolyzer technologies and power electronic converter topologies for enabling hydrogen production through water electrolysis," *International Journal of Circuit Theory and Applications*, 2024.

[12] M. Chen, S.-F. Chou, F. Blaabjerg, and P. Davari, "Overview of power electronic converter topologies enabling large-scale hydrogen production via water electrolysis," *Applied Sciences*, vol. 12, no. 4, p. 1906, 2022.

[13] D. Guilbert, S. M. Collura, and A. Scipioni, "Dc/dc converter topologies for electrolyzers: State-of-the-art and remaining key issues," *International Journal of Hydrogen Energy*, vol. 42, no. 38, pp. 23966–23985, 2017.

[14] G. Rego, J. Rocha, J. A. Faria, J. L. Afonso, and V. Monteiro, "A review of hydrogen production methods and power electronics converter topologies for green hydrogen applications," *Energies*, vol. 17, no. 22, p. 5579, 2024.

[15] Y. Hidaka and K. Kawahara, "Modeling of a hybrid system of photovoltaic and fuel cell for operational strategy in residential use," in *2012 47th International Universities Power Engineering Conference (UPEC)*, pp. 1–6, IEEE, 2012.

[16] M. Kiaee, A. Cruden, P. Chladek, and D. Infield, "Demonstration of the operation and performance of a pressurised alkaline electrolyser operating in the hydrogen fuelling station in porsgrunn, norway," *Energy Conversion and Management*, vol. 94, pp. 40–50, 2015.

[17] S. Pascuzzi, A. S. Anifantis, I. Blanco, and G. Scarascia Mugnozza, "Electrolyzer performance analysis of an integrated hydrogen power system for greenhouse heating. a case study," *Sustainability*, vol. 8, no. 7, p. 629, 2016.

[18] X. Wang, J. Huang, Z. Xu, C. Zhang, and X. Guan, "Real-world scale deployment of hydrogen-integrated microgrid: design and control," *IEEE Transactions on Sustainable Energy*, 2024.

[19] F. Sayedin, A. Maroufmashat, S. Al-Adwani, S. S. Khavas, A. Elkamel, and M. Fowler, "Evolutionary optimization approaches for direct coupling photovoltaic-electrolyzer systems," in *2015 International Conference on Industrial Engineering and Operations Management (IEOM)*, pp. 1–8, IEEE, 2015.

[20] A. Khalilnejad, A. Sundararajan, and A. I. Sarwat, "Performance evaluation of optimal photovoltaic-electrolyzer system with the purpose of maximum

hydrogen storage," in *2016 IEEE/IAS 52nd Industrial and Commercial Power Systems Technical Conference (I&CPS)*, pp. 1–9, IEEE, 2016.

[21] R. Gaamouche, A. Abbou, A. Redouane, A. El Hasnaoui, and B. Belhorma, "Modeling and simulation of direct coupling of an electrolyzer to pv system for hydrogen production," in *2018 6th International Renewable and Sustainable Energy Conference (IRSEC)*, pp. 1–5, IEEE, 2018.

[22] J. A. Azzolini, M. Tao, K. Ayers, and J. Vacek, "A load-managing photovoltaic system for driving hydrogen production," in *2020 47th IEEE Photovoltaic Specialists Conference (PVSC)*, pp. 1927–1932, IEEE, 2020.

[23] V. Solovey, M. Zipunnikov, and A. Kotenko, "Researching and adjusting the modes of joint operation of a photoelectric converter and a high pressure electrolyzer," *International Journal of Hydrogen Energy*, vol. 47, no. 66, pp. 28272–28279, 2022.

[24] A. Kouache, A. Djafour, K. Benzaoui, A. Gougui, M. Danoune, and M. Ramdani, "Field investigation of green hydrogen production via indirect coupling of pem electrolyzer in southeast algeria," *International Journal of Hydrogen Energy*, 2024.

[25] A. G. Del Valle, P. García-Linares, and A. Martí, "Optimizing hydrogen production: A comparative study of direct and indirect coupling between photovoltaics and electrolyzer," *Energy Conversion and Management*, vol. 315, p. 118751, 2024.

[26] F. Merahi, B. O. Bouamama, S. Mekhilef, *et al.*, "Bond graph modeling, design and experimental validation of a photovoltaic/fuel cell/electrolyzer/battery hybrid power system," *International Journal of Hydrogen Energy*, vol. 46, no. 47, pp. 24011–24027, 2021.

[27] M. K. Behera and L. C. Saikia, "A novel resilient control of grid-integrated solar pv-hybrid energy storage microgrid for power smoothing and pulse power load accommodation," *IEEE Transactions on Power Electronics*, vol. 38, no. 3, pp. 3965–3980, 2022.

[28] M. Abdo, M. A. Abdel-Rahman, M. Amer, and S. Helmy, "Harmonic domain model of a hybrid pv-hydrogen/fc-electrolyzer system for steady-state analysis," in *2023 24th International Middle East Power System Conference (MEPCON)*, pp. 1–6, IEEE, 2023.

[29] S. S. Kumar and V. Himabindu, "Hydrogen production by pem water electrolysis–a review," *Materials Science for Energy Technologies*, vol. 2, no. 3, pp. 442–454, 2019.

[30] IEA, "Global hydrogen review 2025." `https://www.iea.org/reports/global-hydrogen-review-2025`, 2025. [Online; accessed 29-October-2025].

[31] F. Dawood, M. Anda, and G. Shafiullah, "Hydrogen production for energy: An overview," *International Journal of Hydrogen Energy*, vol. 45, no. 7, pp. 3847–3869, 2020.

[32] G. Salerno, B. Cecconi, O. Bettucci, M. Monai, L. Zani, D. Franchi, M. Calamante, A. Mordini, T. Montini, P. Fornasiero, *et al.*, "Enhanced long-term stability of a photosensitizer with a hydroxamic acid anchor in dye-sensitized photocatalytic hydrogen generation," *European Journal of Organic Chemistry*, vol. 26, no. 45, p. e202300924, 2023.

[33] A. Mohammadi and M. Mehrpooya, "A comprehensive review on coupling different types of electrolyzer to renewable energy sources," *Energy*, vol. 158, pp. 632–655, 2018.

[34] P. Millet, "Fundamentals of water electrolysis," *Hydrogen Production: Electrolysis*, pp. 33–62, 2015.

[35] S. E. Hosseini, *Fundamentals of Hydrogen Production and Utilization in Fuel Cell Systems*. Elsevier, 2023.

[36] F. Marangio, M. Santarelli, and M. Calì, "Theoretical model and experimental analysis of a high pressure pem water electrolyser for hydrogen production," *International journal of hydrogen energy*, vol. 34, no. 3, pp. 1143–1158, 2009.

[37] M. Koundi, H. El Fadil, Z. EL Idrissi, A. Lassioui, A. Intidam, T. Bouanou, S. Nady, and A. Rachid, "Investigation of hydrogen production system-based pem el: Pem el modeling, dc/dc power converter, and controller design approaches," *Clean Technologies*, vol. 5, no. 2, pp. 531–568, 2023.

[38] M. David, C. Ocampo-Martínez, and R. Sánchez-Peña, "Advances in alkaline water electrolyzers: A review," *Journal of Energy Storage*, vol. 23, pp. 392–403, 2019.

[39] G. Kaur, *PEM fuel cells: fundamentals, advanced technologies, and practical application*. Elsevier, 2021.

[40] D. Falcão and A. Pinto, "A review on pem electrolyzer modelling: Guidelines for beginners," *Journal of cleaner production*, vol. 261, p. 121184, 2020.

[41] C. Li and J.-B. Baek, "The promise of hydrogen production from alkaline anion exchange membrane electrolyzers," *Nano Energy*, vol. 87, p. 106162, 2021.

[42] M. M. Nejadian, P. Ahmadi, and E. Houshfar, "Comparative optimization study of three novel integrated hydrogen production systems with soec, pem, and alkaline electrolyzer," *Fuel*, vol. 336, p. 126835, 2023.

[43] M. Ni, M. K. Leung, and D. Y. Leung, "Technological development of hydrogen production by solid oxide electrolyzer cell (soec)," *International journal of hydrogen energy*, vol. 33, no. 9, pp. 2337–2354, 2008.

[44] G. Flis and G. Wakim, "Solid oxide electrolysis: a technology status assessment," *Clean Air Task Force*, 2023.

[45] M. Benghanem, H. Almohamadi, S. Haddad, A. Mellit, and N. Chettibi, "The effect of voltage and electrode types on hydrogen production powered by photovoltaic system using alkaline and pem electrolyzers," *International Journal of Hydrogen Energy*, vol. 57, pp. 625–636, 2024.

[46] H. Sayed-Ahmed, Á. I. Toldy, and A. Santasalo-Aarnio, "Dynamic operation of proton exchange membrane electrolyzers—critical review," *Renewable and Sustainable Energy Reviews*, vol. 189, p. 113883, 2024.

[47] Hydrogen Europe, "Clean hydrogen production pathways report 2024." `https://hydrogeneurope.eu/wp-content/uploads/2024/06~âĂę`, 2024. [Online; accessed 27-January-2025].

[48] A. M. Elberry, J. Thakur, A. Santasalo-Aarnio, and M. Larmi, "Large-scale compressed hydrogen storage as part of renewable electricity storage systems," *International journal of hydrogen energy*, vol. 46, no. 29, pp. 15671–15690, 2021.

[49] F. Ghaffari-Tabrizi, J. Haemisch, and D. Lindner, "Reducing hydrogen boil-off losses during fuelling by pre-cooling cryogenic tank," *Hydrogen*, vol. 3, no. 2, pp. 255–269, 2022.

[50] T. Zhang, J. Uratani, Y. Huang, L. Xu, S. Griffiths, and Y. Ding, "Hydrogen liquefaction and storage: Recent progress and perspectives," *Renewable and Sustainable Energy Reviews*, vol. 176, p. 113204, 2023.

[51] N. Klopčič, I. Grimmer, F. Winkler, M. Sartory, and A. Trattner, "A review on metal hydride materials for hydrogen storage," *Journal of Energy Storage*, vol. 72, p. 108456, 2023.

[52] R. Alleori, M. A. Ancona, M. Bianchi, F. Falcetelli, F. Ferrari, and P. Pilati, "An experimental test bench for the thermal conditioning analysis of absorption and desorption cycles of hydrogen within metal hydrides storage tanks," in *37th International Conference on Efficiency, Cost, Optimization,*

Simulation and Environmental Impact of Energy Systems, ECOS 2024, vol. 2, pp. 1131–1142, ECOS 2024, 2024.

[53] R. Alleori, M. A. Ancona, M. Bianchi, F. Falcetelli, F. Ferrari, F. Melino, P. Pilati, and M. Ricco, "Experimental analysis on a power-to-hydrogen system based on pem electrolysis and metal hydrides: Empirical correlations for optimal system design and performance improvement," *International Journal of Hydrogen Energy*, vol. 128, pp. 306–318, 2025.

[54] T. Førde, "Theoretical and experimental studies of metal hybride storage units," 2007.

[55] K. Nivedhitha, T. Beena, N. Banapurmath, M. Umarfarooq, V. Ramasamy, M. E. M. Soudagar, and Ü. Ağbulut, "Advances in hydrogen storage with metal hydrides: mechanisms, materials, and challenges," *International Journal of Hydrogen Energy*, vol. 61, pp. 1259–1273, 2024.

[56] R. Alleori, M. A. Ancona, M. Bianchi, F. Falcetelli, F. Ferrari, and P. Pilati, "Experimental analysis of ab2 metal hydride storage in pem power-to-hydrogen systems: Integration and energy trade-offs," *Journal of Energy Storage*, vol. 134, p. 118161, 2025.

[57] P. Pilati, F. Ferrari, R. Alleori, F. Falcetelli, M. A. Ancona, F. Melino, M. Bianchi, and M. Ricco, "Experimental analysis on a commercial power electronic converter in power-to-hydrogen system based on pem electrolysis and metal hydrides," *Energies*, vol. 18, no. 11, p. 2831, 2025.

[58] Y. Manoharan, S. E. Hosseini, B. Butler, H. Alzhahrani, B. T. F. Senior, T. Ashuri, and J. Krohn, "Hydrogen fuel cell vehicles; current status and future prospect," *Applied Sciences*, vol. 9, no. 11, p. 2296, 2019.

[59] J. Wu, X. Z. Yuan, J. J. Martin, H. Wang, J. Zhang, J. Shen, S. Wu, and W. Merida, "A review of pem fuel cell durability: Degradation mechanisms and mitigation strategies," *Journal of Power Sources*, vol. 184, no. 1, pp. 104–119, 2008.

[60] J. Zhang, Q. Xun, M. Liserre, and H. Yang, "Health-aware bi-level optimization of component sizing and real-time energy management in fuel cell hybrid electric trucks," *IEEE Transactions on Industry Applications*, 2024.

[61] M. M. Tellez-Cruz, J. Escorihuela, O. Solorza-Feria, and V. Compañ, "Proton exchange membrane fuel cells (pemfcs): Advances and challenges," *Polymers*, vol. 13, p. 3064, Sept. 2021.

[62] L. Järvinen, P. Puranen, V. Ruuskanen, A. Kosonen, P. Kauranen, J. Ahola, and C. Chatzichristodoulou, "Experimental study of alkaline water electrolyzer performance and frequency behavior under high frequency dynamic operation," *International Journal of Hydrogen Energy*, vol. 67, pp. 50–61, 2024.

[63] F. Parache, H. Schneider, C. Turpin, N. Richet, O. Debellemanière, É. Bru, A. T. Thieu, C. Bertail, and C. Marot, "Impact of power converter current ripple on the degradation of pem electrolyzer performances," *Membranes*, vol. 12, p. 109, Jan. 2022.

[64] E. Pahon, M.-C. Péra, D. Bouquain, and D. Hissel, "Impact of current ripples on the durability of proton exchange membrane fuel cells based on two ageing datasets," *Data in Brief*, vol. 45, p. 108601, 2022.

[65] Y. Zhan, Y. Guo, J. Zhu, B. Liang, and B. Yang, "Comprehensive influences measurement and analysis of power converter low frequency current ripple on pem fuel cell," *International Journal of Hydrogen Energy*, vol. 44, p. 31352–31359, Nov. 2019.

[66] J. Kim, I. Lee, Y. Tak, and B. Cho, "Impedance-based diagnosis of polymer electrolyte membrane fuel cell failures associated with a low frequency ripple current," *Renewable Energy*, vol. 51, p. 302–309, Mar. 2013.

[67] T. Jarry, A. Jaafar, C. Turpin, F. Lacressonniere, E. Bru, O. Rallieres, and M. Scohy, "Impact of high frequency current ripples on the degradation of high-temperature pem fuel cells (ht-pemfc)," *International Journal of Hydrogen Energy*, vol. 48, p. 20734–20742, June 2023.

[68] B. Wahdame, L. Girardot, D. Hissel, F. Harel, X. François, D. Candusso, M. C. Pera, and L. Dumercy, "Impact of power converter current ripple on the durability of a fuel cell stack," in *2008 IEEE international symposium on industrial electronics*, pp. 1495–1500, IEEE, 2008.

[69] Y. Zhan, Y. Guo, J. Zhu, and L. Li, "Input current ripple reduction and high efficiency for pem fuel cell power conditioning system," in *2017 20th International Conference on Electrical Machines and Systems (ICEMS)*, pp. 1–6, IEEE, 2017.

[70] H. P. Buitendach, R. Gouws, C. A. Martinson, C. Minnaar, and D. Bessarabov, "Effect of a ripple current on the efficiency of a pem electrolyser," *Results in Engineering*, vol. 10, p. 100216, June 2021.

[71] J. E. Valdez-Resendiz, J. C. Rosas-Caro, V. M. Sanchez, and A. R. Lopez-Nuñez, "Experimental study of a fuel cell stack performance operating

with a power electronics converter with high-frequency current ripple," *International Journal of Hydrogen Energy*, 2024.

[72] M. Gerard, J.-P. Poirot-Crouvezier, D. Hissel, and M.-C. Péra, "Ripple current effects on pemfc aging test by experimental and modeling," *Journal of Fuel Cell Science and Technology*, vol. 8, p. 021004, 11 2010.

[73] L. Arriaga, W. Martinez, U. Cano, and H. Blud, "Direct coupling of a solar-hydrogen system in mexico," *International journal of hydrogen energy*, vol. 32, no. 13, pp. 2247–2252, 2007.

[74] R. Clarke, S. Giddey, F. Ciacchi, S. Badwal, B. Paul, and J. Andrews, "Direct coupling of an electrolyser to a solar pv system for generating hydrogen," *International journal of hydrogen energy*, vol. 34, no. 6, pp. 2531–2542, 2009.

[75] A. Di Caro and G. Vitale, "Direct-coupled improvement of a solar-powered proton exchange membrane electrolyzer by a reconfigurable source," *Clean Technologies*, vol. 6, no. 3, pp. 1203–1228, 2024.

[76] F. A. Omar, "A new approach for improving the efficiency of the indirectly coupled photovoltaic-electrolyzer system," *International Journal of Hydrogen Energy*, vol. 48, no. 24, pp. 8768–8782, 2023.

[77] Z. Sun, Y. Peng, and D. Zhang, "A control method based on improved cuckoo algorithm for photovoltaic hybrid hydrogen production system," in *2024 The 9th International Conference on Power and Renewable Energy (ICPRE)*, pp. 1056–1060, IEEE, 2024.

[78] L. Zou, Q. Shen, G. Yang, S. Li, and N. Huang, "Improved hydrogen production efficiency of a photovoltaic-electrolysis system with p&o algorithm: A case study," *Chemical Physics Letters*, vol. 832, p. 140891, 2023.

[79] M. Awad, M. M. Mahmoud, Z. Elbarbary, L. Mohamed Ali, S. N. Fahmy, and A. I. Omar, "Design and analysis of photovoltaic/wind operations at mppt for hydrogen production using a pem electrolyzer: Towards innovations in green technology," *PLoS One*, vol. 18, no. 7, p. e0287772, 2023.

[80] C. Kaddachi, R. Harrabi, S. Farhani, H. Grissa, and F. Bacha, "Modeling and control of photovoltaic hydrogen production system," in *2024 IEEE International Conference on Advanced Systems and Emergent Technologies (IC_ASET)*, pp. 1–5, IEEE, 2024.

[81] S. Farhani, C. Kaddachi, and F. Bacha, "Study and simulation of green hydrogen production systems coupled with concentrated photovoltaic

generators," in *2024 IEEE International Conference on Artificial Intelligence & Green Energy (ICAIGE)*, pp. 1–5, IEEE, 2024.

[82] M. Albarghot and L. Rolland, "Matlab/simulink modelling and experimental results of a pem electrolyzer powered by a solar panel," in *2016 IEEE electrical power and energy conference (EPEC)*, pp. 1–6, IEEE, 2016.

[83] A. Harikrishnan, P. Mehta, and P. Bharadwaj, "High performance switched moded power conversion for photovoltaic integrated hydrogen based energy system," in *2023 IEEE 3rd International Conference on Smart Technologies for Power, Energy and Control (STPEC)*, pp. 1–6, IEEE, 2023.

[84] R. Mas, D. Pichilingue, A. Berastain, and C. Celis, "On the application of sliding mode control to indirectly coupled photovoltaic-electrolyzer systems used in the production of clean energy," *International Journal of Thermofluids*, vol. 23, p. 100747, 2024.

[85] Z. Han, S. Yuan, J. Wang, Y. Dong, L. Gao, and Y. Yang, "Modeling and control of photovoltaic hydrogen production system adapting to power fluctuations," in *2021 IEEE 5th Conference on Energy Internet and Energy System Integration (EI2)*, pp. 2835–2840, IEEE, 2021.

[86] C. Miron, N. Christov, and S. C. Olteanu, "Energy management of photovoltaic systems using fuel cells," in *2016 20th International Conference on System Theory, Control and Computing (ICSTCC)*, pp. 749–754, IEEE, 2016.

[87] C. Pradhan, M. K. Senapati, S. G. Malla, P. K. Nayak, and T. Gjengedal, "Coordinated power management and control of standalone pv-hybrid system with modified iwo-based mppt," *IEEE Systems Journal*, vol. 15, no. 3, pp. 3585–3596, 2020.

[88] M. M. Gulzar, A. Iqbal, D. Sibtain, and M. Khalid, "An innovative converterless solar pv control strategy for a grid connected hybrid pv/wind/fuel-cell system coupled with battery energy storage," *IEEE Access*, vol. 11, pp. 23245–23259, 2023.

[89] Y. Xia, H. Cheng, H. He, Z. Hu, and W. Wei, "Efficiency enhancement for alkaline water electrolyzers directly driven by fluctuating pv power," *IEEE Transactions on Industrial Electronics*, vol. 71, no. 6, pp. 5755–5765, 2023.

[90] M. El Amri, R. Z. Falama, A. S. Saidi, and C. B. Salah, "Study of hydrogen production and storage pv system," in *2022 IEEE 21st international Ccnference on Sciences and Techniques of Automatic Control and Computer Engineering (STA)*, pp. 528–532, IEEE, 2022.

[91] M. E. Amri and C. B. Salah, "Study of a pv/battery system for hydrogen production and storage," in *2022 IEEE 21st international Ccnference on Sciences and Techniques of Automatic Control and Computer Engineering (STA)*, pp. 522–527, IEEE, 2022.

[92] N. Tlili, B. Neily, and F. B. Salem, "Modeling and simulation of hybrid system coupling a photovoltaic generator, a pem fuel cell and an electrolyzer (part i)," in *2014 IEEE 11th International Multi-Conference on Systems, Signals & Devices (SSD14)*, pp. 1–8, IEEE, 2014.

[93] N. Tlili, B. Neily, and F. Ben Salem, "Modeling and simulation of hybrid system coupling a photovoltaic generator, a pem fuel cell and an electrolyzer (part ii)," in *2014 IEEE 11th International Multi-Conference on Systems, Signals & Devices (SSD14)*, pp. 1–7, 2014.

[94] S. Z. Hassan, S. Mumtaz, T. Kamal, and L. Khan, "Performance of grid-integrated photovoltaic/fuel cell/electrolyzer/battery hybrid power system," in *2015 Power Generation System and Renewable Energy Technologies (PGSRET)*, pp. 1–8, IEEE, 2015.

[95] V. M. Lopez, O. Isabella, M. Zeman, and H. Ziar, "Battery-less uncertainty-based control of a stand-alone pv-electrolyzer system," *Journal of Power Sources*, vol. 614, p. 234934, 2024.

[96] M. Koundi and H. EL FADIL, "Mathematical modeling of pem electrolyzer and design of a voltage controller by the smpwm approach," in *2019 international conference on power generation systems and renewable energy technologies (PGSRET)*, pp. 1–6, IEEE, 2019.

[97] R. A. A. Rodríguez, J. A. G. Moreno, L. N. R. Castañeda, and J. Trujillo, "Modeling and simulation of a non-linear high-power quadratic buck converter from design analysis," *Encuentro Internacional de Educación en Ingeniería*, 2023.

[98] A. B. Makhloufi, M. Hatti, and R. Taleb, "Comparative study of photovoltaic system for hydrogen electrolyzer system," in *2017 6th International Conference on Systems and Control (ICSC)*, pp. 445–450, IEEE, 2017.

[99] S. Cuk and R. Middlebrook, "Advances in switched-mode power conversion part ii," *IEEE Transactions on Industrial Electronics*, no. 1, pp. 19–29, 1983.

[100] R. R. Makineni, D. Sutanto, K. M. Muttaqi, M. R. Islam, and A. P. Agalgaonkar, "Dual loop cascade control of a stacked interleaved buck converter for electrolyzer application," in *2022 IEEE IAS Global Conference on Emerging Technologies (GlobConET)*, pp. 1029–1035, IEEE, 2022.

[101] D. Iannuzzi and M. Pagano, "Efficiency of hydrogen based storage systems for stand-alone pv applications: Numerical and experimental results," in *2009 International Conference on Clean Electrical Power*, pp. 555–561, IEEE, 2009.

[102] H. Djoudi, A. Badji, N. Benyahia, M. Zaouia, H. Denoun, and N. Benamrouche, "Modeling and power management control of the photovoltaic and fuel cell/electrolyzer system for stand-alone applications," in *2015 4th International Conference on Electrical Engineering (ICEE)*, pp. 1–6, IEEE, 2015.

[103] M. Maaruf and M. Khalid, "Hybrid solar/pem fuel cell/and water electrolyzer energy system for all-electric ship," in *2022 IEEE Kansas Power and Energy Conference (KPEC)*, pp. 1–5, IEEE, 2022.

[104] M. A. Bayoumi, F. El Sayed, M. G. Abdallah, A. M. Atallah, and D. M. Hafez, "Investigation of green hydrogen production and storage from pv arrays connected to an ac microgrid system," in *2023 International Telecommunications Conference (ITC-Egypt)*, pp. 157–164, IEEE, 2023.

[105] M. M. Rahman, G. Antonini, and J. M. Pearce, "Open-source dc-dc converter enabling direct integration of solar photovoltaics with anion exchange membrane electrolyzer for green hydrogen production," *International Journal of Hydrogen Energy*, vol. 88, pp. 333–343, 2024.

[106] L. Palma, B. Molina, and A. Díaz, "Design and sizing of power conversion system with energy storage for improved pv-electrolyzer energy coupling," in *2023 International Conference on Clean Electrical Power (ICCEP)*, pp. 784–788, IEEE, 2023.

[107] K. Agbossou, M. Kolhe, J. Hamelin, and T. K. Bose, "Performance of a stand-alone renewable energy system based on energy storage as hydrogen," *IEEE Transactions on energy Conversion*, vol. 19, no. 3, pp. 633–640, 2004.

[108] K. Agbossou, S. Kélouwani, A. Anouar, and M. Kolhe, "Energy management of hydrogen-based stand-alone renewable energy system by using boost and buck converters," in *Conference Record of the 2004 IEEE Industry Applications Conference, 2004. 39th IAS Annual Meeting.*, vol. 4, pp. 2786–2793, IEEE, 2004.

[109] M. L. Doumbia, K. Agbossou, and E. Granger, "Simulink modelling and simulation of a hydrogen based photovoltaic/wind energy system," in *EUROCON 2007-The International Conference on" Computer as a Tool"*, pp. 2067–2072, IEEE, 2007.

[110] M. L. Doumbia, K. Agbossou, and E. Granger, "Modelling and simulation of a hydrogen based photovoltaic/wind energy system," in *2007 IEEE International Symposium on Industrial Electronics*, pp. 2601–2606, IEEE, 2007.

[111] R. K. Kumar and P. Samuel, "Designing a hydrogen generation system through pem water electrolysis with the capability to adjust fast fluctuations in photovoltaic power," *International Journal of Hydrogen Energy*, vol. 82, pp. 1–10, 2024.

[112] N. Dahmane, A. Djerioui, S. Zeghlache, Z. E. Dahmane, A. Houari, and A. Hadjkaddour, "Energy management of pv/fc/bat/sc and pem electrolyzer," in *2022 IEEE International Conference on Electrical Sciences and Technologies in Maghreb (CISTEM)*, vol. 4, pp. 1–6, IEEE, 2022.

[113] F. N. Shaker, A. A. Obed, and A. J. Abid, "Comprehensive design for a neuro-fuzzy controller for a safe hydrogen energy storage," in *2022 10th International Conference on Smart Grid (icSmartGrid)*, pp. 124–130, IEEE, 2022.

[114] S. S. Kumar, N. Mukundan, and P. Jayaprakash, "Modified lms control for a grid interactive pv–fuel cell–electrolyzer hybrid system with power dispatch to the grid," *IEEE Transactions on Industry Applications*, vol. 58, no. 6, pp. 7907–7918, 2022.

[115] Y. Zhong, Y. Peng, H. Chen, G. Hao, F. Gao, and Z. Zhou, "An improved particle swarm optimization algorithm-based mppt method for distributed photovoltaic hydrogen production systems," in *2024 The 9th International Conference on Power and Renewable Energy (ICPRE)*, pp. 1091–1096, IEEE, 2024.

[116] M. B. Hossain, M. R. Islam, K. M. Muttaqi, D. Sutanto, and A. P. Agalgaonkar, "A compensation strategy for mitigating intermittencies within a pv powered microgrid using a hybrid multilevel energy storage system," *IEEE Transactions on Industry Applications*, vol. 59, no. 4, pp. 5074–5086, 2023.

[117] R. Bhosale and V. Agarwal, "Control of fuel cell and electrolyzer based hydrogen storage system with ultra-capacitor for voltage stability and enhanced transient stability of a dc micro grid," in *2018 International Conference on Power, Instrumentation, Control and Computing (PICC)*, pp. 1–6, IEEE, 2018.

[118] X. Liu, J. Zou, R. Long, Z. Liu, and W. Liu, "Variable period sequence control strategy for an off-grid photovoltaic-pem electrolyzer hydrogen generation system," *Renewable Energy*, vol. 216, p. 119074, 2023.

[119] T. F. Rech, T. Orlando, R. F. Coelho, and A. L. Kirsten, "Step-down converter for low current ripple in electrolyzer with mppt control strategy," in *2023 IEEE 8th Southern Power Electronics Conference (SPEC)*, pp. 1–7, IEEE, 2023.

[120] R. R. Makineni, A. P. Agalgaonkar, K. M. Muttaqi, M. R. Islam, and D. Sutanto, "Integral sliding mode control of a stacked interleaved buck converter for electrolyzers supplied with renewable energy sources," *IEEE Transactions on Industry Applications*, 2024.

[121] A. M. Elbakly, I. Abdelsalam, and M. I. Marei, "Interleaved multi-port non-isolated dc/dc converter for green hydrogen production with pv/pem electrolyzer system," in *2025 7th International Youth Conference on Radio Electronics, Electrical and Power Engineering (REEPE)*, pp. 1–5, IEEE, 2025.

[122] Y. Yonezawa, M. Atsushi, H. Nakao, H. Takauchi, Y. Nakashima, H. Ebe, D. Yamashita, M. Sugiyama, Y. Ota, and K. Nishioka, "Model-based development of solar-to-hydrogen conversion system with dynamic operating point control of multiple dc-dc converters," in *2018 7th International Conference on Renewable Energy Research and Applications (ICRERA)*, pp. 1435–1440, IEEE, 2018.

[123] D. Yamashita, H. Nakao, Y. Yonezawa, Y. Nakashima, Y. Ota, K. Nishioka, and M. Sugiyama, "A new solar to hydrogen conversion system with high efficiency and flexibility," in *2017 IEEE 6th International Conference on Renewable Energy Research and Applications (ICRERA)*, pp. 441–446, IEEE, 2017.

[124] M. Geske, D. Ablakovic, K. Jalili, and C. Keller, "Direct coupling of solar plants and electrolyzers with voltage-source converters," in *2024 IEEE Sixth International Conference on DC Microgrids (ICDCM)*, pp. 1–8, IEEE, 2024.

[125] Z. Kang and F. Duan, "A flexible load adaptive control strategy for efficient photovoltaic hydrogen generation system," *Solar Energy*, vol. 266, p. 112150, 2023.

[126] O. Abdel-Rahim, A. A. Arafa, *et al.*, "Efficient integration of pv panels and electrolysis through a high-performance converter for clean hydrogen generation," *Journal of Advanced Research in Applied Sciences and Engineering Technology*, vol. 52, no. 2, pp. 26–34, 2025.

[127] D. Concha, H. Renaudineau, M. S. Hernandez, A. M. Llor, and S. Kouro, "Evaluation of dcx converters for off-grid photovoltaic-based green hydrogen production," *International Journal of Hydrogen Energy*, vol. 46, no. 38, pp. 19861–19870, 2021.

[128] H. Renaudineau, A. M. Llor, M. S. Hernandez, D. Concha, A. H. Wilson-Veas, and S. Kouro, "Photovoltaic to electrolysis off-grid green hydrogen production with dc–dc conversion," *Renewable Energy*, vol. 237, p. 121687, 2024.

[129] K. Kim, J.-H. Kim, J.-P. Lee, T.-J. Kim, and C.-Y. Oh, "Converter design and control strategy for pem water electrolyzer to increase hydrogen generation using hardware-in-the-loop simulation," in *2024 IEEE Applied Power Electronics Conference and Exposition (APEC)*, pp. 2960–2964, IEEE, 2024.

[130] P. Chandrasekhar and S. R. Reddy, "Performance of soft-switched dc-dc resonant converter for electrolyzer," in *2011 4th International Symposium on Resilient Control Systems*, pp. 95–100, IEEE, 2011.

[131] J. Xiong, Y. Xia, Y. Peng, and W. Wei, "A multi-mode self-optimization electrolysis converting strategy for improving efficiency of alkaline water electrolyzers," *IEEE Transactions on Power Electronics*, 2023.

[132] C. Cavallaro, V. Cecconi, F. Chimento, S. Musumeci, C. Santonocito, and C. Sapuppo, "A phase-shift full bridge converter for the energy management of electrolyzer systems," in *2007 IEEE International Symposium on Industrial Electronics*, pp. 2649–2654, IEEE, 2007.

[133] T. Yu, J. Meng, Z. Xu, H. Xie, Z. Jia, and H. Quan, "Modeling and simulation of photovoltaic off-grid hydrogen production system," in *2022 International Conference on Environmental Science and Green Energy (ICESGE)*, pp. 181–186, IEEE, 2022.

[134] X. Li, N. Li, W. Xue, W. Mao, S. Qiu, and X. Wu, "Lcc-resonant-type current-fed-out three-port dc–dc converter for pv electrolytic hydrogen production integrated with energy storage," *IEEE Transactions on Industrial Electronics*, 2024.

[135] A. Merrouche, T. Talbert, D. Matt, T. Martiré, and G. Pellecuer, "Interconnection of renewable sources: Multi-active-bridge converter," in *2024 IEEE International Conference on Industrial Technology (ICIT)*, pp. 1–5, IEEE, 2024.

[136] A. Khosroshahi, M. Abapour, and M. Sabahi, "Reliability evaluation of conventional and interleaved dc–dc boost converters," *IEEE Transactions on Power Electronics*, vol. 30, no. 10, pp. 5821–5828, 2014.

[137] M. Murken and P. Gratzfeld, "Reliability comparison of bidirectional automotive dc/dc converters," in *2017 IEEE 86th Vehicular Technology Conference (VTC-Fall)*, pp. 1–7, IEEE, 2017.

[138] Y. Song, P. A. Schirmer, P. Schreivogel, K. Zhang, H. Wang, and F. Blaabjerg, "On the sensitivity analysis in reliability evaluation for power electronic converters," *IEEE Transactions on Power Electronics*, 2025.

[139] Y. Zhan, Y. Guo, J. Zhu, L. Li, B. Yang, and B. Liang, "A review on mitigation technologies of low frequency current ripple injected into fuel cell and a case study," *International Journal of Hydrogen Energy*, vol. 45, no. 46, pp. 25167–25190, 2020.

[140] A. Valarmathy and M. Prabhakar, "Non-isolated high gain dc–dc converter with ripple-free source current," *Scientific Reports*, vol. 14, no. 1, p. 973, 2024.

[141] D. Jackson and S. Leeb, "Feedforward ripple cancellation for a full-bridge converter," in *APEC 2000. Fifteenth Annual IEEE Applied Power Electronics Conference and Exposition (Cat. No. 00CH37058)*, vol. 1, pp. 347–352, IEEE, 2000.

[142] H. Seok, B. Han, B.-H. Kwon, and M. Kim, "High step-up resonant dc–dc converter with ripple-free input current for renewable energy systems," *IEEE Transactions on Industrial Electronics*, vol. 65, no. 11, pp. 8543–8552, 2018.

[143] J. Wang, W. G. Dunford, and K. Mauch, "Analysis of a ripple-free input-current boost converter with discontinuous conduction characteristics," *IEEE transactions on power electronics*, vol. 12, no. 4, pp. 684–694, 1997.

[144] E. Chou, F. Chen, C. Adragna, and B. Lu, "Ripple steering ac-dc converters to minimize input filter," in *2009 IEEE Energy Conversion Congress and Exposition*, pp. 1325–1330, IEEE, 2009.

[145] M. J. Schutten, R. L. Steigerwald, and J. A. Sabaté, "Ripple current cancellation circuit," in *Eighteenth Annual IEEE Applied Power Electronics Conference and Exposition, 2003. APEC'03.*, vol. 1, pp. 464–470, IEEE, 2003.

[146] J. C. Rosas-Caro, F. Mancilla-David, J. C. Mayo-Maldonado, J. M. Gonzalez-Lopez, H. L. Torres-Espinosa, and J. E. Valdez-Resendiz, "A transformer-less high-gain boost converter with input current ripple cancelation at a selectable duty cycle," *IEEE Transactions on Industrial Electronics*, vol. 60, no. 10, pp. 4492–4499, 2012.

[147] J. W. Kolar, F. Krismer, Y. Lobsiger, J. Muhlethaler, T. Nussbaumer, and J. Minibock, "Extreme efficiency power electronics," in *2012 7th International Conference on Integrated Power Electronics Systems (CIPS)*, pp. 1–22, IEEE, 2012.

[148] J. Wibben and R. Harjani, "A high-efficiency dc–dc converter using 2 nh integrated inductors," *IEEE Journal of Solid-State Circuits*, vol. 43, no. 4, pp. 844–854, 2008.

[149] M. A. Alharbi, M. S. Dahidah, S. A. Ali, S. A. Ethni, and V. Pickert, "Ripple-free multiphase interleaved stacked converter for high-power applications," *IEEE Transactions on Power Electronics*, vol. 37, no. 12, pp. 14770–14780, 2022.

[150] L. Zhang, M. Han, W. Bao, Y. Dong, Y. Fan, and H. Liu, "Low-ripple high-efficiency ac-dc rectifier with auxiliary compensator for hydrogen production," *IET Power Electronics*, vol. 16, no. 12, pp. 2091–2102, 2023.

[151] X. Guo, S. Zhang, Z. Liu, L. Sun, Z. Lu, C. Hua, and J. M. Guerrero, "A new multi-mode fault-tolerant operation control strategy of multiphase stacked interleaved buck converter for green hydrogen production," *International Journal of Hydrogen Energy*, vol. 47, no. 71, pp. 30359–30370, 2022.

[152] P. Pilati, R. Mandrioli, V. Cirimele, D. Guilbert, and M. Ricco, "Phase shedding of a ripple-free stacked interleaved boost converter for fuel cell-based powertrains," *IEEE Transactions on Transportation Electrification*, 2025.

[153] K. Drobnic, G. Grandi, M. Hammami, R. Mandrioli, M. Ricco, A. Viatkin, and M. Vujacic, "An output ripple-free fast charger for electric vehicles based on grid-tied modular three-phase interleaved converters," *IEEE Transactions on Industry Applications*, vol. 55, p. 6102–6114, Nov. 2019.

[154] R. Mandrioli, M. Ricco, M. Hammami, A. Viatkin, and G. Grandi, "A ripple-free output current interleaved dc/dc converter design algorithm for ev charging," in *2021 22nd IEEE International Conference on Industrial Technology (ICIT)*, p. 292–297, IEEE, Mar. 2021.

[155] P. Pilati, F. L. Franco, V. Cirimele, V. Mariani, R. Mandrioli, and M. Ricco, "Modular dc/dc boost converter for efficient and ripple-free conversion in fuel cell-based powertrains," in *2024 IEEE 18th International Conference on Compatibility, Power Electronics and Power Engineering (CPE-POWERENG)*, pp. 1–6, IEEE, 2024.

[156] M. Hammami, A. Viatkin, M. Ricco, and G. Grandi, "A dc/dc fast charger for electric vehicles with minimum input/output ripple based on multiphase interleaved converters," in *2019 international conference on clean electrical power (ICCEP)*, pp. 187–192, IEEE, 2019.

[157] J. W. Kimball and P. T. Krein, "Discrete-time ripple correlation control for maximum power point tracking," *IEEE Transactions on Power Electronics*, vol. 23, no. 5, pp. 2353–2362, 2008.

[158] A. Costabeber, M. Carraro, and M. Zigliotto, "Convergence analysis and tuning of a sliding-mode ripple-correlation mppt," *IEEE Transactions on Energy Conversion*, vol. 30, no. 2, pp. 696–706, 2014.

[159] M. Hammami, M. Ricco, A. Ruderman, and G. Grandi, "Three-phase three-level flying capacitor pv generation system with an embedded ripple correlation control mppt algorithm," *Electronics*, vol. 8, no. 2, p. 118, 2019.

[160] C. W. T. McLyman, *Transformer and inductor design handbook*. CRC press, 2004.

[161] G. Gupta, B. Wu, S. Mylius, and G. J. Offer, "A systematic study on the use of short circuiting for the improvement of proton exchange membrane fuel cell performance," *International Journal of Hydrogen Energy*, vol. 42, no. 7, pp. 4320–4327, 2017.

[162] F. Grumm, M. Schumann, C. Cosse, M. Plenz, A. Lücken, and D. Schulz, "Short circuit characteristics of pem fuel cells for grid integration applications," *Electronics*, vol. 9, no. 4, 2020.

[163] M. Rimondi, R. Mandrioli, V. Cirimele, L. K. Pittala, M. Ricco, and G. Grandi, "Design of an integrated, six-phase, interleaved, synchronous dc/dc boost converter on a fuel-cell-powered sport catamaran," *Designs*, vol. 6, no. 6, 2022.

[164] A. Mariscotti, "Critical review of emc standards for the measurement of radiated electromagnetic emissions from transit line and rolling stock," *Energies*, vol. 14, no. 3, p. 759, 2021.

[165] P. Pizarro, E. Espina, M. Diaz, T. Ravet, A. Rojas, and D. Carrasco, "A new modular multilevel converter topology for green hydrogen production," in *2023 IEEE CHILEAN Conference on Electrical, Electronics Engineering, Information and Communication Technologies (CHILECON)*, pp. 1–6, IEEE, 2023.

[166] E. Rausell, G. Navarro, M. Lafoz, S. Arnaltes, J. L. Rodríguez, M. Blanco, and J. Nájera, "Analysis of using mmc topologies for the direct integration of renewable generation with modular electrolyzers," in *2023 25th European Conference on Power Electronics and Applications (EPE'23 ECCE Europe)*, pp. 1–8, IEEE, 2023.